UNIVERSITY OF CRETE

DEPARTMENT OF MATERIALS SCIENCE AND TECHNOLOGY

LIGHT SCATTERING TECHNIQUES FOR PROBING NEAR-WALL DYNAMICS AND FLOW OF COMPLEX FLUIDS

A THESIS

submitted by

Antonio Giuliani

for the degree of

Doctor of Philosophy

February 2019

Acknowledgements

My time in Crete has been full of delicious food, great weather, fun and loving people and let us not forget, science.

I want to thank the people that made it possible. First and foremost, thank you Benoit for choosing me for the project, for being my supervisor and for all the time you spent working with me. Although many times painful I know I will miss our discussions. Antje, thank you so very much from the bottom of my heart for being there with your wisdom. Antonakis, my future self, I had so much fun on our shared projects. Brutta pecora, for all the hate and love we share, ARGH! Ameur, for giving your perspectives and being honest with me. Damn, rheology! Salvatore for trying to kill me with Nitrogen, and Daniele for trying to maintain the tradition, AAAAHHHH!! Maria S. for her enthusiasm! Leo and Lucille for their infinite love. Papaya and Thanasito, better when they are together. Dimitris and George, thank you for your hard work and for allowing us to follow so many interesting talks. The King deserves a whole chapter to himself... Kate, the Continizer binds us. Claudia for what I cannot share here. Lida!!! The many other lab members that have come through and try their best including Kristina, Manos, Jose, Fytas, Mohandas, Yan, Nikos, Dimitra, Consiglia, Big Thanasis, Manolis G., Petros, Yuya, Antigoni, Maria, Ravi, Giulhem, Ricardo, Allan, Yan. Ruel, thank you for staying in touch from afar. I should thank the support teams at ITE (the workshop guys, Manolis and the administration offices) who were as friendly and helpful as they could. The collaboration with Lefteris and Fabien was priceless. It is always good to visit our friends at Vamvakaki's chemistry lab and the Biosensors group. Our lab is truly lovely and I am proud to have been part of the team. I wish the best to all of you.

My work was mostly financed by the SOMATAI ITN within which I am thankful to all of the PI's that hosted us around Europe and the many interesting lecturers. A particular thank you goes to Peter and Ulrike for the organization. I enjoyed the nights out and trips with my fellows from the network and made good memories. Especially with Nina who stayed with us for a while.

I also thank my dear Potata who became the reason why I actually finish my PhD. I thank my friends from outside the lab with whom I had so many laughs, dances, love, much food and drinks and adventures! They were always next to me and suffered indirectly through all my struggles. Finally thanks to my family for their love and supporting me on my academic quest.

Contents

Chapter 1

Introduction

1.1 Soft materials and soft matter science

Depicted in Fig. 1.1 are "soft" systems (as opposed to "hard" systems like metals) with molecular constituting components bound together, in general, by weak forces comparable to the thermal energy. This enables us to obtain strong responses from weak perturbations, either external or internal. Accompanying their weak interactions we find hierarchical structures that often lead to function.

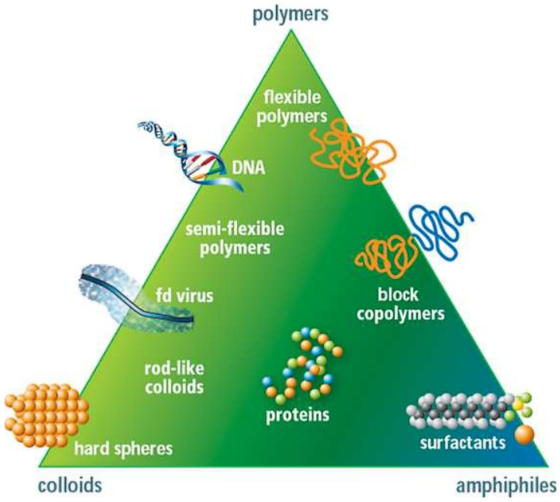

Figure 1.1: This "soft matter triangle" shows the continuum of molecules and systems part of the softmatter category. Taken from [1].

Departing from what nature provides, an ever-expanding list of man-crafted systems also make up part of the softmatter category. These share the characteristics mentioned above with natural systems and to some extent, they mimic natural behaviors and characteristics; such is the case for biomedical applications such as tissue engineering [2]. Part of the innovation within softmatter comes from novel artificial architectures. Think of polymer sciences and the exotic ring, brush, and star polymers [3, 4].

The term softmatter is clearly quite broad, capturing so much of what we experience in our daily lives. Food, pharmaceutical and chemical industries are all based on soft matter. Most food products are softmatter systems (yogurt, mayonnaise, cheese, chocolate...) and contain many components to give them their desired flavor, texture, aspect and shelf life [5]. Pharmaceutical products contain advanced systems for drug delivery, which can withstand harsh conditions (the human stomach) to then release active ingredients at specific targeted sites [6, 7]. Chemical industries provide us with so many of the commodities that we are accustomed to including packaging, gadgets, tires and clothing, which are in great part made out of plastics and their composites [8].

In terms of length scale, softmatter usually refers to macromolecular aggregates from 1 nm to $\sim \mu m$. Some systems extend further than that; gel structures, like the extracellular matrix, extend infinitely relative to the previous dimensions, and an unraveled Hagfish skein can be long 30 cm [9].

Characteristic time scales found within softmatter span a greater breadth. Atomic reconfiguration take place at 10^{-9} s, diffusion of particles happens around 10^{-6} s [10], polymer relaxation processes occur at 10^{-3} s [11], proteins fold at 1 s [12] and colloidal rearrangements can be slower than 10^{5} s [13]. Note, the processes just mentioned have themselves broad distributions.

Systems with quite different mechanical properties exist, in terms of their elastic moduli: colloidal dispersions can have 1 Pa, emulsions and foams 10^{2} Pa, elastomers 10^{6} Pa and glassy polymers 10^{9} Pa. They, moreover may exhibit strong non linearities under deformation (for example: shear thickening, shear thinning, and thixotropy).

The challenges with softmatter involve their design, tuning, fabrication and industrialization. That means more than hard work on the development of new products that drives and is driven by the basic research done within softmatter.

The field is necessarily at the intersection of different professions, encompassing biology, physics, mathematics, physical chemistry, optics, food sciences, rheology, surface sciences and others.

1.2 Soft matter and interfaces

Interfaces are ubiquitous in soft matter, this is no surprise given its common hierarchical structures. Take colloids and nanoparticles for example, the ratio of surface to volume goes as 1/radius, for a given mass concentration therefore, the amount of surface increases as dimensions become smaller. Biphasic materials like polymeric mixtures, emulsions and foams are clearly another case where interfaces become dominant.

Interfaces, either between solid, liquid and gas, or between different components are regions of high Gibbs energy. They present discontinuities in long range order and chemical nature, which results in charge unbalance, entropic migrations, surface elastic properties and confinement effects. Interactions with a solid wall will lead to reduction of the diffusion coefficient of colloids next to it by hydrodynamic means; the same colloid will tend to pin itself to a liquid air interface to minimize the surface energy. Polymers attached to a solid particle will acquire different conformations depending on their surface density and the specific interaction with the solvent and solid particle. Given their ubiquity and complexity, it is clear that, interfaces play an active role and must be considered.

The work of this thesis was done on interfacial softmatter. It was carried out within the framework of the Marie Curie initial training network (ITN) SOMATAI (soft matter at aqueous interfaces). This ITN's purpose was to train young scientists in softmatter and in particular interfacial softmatter additionally providing soft skills and international experience.

By comparison to the bulk of a material, interfaces pose the technical challenge of being, by definition, infinitesimally small in mass and thickness. Sensitive methods are therefore required to measure their properties. These include among others, a list of probe, microscopy and reflection based techniques with high sensitivity requirements.

1.3 The thesis

This work has a strong component of technical development based on the total internal reflection (TIR) of light. TIR occurs for optical rays when the reflection is from the medium of higher refractive index above a certain critical angle. An evanescent wave (EW) is produced in the lower refractive index medium; this wave is a non propagating electromagnetic wave which decays exponentially into the medium, over a characteristic length called the penetration depth $\sim \lambda$. This field extends a few 100 nm's into the medium and provides very local sensitivity suited for the study of interfacial properties. The EW can be used as a source for dynamic light scattering (DLS), in pretty much the same way as traditionally done in the bulk, to measure diffusion coefficients. Information on the structure of interfaces, thickness of layers, and their refractive index can be recovered from the ratio of the out of plane and in plane polarizations measured by ellipsometry. Internal reflection is a variation of the technique suited to studying adsorbed material without concern of the bulk material. In complementarity to the experimental work, we used modeling and computer simulations to support and rationalize our observations.

EW-DLS velocimetry In chapter 3 we present the principle and implementation of a novel in situ dynamic light scattering velocimetry on a commercial rheometer. The technique is based on total internal reflection at the bottom plate of a rheometer. The evanescent wave that penetrates sub-micron level into the sample enables the monitoring of the near wall dynamics under rheometric flow. Slip during shear is detected by measuring the near wall (NW) velocity profile. We discuss how to extract the near wall velocities from the measured autocorrelation functions, using Fourier transform analysis. The method was tested on a Newtonian fluid, colloidal dispersions and polymer solutions. Stick boundary conditions were observed in the Newtonian fluid; the presence of strong slip was easily identified in visco-elastic colloidal suspensions; and polymer solutions were found to present weak slip. This high resolution near wall velocimetry rheo-optical technique should prove valuable for a broad range of flowing materials.

EW-DLS on turbid media In chapter 4 we investigate the effect of multiple scattering on EW-DLS measurements. Traditional DLS and EW-DLS measurements need to be performed on optically dilute conditions (either from low concentration or low contrast) where there exists a well defined physical relation between time, length and scattering angle. What constitutes the signal from multiple scattering using an EW geometry and whether any useful quantities can be measured have not been addressed until now. The localized scattering and the point of entrance detection of the EW geometry yield a sizable single scattering component that made it possible to recover quasi single scattering dynamics in strongly turbid media. Moreover studies under shear as in chapter 3 reveal strong temporal decoupling of the near wall single scattering dynamics and useful DWS like bulk shear rate information so that both the previously established near wall velocimetry and DWS like velocimetry can be performed in the same experiment. This makes it theoretically possible to estimate the full flow profile while preserving excellent surface sensitivity. The strong contrast provides abundance in signal making the experiments faster and simpler than the optically dilute counterparts. Our results are supported by Monte Carlo ray tracing simulations that indicate the effective distinction of the single scattering signal and ability to recover the near wall dynamics for evanescent wave illumination.

Ellipsometry of turbid media In chapter 5 we report on the application and validity of effective medium models for turbid media in internal reflection variable angle spectroscopic ellipsometry (VASE). The proper description of the clear-turbid interface is not fully established. The reflectivity between a transparent substrate and a turbid medium is of interest as it could be used to characterize the turbid medium and provide a way to estimate size, refractive index and composition. Different models mostly semi-empirical have been produced, but don't fully agree. Effective medium approaches have been used to compute the reflectivity coefficient of these interfaces, mostly in the context of angular dependence of reflectivity measurements and the occurrence of total internal reflection close to the critical angle [14, 15, 16, 17, 18, 19]. Both attenuated total reflection (ATR) spectroscopy type of approach and ellipsometric approaches have not been much explored. Here we report on internal VASE to characterize turbid medium using an effective medium approximation. In particular we show the value of the wavelength dependence for determining the scattering losses. The measurements are relatively straightforward, but the analysis/interpretation of the data are somewhat model dependent. The merit of effective medium approximation based models is evaluated. In the case of PS latex dispersion we found that an EMA description of the refractive index, where the real part is described by a mixing law, and the imaginary part is accounted for by the optical losses through Mie scattering, provide good representation of the internal VASE data using a non-lossy layer at the interface.

Internal reflection study of polyelectrolyte brushes In chapter 6 we investigate the dynamics and pH induced swelling kinetics of high Mw polyelectrolyte brushes (PEB) after they have undergone strong degrafting. The results presented are preliminary. Polyelectrolyte brushes are charged polymeric chains attached from one free end to a surface. They are a versatile surface functionalization as they can be thermo-, photo- and pH responsive [20]. Measurements of internal dynamics of PEB's are not intensely pursued in literature, due to lack of experimental techniques. Our study was carried out using EW-DLS, that has so far mostly been applied to the case of neutral polymer brush [21, 22]. Understanding dynamics requires a good knowledge of the concentration profile. Many studies have reported the swelling behavior of such PE responsive brushes. Internal reflection VASE was used to determine wet thicknesses and measure its pH time response. The time dependence of the response is important with practical implications. Several studies have reported rather long equilibration time of the layer following the change of pH of the surrounding fluid [23]. The origin of the slow response is not fully resolved.

Bibliography

[1] G. Gompper, J. K. G. Dhont, and D. Richter, "A unified view of soft matter systems," *The European Physical Journal E*, vol. 26, pp. 1–2, may 2008.

[2] R. Langer and J. P. Vacanti, "Tissue engineering," *Science*, 1993.

[3] G. Polymeropoulos, G. Zapsas, K. Ntetsikas, P. Bilalis, Y. Gnanou, and N. Hadjichristidis, "50th Anniversary Perspective: Polymers with Complex Architectures," *Macromolecules*, vol. 50, pp. 1253–1290, feb 2017.

[4] S. T. Milner, "Polymer brushes," *Science*, vol. 251, pp. 905–914, feb 1991.

[5] R. G. Van Der Sman, "Soft matter approaches to food structuring," 2012.

[6] M. Malmsten, "Soft drug delivery systems," 2006.

[7] G. Paradossi, F. Cavalieri, and E. Chiessi, "Soft condensed matter in pharmaceutical design.," *Curr. Pharm. Des.*, 2006.

[8] D.-K. Yang and S.-T. Wu, *Fundamentals of Liquid Crystal Devices.* John Wiley & Sons, 2014.

[9] D. S. Fudge, N. Levy, S. Chiu, and J. M. Gosline, "Composition, morphology and mechanics of hagfish slime," *Journal of Experimental Biology*, vol. 208, pp. 4613–4625, dec 2005.

[10] C. Marlière, P. Faure, P. Coussot, D. Vlassopoulos, A. Larsen, and B. Loppinet, "Jamming of cellulose ether solutions in porous medium," *AIChE Journal*, 2015.

[11] S. Costanzo, Q. Huang, G. Ianniruberto, G. Marrucci, O. Hassager, and D. Vlassopoulos, "Shear and Extensional Rheology of Polystyrene Melts and Solutions with the Same Number of Entanglements," *Macromolecules*, 2016.

[12] N. J. Greenfield, “Analysis of the kinetics of folding of proteins and peptides using circular dichroism.,” *Nature protocols*, vol. 1, no. 6, pp. 2891–9, 2006.

[13] M. Laurati, G. Petekidis, N. Koumakis, F. Cardinaux, A. B. Schofield, J. M. Brader, M. Fuchs, and S. U. Egelhaaf, “Structure, dynamics, and rheology of colloid-polymer mixtures: From liquids to gels,” *The Journal of Chemical Physics*, vol. 130, p. 134907, apr 2009.

[14] J. A. Rety and K. E. Peiponen, “Reflectance study of milk in the UV-visible range,” *Applied Spectroscopy*, vol. 53, no. 9, pp. 1123–1127, 1999.

[15] K. E. Peiponen, A. Jaskelainen, J. Raty, O. Richard, U. Tapper, E. I. Kauppinen, and K. Lumme, “Reflectance study of pigment slurries,” *Applied Spectroscopy*, vol. 54, no. 6, pp. 878–884, 2000.

[16] I. Niskanen, J. Räty, and K.-E. Peiponen, “Complex refractive index of turbid liquids,” *Optics Letters*, vol. 32, p. 862, apr 2007.

[17] W. R. Calhoun, H. Maeta, A. Combs, L. M. Bali, and S. Bali, “Measurement of the refractive index of highly turbid media,” *Optics Letters*, vol. 35, p. 1224, apr 2010.

[18] H. Contreras-Tello and A. García-Valenzuela, “Refractive index measurement of turbid media by transmission of backscattered light near the critical angle,” *Applied Optics*, vol. 53, no. 21, p. 4768, 2014.

[19] J. Sun, J. Wang, Q. Ye, J. Mei, W. Zhou, C. Zhang, and J. Tian, “Analysis of reflectance curve of turbid media and determination of the non-surface complex refractive index,” *Optics Express*, vol. 23, p. 24602, sep 2015.

[20] W. L. Chen, R. Cordero, H. Tran, and C. K. Ober, “50th Anniversary Perspective: Polymer Brushes: Novel Surfaces for Future Materials,” *Macromolecules*, vol. 50, pp. 4089–4113, jun 2017.

[21] G. Fytas, S. H. Anastasiadis, R. Seghrouchni, D. Vlassopoulos, J. Li, B. J. Factor, W. Theobald, and C. Toprakcioglu, “Probing collective motions of terminally anchored polymers,” *Science*, vol. 274, pp. 2041–2044, dec 1996.

[22] V. N. Michailidou, B. Loppinet, D. C. Vo, O. Prucker, J. Rühe, and G. Fytas, “Dynamics of end-grafted polystyrene brushes in theta solvents,” *Journal of Polymer Science, Part B: Polymer Physics*, vol. 44, no. 24, pp. 3590–3597, 2006.

[23] J. D. Willott, T. J. Murdoch, B. A. Humphreys, S. Edmondson, G. B. Webber, and E. J. Wanless, “Critical salt effects in the swelling behavior of a weak polybasic brush,” *Langmuir*, vol. 30, pp. 1827–1836, feb 2014.

Chapter 2

Basic working principles

The information in this chapter is not comprehensive and was taken from different sources. The aim of this chapter is to give the reader basic background information on the theories and terminology used in this thesis.

For more details on scattering and dynamic light scattering refer to the books by Pecora [1] and Lindner [2]. An easy to read review on DWS was given by Maret [3]. For more information on multiple scattering refer to the chapter by Pine and Weitz [4] in Brown's Dynamic light scattering book. Alternatively, visit the review by Pine et al. from 1990 [5] or the paper by Rojas-Ochoa et al. [6]. For the section on ellipsometry, a fantastic resource on reflection theory is Lekner's book [7], while on ellipsometry you can visit the book by Fujiwara [8]. Fuller wrote a book that includes plenty of material including ellipsometry and light scattering applied to rheooptical studies [9]. Finally, the books by Barnes [10] and Larson [11] provide a broad overview on rheology and flow of complex fluids.

2.1 Basic light scattering theory

Take a dielectric medium of average dielectric constant ϵ_0 (and refractive index $n_0 = \sqrt{\epsilon_0}$). Now consider a monochromatic coherent planar wave of frequency ω_i propagating along $\boldsymbol{k_i}$ incident in $\boldsymbol{r}$ of the form:

$$E_i(r,t) = E_0 \exp\left[i(\boldsymbol{k_i} \cdot \boldsymbol{r} - \omega_i t)\right] \tag{2.1}$$

A particle located at $\boldsymbol{r}$ behaving as a dipole μ will oscillate according to its polarizability α, $\mu = \alpha E$ and irradiate light. The field at $\boldsymbol{R}$ is

$$E_s(R,t) = \frac{k_f^2 E_0}{4\pi\epsilon_0 R}\alpha(\boldsymbol{r}) \exp i(k_f R - \omega_s t) \exp i(\boldsymbol{k_i} \cdot \boldsymbol{r}) \tag{2.2}$$

Where the subscript f indicates that the quantity refers to the final state. Using Clausius-Mossotti relation ($(n^2-1)/(n^2+2) = 4\pi N\alpha/3$, for number density N) to express the polarizability and a Taylor expansion over dn/dc gives $\alpha(\boldsymbol{r}) = (m(\boldsymbol{r})/2\pi N_A)(dn/dc)$ with $m(\boldsymbol{r})$ the molar mass distribution. It follows that the scattered intensity is proportional to the square of the mass.

With an appropriate coordinate change, we can integrate over a particle's volume.

$$\begin{gathered} E_s(\boldsymbol{r'},t) = \\ \frac{k_f^2 E_0}{8\pi^2 N_A \epsilon_0 R}\frac{dn}{dc} \exp i(k_f R + k_i \cdot r_0 - \omega_i t) \int_V m(\boldsymbol{r'}) \exp -i\boldsymbol{q} \cdot \boldsymbol{r'} d^3 r' \end{gathered} \tag{2.3}$$

The product of the scattering wave vector $\boldsymbol{q} = \boldsymbol{k_f} - \boldsymbol{k_i}$ with the element dr is the phase shift of two points relative to the detector. The previous integral is the Fourier transform of $m(r)$, in other words, it represents density variations over length scales $\boldsymbol{q}^{-1}$ instead of the innumerable coordinates $\boldsymbol{r}$. Assuming an elastic process ($|\boldsymbol{k_f}| = |\boldsymbol{k_i}|$), under the scattering angle θ, we have:

$$q^2 = \left|\boldsymbol{k_f} - \boldsymbol{k_i}\right|^2 = k_f^2 + k_i^2 - 2\boldsymbol{k_f} \cdot \boldsymbol{k_i} = 2k_i^2 - 2k_i^2 \cos(\theta) = 4k_i^2 \sin^2(\frac{\theta}{2}) \tag{2.4}$$

For the case of solid particles of size $\sim \lambda$, internal reflections need to be taken into account with Mie scattering theory [12]. Note that Mie theory is meant only for spherical particles but other methods exist [13]. Dimensions comparable to λ lead to resonances with peaks and minima on the angular scattered intensity.

In the presence of other identical particles, another change of coordinates can be carried out. Setting $\boldsymbol{r'} = \boldsymbol{r'_i} + \boldsymbol{R_i}$, where $\boldsymbol{R_i}$ is the reference point of particle i. We can sum over the reference points $\boldsymbol{R_i}$ of each particle getting the extra term.

$$\sum_{i}^{N} \exp i(\boldsymbol{q} \cdot \boldsymbol{R_i}) \tag{2.5}$$

Experimentally, the intensity $I = |\boldsymbol{E}|^2 = I$ is measured and not the field $\boldsymbol{E}$. Assuming ergodicity (equivalence between time and ensemble average), one can average over all orientations (and conformations) of the particles. The scattered intensity can then be expressed as the product of the Form ($F(q)$) and Structure ($S(q)$) factors. This is the basis of static light scattering (SLS).

$$I(q) = I_0 S(q) F(q) \tag{2.6}$$

In optically dilute experimental conditions (i.e. single scattering), the scattering vector allows us to probe different length scales. In practice, by moving yourself on the angular sphere, you are moving on the reciprocal space of the density fluctuations in the sample.

In the case of a dilute dispersion, the particle-particle interactions are small, so there is no correlation between them and the total intensity results in the sum of the many. For the case of correlated positions, given a virial expansion for their interactions, the structure factor is written as follows:

$$S(0) = \frac{1}{1 + 2\bar{B}_2 w + O(w^2)} \tag{2.7}$$

where w is the sample mass concentration and $\bar{B}_2$ is the mass based second virial coefficient. In dilute solutions ($S \sim 1$) and at small angles ($qR_g \ll 1$), $F(q) = 1 - q^2 R_g^2/3$. R_g being the radius of gyration of the particle, an average of the mass distribution within a particle.

$$\left\langle R_g^2 \right\rangle = \frac{\int_V m(\boldsymbol{r}) r^2 d\boldsymbol{r}}{\int_V m(\boldsymbol{r}) d\boldsymbol{r}} \tag{2.8}$$

2.2 Correlation Spectroscopy

The time auto-correlation function of the electric field in a light scattering experiment, defined as:

$$g(q,\tau) = \frac{\langle E(q,t)E^*(q,t+\tau)\rangle}{\langle E(q,t)E^*(q,t)\rangle} \tag{2.9}$$

Gives access to the microscopic dynamics within the system. To see this, we take a look at the autocorrelation of the particle positions term Eq. 2.5,

$$\frac{\left\langle \sum_j^N \sum_i^N \exp i(\boldsymbol{q} \cdot (\boldsymbol{R}_{\boldsymbol{i}}(t) - \boldsymbol{R}_{\boldsymbol{j}}(t+\tau))) \right\rangle}{\left\langle \sum_j^N \sum_i^N \exp i(\boldsymbol{q} \cdot (\boldsymbol{R}_{\boldsymbol{i}}(t) - \boldsymbol{R}_{\boldsymbol{j}}(t))) \right\rangle} \tag{2.10}$$

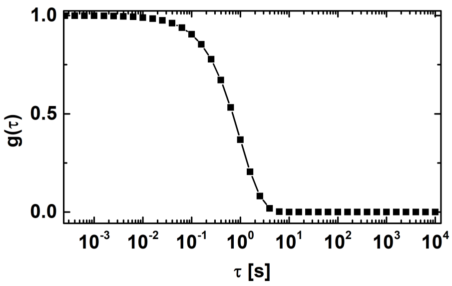

Figure 2.1: Exponential decay with decay rate of 1 s in lin-log scale with times equally spaced in log scale (equivalent to the so called multi-tau).

for cases with some random component to it, say diffusion, the correlation will be maximum at $\tau \to 0$ and then will decay to 0 as the random motion will eventually lead to complete loss of correlation. Typically, decorrelation decays have exponential shape and are calculated at times τ with a quasi linear spacing called the multi-tau [14] (see Fig. 2.1 for an example). The characteristic time of the decay is given by the time it takes the scattering center to move over λ (this is fundamentally an interferometric experiment). For Brownian motion of uncorrelated particles, the cross terms in Eq.

2.10 vanish.

$$\frac{1}{N}\left\langle \sum_{j}^{N} \exp i(\boldsymbol{q}\cdot(\boldsymbol{R_j}(t)-\boldsymbol{R_j}(t+\tau)))\right\rangle = \langle \exp i(\boldsymbol{q}\cdot \Delta\boldsymbol{R}(\tau))\rangle \tag{2.11}$$

By Taylor expanding the right hand side on Eq. 2.11 and realizing the second term is 0 for Brownian motion, we can write the following.

$$\langle \exp i(\boldsymbol{q}\cdot \Delta\boldsymbol{R}(\tau))\rangle = \exp\left(-q^2 < \Delta R(\tau)^2 >\right) = \exp\left(-Dq^2\tau\right) \tag{2.12}$$

The right side of Eq. 2.12 follows from the definition of the diffusion coefficient projected on one dimension $D = (\Delta R(dt))^2/2dt$. By making use of Stokes-Einstein relation we can further obtain the hydrodynamic size of the particles. Assuming spherical particle:

$$D = \frac{kT}{6\pi\eta R_H} \tag{2.13}$$

Where kT is the thermal energy, η is the surrounding medium viscosity and R_H is the hydrodynamic radius of the particle. In case of correlated particle motion, the diffusion coefficient becomes a function of the hydrodynamic interaction $(H(q))$ and the structure factor.

$$D(q) = D_0\frac{H(q)}{S(q)} \tag{2.14}$$

Given the measurable quantity on an experiment is the intensity, we hope for a way to relate its correlation function to the field correlation function. The generalized Siegert relation does this.

$$g_{measured}(\tau) = (1-B)^2\left|g(\tau)\right|^2 + 2B(1-B)\Re(g(\tau)) \tag{2.15}$$

The above equation assumes there are two sources of light reaching the detector, first, the signal of interest and second, a reference static signal which does not vary significantly in time. B is equal to $\sqrt{1-A}$, where A is the amplitude of the measured correlation function ($g_{measured}(0) - g_{measured}(\infty)$). A is also equal to the ratio $I_{dynamics}/I_{ref}$ in case of single speckle detection.

The static signal can come from a portion of the beam split before the sample and mixed again at the detector, or in the case of evanescent wave experiments with glass as the high refractive index material, from the light scattered by the defects on the solid piece of glass at the spot of reflection.

When $B = 0$ ($A = 1$, or full amplitude) the measured correlation function is equal to the modulus square of the field correlation function; this is referred to as the homodyne mode. As a consequence, the phase of the electric field is lost. To correctly analyze a homodyne correlogram, it should be converted to field correlogram. A bimodal system serves as a good example. If two decays appear on the field correlogram, the square operation on Eq. 2.15 will make a third "apparent" mode appear.

For $B > 0$, the measured correlogram includes the real part of the field correlation function; and for $B \sim 1$ the two are approximately the same; these are referred to as mode mixing or heterodyne mode. The measured correlation function is then a direct measurement of the field correlation function, and the phase there included is conserved.

The presence of the phase becomes useful when one desires to measure velocimetry. For directional motion $\Delta R(t) = vt$, so from Eqs. 2.11 and 2.15, the measured correlogram will have the form $\cos(\boldsymbol{q} \cdot \boldsymbol{v}t)$, only measurable on heterodyne mode. A peculiarity of Eq. 2.15 is that the measured correlogram can acquire negative values only during heterodyne mode.

2.3 Multiple scattering

Turbidity is the result of a high concentration of particles/scatterers on the path of the light to the observer which prevent the light from traveling in a straight line. Such is the effect observed with fog (droplets of water), smoke (solid particles) and milk (fat globules).

The higher the concentration of scatterers, the more likely light will be deviated from its trajectory. The mean free path, l, is the average distance between two successive scattering events. One should compare with this length scale to determine the amount of scattering though a medium of thickness L. When $L \ll l$, we are on the optically dilute regime, or single scattering regime, the medium looks transparent. This is where the traditional DLS experiments are carried out. At $L \sim l$, just a fraction of the initial beam makes it through the slab unscattered and T becomes appreciably less than 1. For the two cases mentioned above, the transmission of light through a non absorbing slab of thickness L containing scattering centers is given by Beer-Lambert law [15].

$$T = \frac{I}{I_0} = \exp\left(-\frac{L}{l}\right) \tag{2.16}$$

If no positional correlations between the particles exist (in low concentrations), l is simply the product of the scattering cross section and number concentration of the scattering particles ($l = 1/\rho C_{sca} = \lambda/4\pi n''$).

At every scattering event the direction of a photon is changed, and so is its polarization. For $L \gg l$, the direction of travel of every photon is randomized and the polarization of the original beam is lost. As such, the photon trajectory can be described by a random walk with steps of length l^*. This is the diffuse wave limit, or diffusing wave spectroscopy (DWS) limit.

$$l^* = \frac{l}{1 - \langle \cos\theta \rangle} = l\frac{2k_0^2}{\langle q^2 \rangle} \tag{2.17}$$

where $\langle \cos\theta \rangle$ is averaged over the scattering angle according to the appropriate scattering function. Positional correlation need to be taken into account when necessary. $\langle \cos\theta \rangle$ is usually referred to as g, the anisotropy factor. For Rayleigh scattering $g \sim 0$, i.e. for small particles $l^* = l$, the random walk is described in steps of l. For correlated scatterers one needs to account for $S(\boldsymbol{q}) \neq 1$ when calculating $\langle q^2 \rangle$.

The transmitted intensity pass such slab is given by [16]

$$T = \frac{\frac{5l^*}{3L}}{1 + \frac{5l^*}{3L}} \tag{2.18}$$

Transmission measurements can therefore be used to estimate the l^* of an unknown sample through a reference sample of known l^*.

Stronger scattering regimes are not considered here [17, 6].

To calculate the field correlation function through multiple scattering, we neglect interference within the turbid medium. We calculate the correlation function for all the different random walk paths and then sum them all up at the detector. Going to the continuous limit we obtain the integral:

$$g(\tau) = \int_0^\infty P(S') g_{S'}(\tau) dS' \tag{2.19}$$

Here $P(S)$ is the probability density function of path lengths S' and $g_{S'}(\tau)$ is the correlation function for path S'. Consider the path S where the photon has been scattered n times. Along S the photon has accumulated a total phase shift $\Delta\Phi_S(\tau) = \sum_{i=1}^{n} \boldsymbol{q} \cdot \Delta\boldsymbol{r}_{\boldsymbol{i}}(\tau)$. The field correlation function for S is then:

$$g_S(\tau) = \exp -i\Delta\Phi_S(\tau) = \langle \exp -i \left(\boldsymbol{q} \cdot \Delta\boldsymbol{r}(\tau) \right) \rangle_q^n \tag{2.20}$$

Where on the right side we have taken the product over n steps with each of them having the same average phase shift. After Taylor expanding and taking into account the Brownian motion of the scatterers, that the scattering vector is independent of the mean square displacement and given $\langle \Delta\boldsymbol{r}(\tau)^2 \rangle = 6D\tau$. Using Eq. 2.17 an expression for the nth order scattering correlation function in terms of the number of scattering events or the total length of the path S is obtained.

$$g_S(\tau) = \exp\left(-n\left\langle \boldsymbol{q}^2\right\rangle\left\langle \Delta\boldsymbol{r}(\tau)^2\right\rangle/6\right) = \exp\left(-2k_0^2 D\frac{S}{l^*}\tau\right) \tag{2.21}$$

For the backscattering from a slab of infinite thickness, the correlation function takes the form:

$$g(t) = \exp\left(-\gamma\sqrt{k_0^2\left\langle \Delta r^2(t)\right\rangle}\right) \tag{2.22}$$

where $\gamma = z_0/l^* + 2/3$ z_0 is the distance of the first scattering from the surface, or alternatively the source of multiple scattering. z_0 is important when solving the diffusion equations in backscattering. For the forward scattering experiment, the early slope has the form:

$$\frac{(L/l^*)^2 + +4(L/l^*) + 8/3}{\tau_0(1 + 4l^*/3L)} \tag{2.23}$$

The problem to solve for specific scattering geometries is a tough one, so ray tracing simulations are commonly used instead. The characteristic time scale of the correlogram corresponds to the time the phase shift to become roughly unity, $nq^2\delta r^2 \sim 1$. For the diffusive limit across a distance L, $n = (L/l^*)^2$ so $\delta r = \lambda l^*/2\pi L \ll \lambda$. Therefore, in a DWS experiment ($l^*/L \ll 1$), small motions are probed, well below λ.

2.4 Evanescent wave - total internal reflection

Consider light hitting the interface between two media of distinct refractive index along the xz plane of incidence. It can be seen from Maxwell's equations and the continuity of the electromagnetic field that $k_{1\parallel} = k_{2\parallel}$ (equivalent to Snell's law $n_1\sin(\theta_i) = n_2\sin(\theta_t)$). Following, the component of $\boldsymbol{k_2}$ normal to the interface (along the z axis) is:

$$k_{2\perp} = k_2\sqrt{1-\sin^2(\theta_t)} = k_2\sqrt{1-\left(\frac{n_1}{n_2}\right)^2\sin^2(\theta_i)} \tag{2.24}$$

Under the condition of $n_1 < n_2$, $k_{2\perp}$ remains real. Notice that in optics it is usual to write the subscript (index) of the media increasing along the path. The case of reflection for $n_1 < n_2$ is referred to as external reflection, while $n_1 > n_2$ is referred to as internal reflection. Under internal reflection, $k_{2\perp}$ can take imaginary values at angles above the critical angle θ_c.

$$\theta_c = \arcsin\left(\frac{n_2}{n_1}\right) \tag{2.25}$$

The electric field on the lower refractive index medium then decays exponentially, $E(z) = E_0 \exp\left(-k_{2\perp} z\right)$. Finally, the intensity is written as:

$$I(z) = |E(z)|^2 = I_0 \exp\left(-2k_{2\perp} z\right) = I_0 \exp\left(-z/dp\right) \tag{2.26}$$

where dp is the intensity penetration depth defined below.

$$1/dp = 2k_0 n_2 \sqrt{\left(\frac{n_1}{n_2}\right)^2 \sin^2(\theta_i) - 1} \tag{2.27}$$

At this point, we find ourselves in the condition total internal reflection (TIR). The field does not propagate into the second medium as it decays exponentially, with dp being the natural length of the decay. 100% of the light is reflected. The evanescent field nonetheless probes the near wall environment within $dp \sim \lambda$. This source of light can be used to carry out surface sensitive measurements in fluorescence (TIRF) or scattering (EW-DLS).

$T = \left(\frac{n_t \cos\theta_t}{n_i \cos\theta_i}\right) t^2$

2.5 Ellipsometry

2.5.1 Reflectivity

Consider a wave incident on an interface between two isotropic dielectrics, where the incident, reflected and transmitted wave all lie on a 'reflection plane'. A good choice of coordinates for the polarization of the field is the decomposition along the interface, referred to as S polarization, and normal to the interface (or along the plane of reflection) referred to as P polarization. See Fig. 2.4 for clarification. The ratio of the amplitude of reflected and transmitted wave with the incident wave is the reflection coefficient $E_r/E_i = r$ and transmission coefficient $E_t/E_i = t$. The square of those quantities are called reflectance or reflectivity and transmittance (usually represented with capitals R and T) (the transmittance is actually $T = \left(\frac{n_t \cos\theta_t}{n_i \cos\theta_i}\right) t^2$).

$$r_s = \frac{E_{r,s}}{E_{i,s}} = \frac{k_{1\perp} - k_{2\perp}}{k_{1\perp} + k_{2\perp}} = \frac{n_1 \cos\theta_i - n_2 \cos\theta_t}{n_1 \cos\theta_i + n_2 \cos\theta_t} \tag{2.28}$$

$$r_p = \frac{E_{r,s}}{E_{i,s}} = \frac{\frac{k_{1\perp}}{n_1^2} - \frac{k_{2\perp}}{n_2^2}}{\frac{k_{1\perp}}{n_1^2} + \frac{k_{2\perp}}{n_2^2}} = \frac{n_2 \cos\theta_i - n_1 \cos\theta_t}{n_2 \cos\theta_i + n_1 \cos\theta_t} \tag{2.29}$$

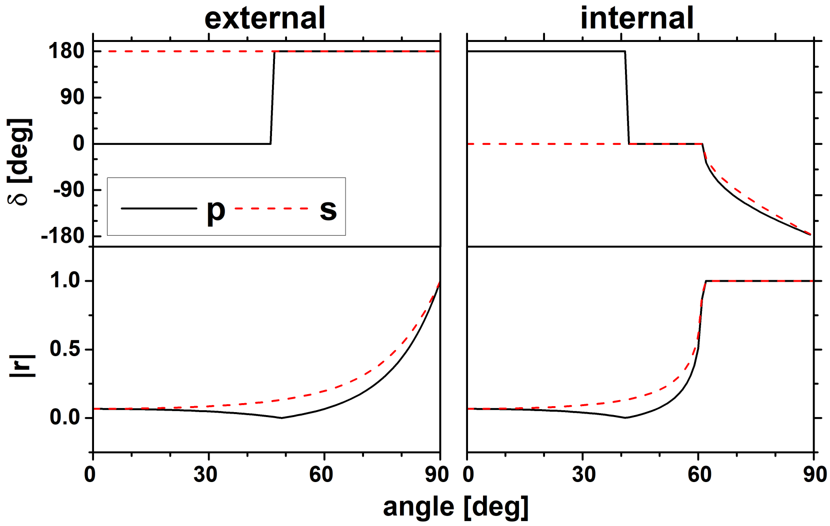

Figure 2.2: Phase and amplitude of the reflection coefficients for a Fresnel interface in both S and P polarizations. Refractive indexes: 1.52 (BK7 glass) and 1.33 (water). $\theta_B = 48.8°$ for external and $\theta_B = 41.2°$ and $\theta_c = 61.0°$ for internal reflection .

Figure 2.2 shows the values of both the amplitude and the phase and 2.3 shows the reflectivity curves for external reflection (2.3a), $n_1/n_2 = 1.33/1.52$, and internal reflection (2.3b), $n_1/n_2 = 1.52/1.33$. Two angles are of particular significance on this figure. First, an angle at which R_p falls to 0, called the Brewster angle θ_B; this is verified on both internal and external reflections. The Brewster angle is exploited for its sensitivity to changes of the interface (for example, absorption of molecules).

$$\theta_B = \arctan\left(\frac{n_2}{n_1}\right) \tag{2.30}$$

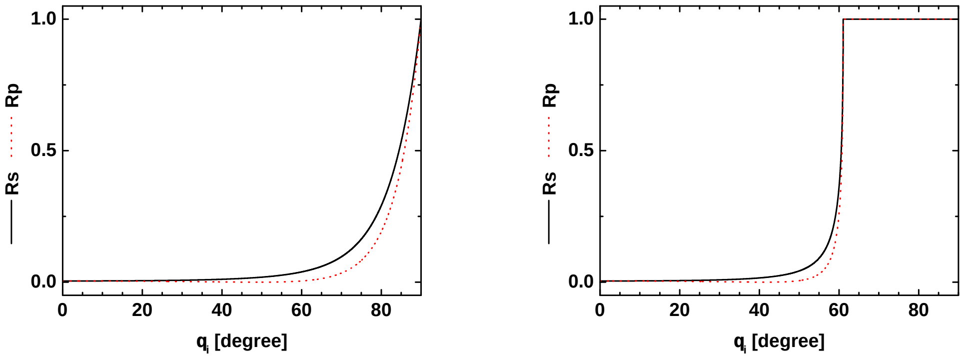

(a) external reflection

(b) internal reflection

Figure 2.3: S and P reflectivity curves, left external, right internal reflection. For refractive indexes 1.52 (BK7 glass) and 1.33 (water). $\theta_B = 48.8°$ for external and $\theta_B = 41.2°$ and $\theta_c = 61.0°$ for internal reflection.

The second angle is the total internal reflection critical angle θ_c given by Eq. 2.25, which, as the name implies, happens only in internal reflection. Above this angle 100% of the intensity of S and P polarization is reflected. For a thin film of thickness d, with interfaces 1|2 and 2|3, multiple reflections arise within the film. For both S and P polarizations, interference among the reflections leads to the following expression for r.

$$r = \frac{r_{1|2} + r_{2|3}\exp\left(-i2n_2\cos\theta_2\right)}{1 + r_{1|2}r_{2|3}\exp\left(-i2n_2\cos\theta_2\right)} \tag{2.31}$$

Extension to multilayer systems is done by matrix methods where each interface and layer is represented by its own matrix. The final reflection coefficients are calculated from the product of the subsequent interfaces and layers matrices.

2.5.2 Ellipsometry

The name ellipsometry comes from the fact that linearly polarized light often becomes elliptical upon light reflection like depicted in Fig. 2.4. The ellipsometric ratio is given by:

$$\frac{r_p}{r_s} = \frac{|r_p|}{|r_s|}e^{i(\delta_{r,p}-\delta_{r,s})} = \tan\left(\Psi\right)e^{i\Delta} \tag{2.32}$$

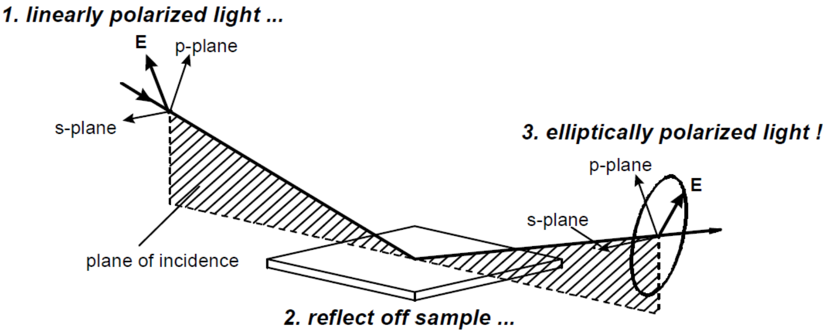

Figure 2.4: Diagram of reflection of linearly polarized light. Taken from the CompleteEase manual by J.A. Woollam Co..

measures this "transformation". The angles Ψ and Δ represent respectively, the amplitude ratio and the phase shift difference between P and S polarizations.

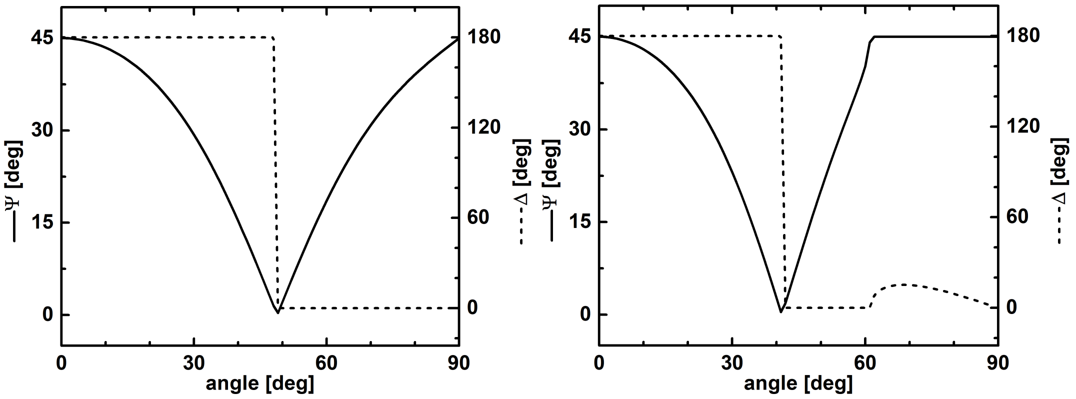

(a) External **(b)** Internal

Figure 2.5: Ellipsometric angles for a simple Fresnel interface. For refractive indexes 1.52 (BK7 glass) and 1.33 (water).

Variable angle spectroscopic ellipsometry (VASE) measures these quantities at different angles and wavelength. The measurements have generally high precision as they derive from the relative change on the two polarizations. The resolution is typically of 0.01°. Ellipsometry is useful and powerful, of widespread use when measuring surface properties such as film thickness (thin-film structures as multilayers), refractive indexes or dielectric functions (and therefore for example, carrier concentration on semiconductors), surface adsorption, etching or thermal oxidation. Particular sensitivity is found at the Brewster and the critical angle. Sophisticated hardware and software make this possible. Be warned though, the desired quantities are not, in general, directly related to the ellipsometric angles, instead one requires models, which are not generally unique solutions.

2.6 Rheology

Rheology is the study of the flow and deformation of matter. A rheometer is a device that either applies a stress (force/area) and measures a deformation or conversely applies a deformation and measures a stress. Many experimental approaches are used for such purposes including elongation, rotation and tube flow to measure the different components of the stress tensor. Rheological tests serve to understand the internal dynamics and structure of complex fluids and can be considered a mechanical spectroscopy. More simply they are necessary mechanical characterization tools.

On rotational plate-plate shear flow, a sample is sandwiched between two parallel horizontal flat plates and the top plate rotates causing a shear deformation on the sample. The velocity and displacement of the fluid increase as a function of the z axis along the gap for a rotating top plate. The deformation is given by the shear strain $\gamma = \delta/h$ and the rate of deformation by the shear rate $\dot{\gamma} = d\gamma/dt = dv/dz$. Notice that the top plate velocity is a function of the radius ($v(r) = \Omega r \implies \dot{\gamma} = \Omega r/H$), as such, for the plate-plate geometry the shear rate increases along the radius. Constant shear rate along the radius can be accomplished by use of the cone-plate geometry where one plate is conical and the gap is proportional to the radius so as to have a constant $\dot{\gamma}$, $H(r) = r \sin\theta \implies \dot{\gamma} = \Omega/\sin\theta$. The apex of the cone should be truncated so that the smallest distance between the plates is at least 10 times bigger than the biggest particle in the system.

Small angle oscillatory shear Under small perturbations the equilibrium linear properties can be measured without affecting the system. A small amplitude oscillatory strain is therefore used to probe the linear elastic (G') and viscous moduli (G''). For a sinusoidal strain $\gamma(\omega,t) = \gamma_0 \sin(\omega t)$, the response of the system is:

$$\sigma(\omega,t) = G'(\omega)\gamma_0 \sin(\omega t) + G''(\omega)\gamma_0 \cos(\omega t) \tag{2.33}$$

The elastic response is in phase as in Hooke's law, $\sigma = G'\gamma$. The viscous dissipation is out of phase, $\sigma = (G''/\omega)\dot{\gamma} = \eta\dot{\gamma}$, as for Newton's equation for a purely viscous fluid.

Flow curves Ramps of varying shear rate as stress or viscosity are measured are referred to as flow curves. Some possible shear responses are: ideal Newtonian (viscosity is constant with $\dot{\gamma}$) shear thinning (viscosity decreases with $\dot{\gamma}$) and shear thickening (viscosity increases with $\dot{\gamma}$).

Boundary condition Previously we assumed $v(z=0) = v_{\downarrow plate} = 0$ and $v(z = gap) = v_{\uparrow plate}$. In other words, the boundary conditions are that the fluid immediately in contact with the solid plates has the same velocity as the plate. This is the stick (or no slip) boundary condition which is commonly assumed as a working condition. A second assumption was that flow field was linear along the gap, i.e. the flow is described by a single $\dot{\gamma}$. The stick boundary condition is not generally valid in nature [18]. Take the lower stationary plate ($v_{\downarrow plate} = 0$) and contiguous fluid velocity $v(z=0) = \dot{\gamma}b \neq v_{\downarrow plate}$, b is the slip length, a length derived from the extrapolation of the velocity to 0, pass the solid plate. Slip arises from low friction between the fluid and the interface compared to the cohesive forces in the bulk of the fluid. A common remedy that seems to work to overcome slip is to roughen the solid walls to increase friction.

Bibliography

[1] R. Pecora, *Dynamic Light Scattering: Applications of Photon Correlation Spectroscopy.* Plenum Press, New York and London, 1985.

[2] P. P. Lindner and T. T. Zemb, *Neutrons, X-rays, and light : scattering methods applied to soft condensed matter.* Elsevier, 2002.

[3] G. Maret, "Diffusing-wave spectroscopy," *Current Opinion in Colloid & Interface Science*, vol. 2, pp. 251–257, jun 1997.

[4] D. Weitz and D. Pine, "Diffusing-wave spectroscopy," in *Dynamic Light Scattering* (W. Brown, ed.), ch. Diffusing-, pp. 652–720, Oxford University Press, 1993.

[5] D. Pine, D. Weitz, J. Zhu, and E. Herbolzheimer, "Diffusing-wave spectroscopy: dynamic light scattering in the multiple scattering limit," *Journal de Physique*, vol. 51, no. 18, pp. 2101–2127, 1990.

[6] L. F. Rojas-Ochoa, S. Romer, F. Scheffold, and P. Schurtenberger, "Diffusing wave spectroscopy and small-angle neutron scattering from concentrated colloidal suspensions," *Physical Review E*, vol. 65, p. 051403, may 2002.

[7] J. Lekner, *Theory of Reflection of Electromagnetic and Particle Waves*. Springer Netherlands, 1987.

[8] H. Fujiwara, *Spectroscopic ellipsometry : principles and applications*. John Wiley & Sons, 2007.

[9] G. G. Fuller, *Optical Rheometry of Complex Fluids*. Oxford, 1995.

[10] H. A. Barnes, J. F. J. F. Hutton, and K. Walters, *An introduction to rheology*. Elsevier, 1989.

[11] R. G. Larson, *The Structure and Rheology of Complex Fluids*, vol. 150. New York Oxford, 1999.

[12] W. W. Hergert and T. Wriedt, *The Mie theory : basics and applications*. Springer, 2012.

[13] M. Bass and V. N. Mahajan, *Handbook of optics. Volume I, Geometrical and physical optics, polarized light, components and intruments*. McGraw-Hill, 2010.

[14] J. Ramírez, S. K. Sukumaran, B. Vorselaars, and A. E. Likhtman, "Efficient on the fly calculation of time correlation functions in computer simulations," *The Journal of Chemical Physics*, vol. 133, p. 154103, oct 2010.

[15] H. C. Van De Hulst, *Light scattering by small particles*, vol. 1. New York (John Wiley and Sons), London (Chapman and Hall), 1981.

[16] P. Lang and Y. Liu, eds., *Soft matter at aqueous interfaces*. Springer, 2015.

[17] F. Scheffold, R. Lenke, R. Tweer, and G. Maret, "Localization or classical diffusion of light?," *Nature*, vol. 398, pp. 206–207, mar 1999.

[18] M. Cloitre and R. T. Bonnecaze, "A review on wall slip in high solid dispersions," *Rheologica acta*, vol. 56, pp. 283–305, mar 2017.

Chapter 3

EW-DLS velocimetry

3.1 Introduction

Fluid flow near surfaces and interfaces has long attracted attention and the issue on the validity of boundary conditions in fluid mechanics is a longstanding one [1]. Consideration of the surface and interfacial contribution to the dynamics of fluid flow is relevant and can be applied towards an improved understanding of flow related to physiological, industrial manufacturing and even geophysical processes [2, 3, 4, 5]. Surface and interfacial contributions to the dynamics of fluid flow is therefore of importance in rheometry [6, 7]. Barnes [8] for example, gives an extensive review of the slip that occurs in two phase systems such as emulsions and particle suspensions.

The most common assumptions for flow along a stationary, solid surface -the no slip or stick boundary condition ($v(z = 0) = 0$, where v is the velocity of the flowing material and z the coordinate normal to the solid surface with 0 at the surface)- is often difficult to verify experimentally. Surface slip ($v(z = 0) \neq 0$) is a known phenomenon and occurs in a diverse range of systems spanning flow of articular cartilage in joints [9], polymer melt flow extrusion [10] and crustal motion within the earth's mantle [11].

In rheometry, the standard assumption of a linear flow profile and stick boundary conditions, is often difficult to verify through only rheological data [12, 13]. The study of rheological phenomena such as yielding, and its interplay with slip, require the ability to measure near wall flows. Therefore, simple efficient ways to detect and evaluate the importance of slip might be of interest. Beyond the detection of slip, the possibility to estimate near wall velocity profiles can allow for a better understanding of flow under confinement [14, 15, 16], and of the role of surfaces on bulk fluid flow [17, 18].

Various techniques have been developed to observe and study flow near solid surfaces [7]. These techniques are often microscopy based -such as particle image velocimetry (PIV) or total internal reflection fluorescence velocimetry (TIRFV) [19, 20, 21]-, and require contrasting phases for image processing analysis. Near-field laser Doppler velocimetry (NFLDV) as a time-resolved scattering method was used to study near surface flows and demonstrated for a simple pressure driven Poiseuille flow [22] in a microfluidic cell. The main purpose here is to demonstrate the feasibility and utility of coupling a rheometer with NFLDV.

In this chapter we show our implementation of the evanescent wave dynamic light scattering approach to velocimetry as developed by Loppinet et al. [22] on a commercial rheometer. We measured a variety of different samples to demonstrate the potential of the technique and were able to measure several extreme cases of near wall flow. Moreover we established a new analysis method based on the Fourier transform of the signal and supported our work with Brownian-Langevin dynamics simulations.

3.2 Evanescent Wave Dynamic Light Scattering Near Wall Velocimetry principle

Dynamic light scattering (DLS) is a well-established technique that probes motion of entities that scatter light [23]. It is mostly used for probing diffusion but can also probe velocities. We briefly recall the principle of time domain DLS (often referred to as photon correlation spectroscopy). More details on the following can be found in 2.1,2.2 and 2.4. The scattered intensity is collected at scattering angle θ_s (between the

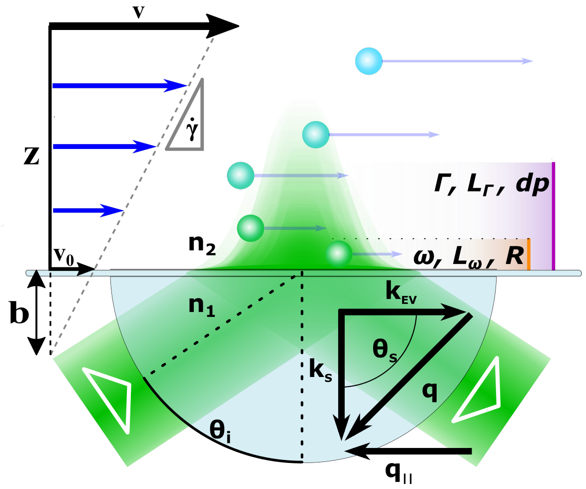

Figure 3.1: Working principle. 532 nm laser beam reflects on an interface between media with refractive indices n_1 and n_2 (we refer to the media by its refractive index) ($n_1 > n_2$) at an incident angle of $\theta_i > \theta_c$. An evanescent wave is produced in the lower refractive index medium, n_2 with a penetration depth, $dp \sim \lambda$. Medium n_2, contains tracer particles that move at velocites relative to n_2 as it is sheared by the top plate (at $z = gap$, not depicted). The tracers within the evanescent wave's volume scatter light into the far field, with wavevector $\boldsymbol{q}$, to the detector placed below the geometry oriented normal to the plane. The setup is aligned in order to have $\boldsymbol{v} \parallel \boldsymbol{q}_{||}$. Γ comes from the velocities averaged over dp, ω is the slowest velocity (of the tracers closest to the wall). In case of slip, b is non zero and we can see a shift on both ω and Γ.

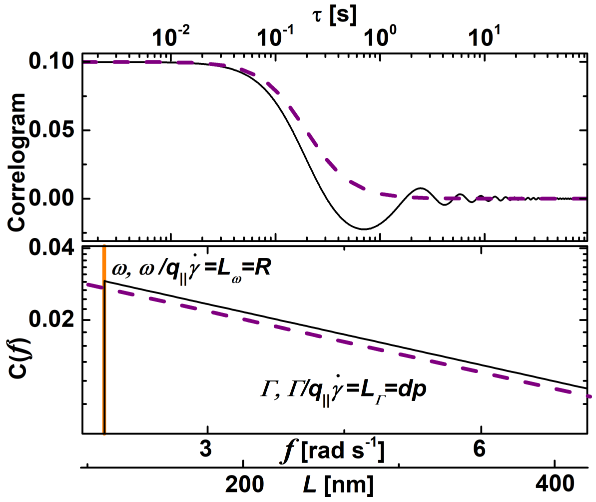

Figure 3.2: Theoretical data (up). The temporal correlation is a damped oscillation. The main frequency is ω and the damping rate corresponds to the averaged velocity distribution Γ. FT of simulated data, with frequency axis rescaled to units of length (down). The orange vertical line corresponds to the position of the theoretical cut-off, in this case 110 nm. The purple dashed slanted line has a slope of 1/300nm ($1/dp$).

incident and the scattered light) that defines the scattering wave vector $\boldsymbol{q}$, $(= \boldsymbol{k_2} - \boldsymbol{k_1})$. In quasielastic scattering, $|\boldsymbol{k_1}| = |\boldsymbol{k_2}| = k_0 n$ is assumed and $q = 2k_0 n \sin(\theta_s/2)$ where

n is the refractive index (RI) of the surrounding medium and k_0 is the wave vector amplitude in vacuum ($k_0 = 2\pi/\lambda$).

The relative motion of the scattering entities leads to temporal fluctuations of the scattered light intensity $I(q,t)$. The normalized intensity autocorrelation function is computed as, $\langle I(q,t)I(q,t+\tau)\rangle / \langle I(q,t)^2\rangle$ [23], and is the time domain spectrum of intensity fluctuations. The normalized intensity autocorrelation function is related to the space-time velocity correlation function. Diffusion results in overdamped correlation functions. Laminar flow produces periodic fluctuations and results in the presence of oscillations in the correlation function.

A variant of DLS introduced by Loppinet et al. [22] - based on the generation of evanescent waves (EW) that emanate from the total internal reflection (TIR) of light between media of different RI ($n_1 > n_2$) when the incidence angle is above the critical angle ($\theta_i > \theta_c$) - will be integrated into a shear-controlled rheometer. The scattering geometry is depicted together with all the relevant quantities in Fig. 3.1. The EW field penetrates the lower RI (n_2) medium and is utilized for investigating interfacial dynamics [24, 25]. The intensity, $I(z)$, of the EW field exponentially decreases in the probed medium as $I(z) = I_0 \exp(-z/dp)$, where dp is the penetration depth of the intensity, defined as the distance where the maximum intensity, I_0, is reduced by a factor of $1/e$ and z is the coordinate normal to the interface with 0 at the interface. The penetration depth depends on the refractive index mismatch between n_1 and n_2, and the incidence angle as follows:

$$\frac{1}{dp} = 2k_0 n_1 \sqrt{\sin(\theta_i) - \left(\frac{n_2}{n_1}\right)^2} \tag{3.1}$$

EW-DLS can be considered as a DLS experiment with a small interface-localized scattering volume, with incident wave vector $\boldsymbol{k_1} = \boldsymbol{k_{EW}} = k_0 n_2 \boldsymbol{x}$, scattered wave vector k_s and scattering wave vector $\boldsymbol{q} = \boldsymbol{k_S} - \boldsymbol{k_{EW}}$ [26].

In the case of ballistic motion (i.e. in the absence of diffusion, or when $Dq^2 < \boldsymbol{v} \cdot \boldsymbol{q}$)

with velocity field, $v = v(z)$, the field correlation function can be written as [22]:

$$g(\boldsymbol{q}, t) = \frac{\int_0^\infty c(z) \exp\left(-z/dp\right) \exp\left(i\boldsymbol{q} \cdot \boldsymbol{v}(z) t\right) dz}{\int_0^\infty c(z) \exp\left(-z/dp\right) dz} \tag{3.2}$$

where $c(z)$ is the concentration of point scatterers. We assume v is parallel to the shear plane and therefore use $\boldsymbol{q} \cdot \boldsymbol{v}(z) = q_{||} v(z)$, where $q_{||}$ is the projection of $\boldsymbol{q}$ over $\boldsymbol{k_{EW}}$, which coincides with $\boldsymbol{v}(z)$.

In the simplest case of a linear velocity profile of the scatterers, typical for shear flow , $v(z) = v_0 + \dot{\gamma} z$, with a shear rate $\dot{\gamma}$ and minimal velocity v_0 and a homogeneous distribution of the scattering probes, $c(z) = constant$, one obtains [22] the relation:

$$g(t) = \frac{\cos\left(\omega t\right) - \Gamma t \sin\left(\omega t\right)}{1 + (\Gamma t)^2} + i \frac{\sin\left(\omega t\right) + \Gamma t \cos\left(\omega t\right)}{1 + (\Gamma t)^2} \tag{3.3}$$

Two characteristic rate constants related to the flow profile emerge in the correlation function: $\omega = v_0 q_{||}$ which corresponds to the slowest, cut-off velocity v_0 of the scatterers closest to the surface, and $\Gamma = \dot{\gamma} q_{||} dp$, which corresponds to the velocity gradient in the penetration depth as the velocity $\dot{\gamma} dp = v(dp) - v_0$.

3.2.1 Signal mixing: heterodyne mode

In the most general experimental case, a part of the non-fluctuating intensity (static) coming from scattering by the glass surface is present in the measured intensity, corresponding to partial heterodyne conditions. In this case, the measured correlation function is given by the generalized Siegert relation [23]:

$$g_m(t) = (1 - B)^2 |g(t)|^2 + 2B(1 - B) Re(g(t)) \tag{3.4}$$

where $B = \sqrt{1 - A}$, A $(= g_m(t \to 0))$ being the maximum amplitude of the measured correlation function, relates to the ratio of the dynamic intensity of the moving particles to the static intensity of the solid surface's imperfections. From Eq. 3.4, we can take:

$$Re(g(t)) = \frac{\cos(\omega t) - \Gamma t \sin(\omega t)}{1+(\Gamma t)^2} \; and \; |g(t)|^2 = \frac{1}{1+(\Gamma t)^2} \tag{3.5}$$

A typical theoretical correlogram following Eqs. 3.4-3.5 is shown in Fig. 3.2, it is essentially a damped oscillation, with frequency corresponding to ω and damping rate to Γ.

In Fig. 3.3a, the measured correlation normalized by A, $g_m(t)/A$ for different levels of heterodyne, i.e. different values of A are shown. $B = 0$, (corresponding to no static intensity, i.e. homodyne conditions) gives $g_m(t) = |g(t)|^2$ which only depends on Γ. When $B \sim 1$ (corresponding to full heterodyne condition), $g_m(t) \sim Re(g(t))$. ω is only accessible when some static intensity is present ($B > 0$). A small heterodyne contribution ($\sim$5% or $B > 0.2$) is sufficient for the frequency ω to become visible in $g_m(t)$.

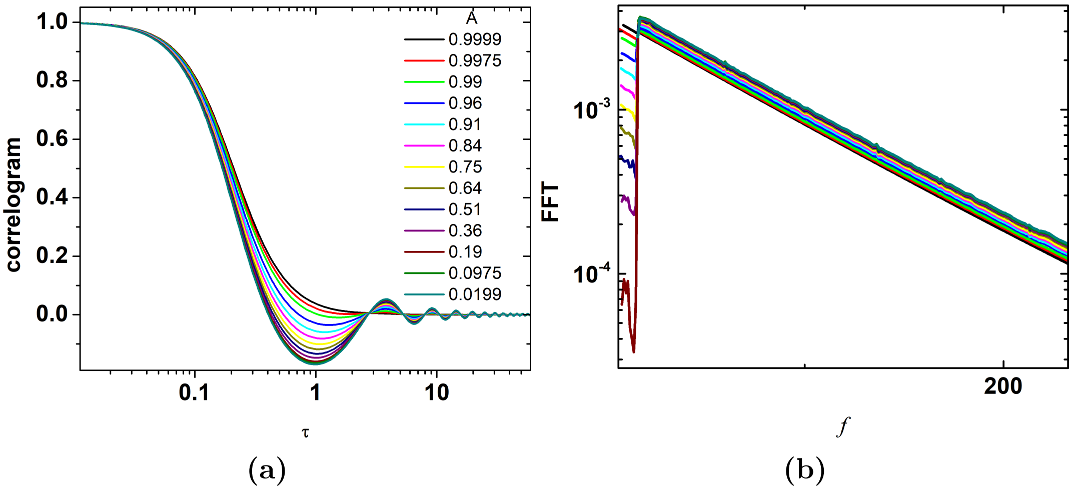

(a) (b)

Figure 3.3: (a) Correlograms according to Eqs. 3.4-3.5 with $\omega/\Gamma = 0.25$, as A (the fraction of dynamic intensity) varies, from homodyne, $A \sim 1$, to heterodyne, $A \sim 0.02$. (b) Corresponding FFT's.

The FFT's corresponding to Fig. 3.3a are shown on Fig. 3.3b. Both the cut-off frequency and the slope are not affected by the variation of A. The cut-off becomes easier to detect as A decreases.

In Fig. 3.4 we report the effect of heterodyne for different ω/Γ ratio, to check the detectability of ω in different conditions. This was done by varying Γ while keeping

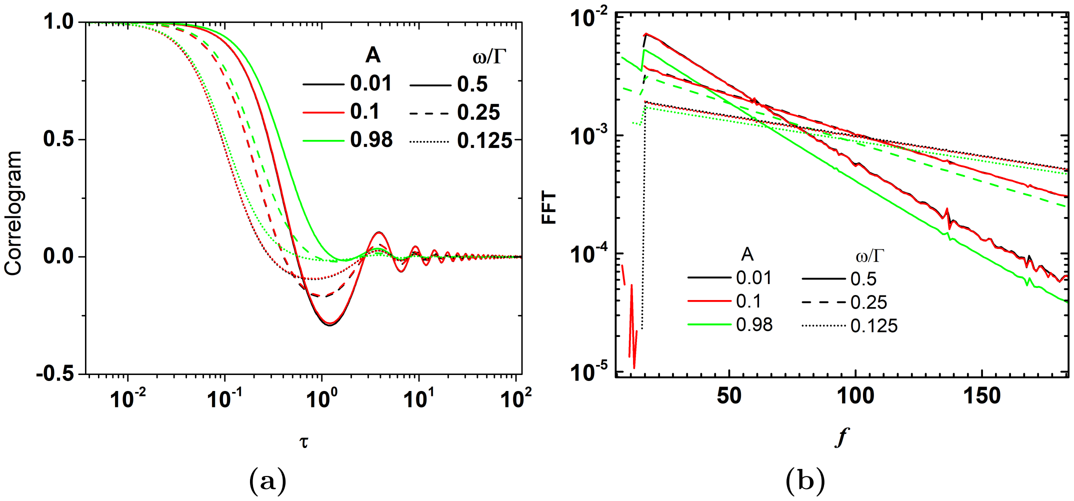

Figure 3.4: (a) Correlograms according to Eqs. 3.4-3.5.Varying A and ω/Γ. (b) Corresponding FFT's.

ω constant. Smaller Γ and higher heterodyne levels make it easier to resolve the cut-off frequency. Obviously noise and signal contamination can become an issue when determining ω for small A.

3.2.2 Rescaling frequencies into length: L

Using a rheometer, a broad range of shear rates and flow conditions are accessible. To allow comparison, we choose to scale the measured near wall velocities by the nominal (rheometer) shear rate ($\dot{\gamma}_n = v_{plate}/gap$) to produce an effective length scale. In general, the factor $L = v_{NW}/\dot{\gamma}_n$, which gives $L_\omega = \omega/\dot{\gamma}_n q_\|$ and $L_\Gamma = \Gamma/\dot{\gamma}_n q_\|$. In the case of a linear profile $\dot{\gamma} = \dot{\gamma}_n$, $L_\omega = v_0/\dot{\gamma}$ and $L_\Gamma = dp$. The scaled lengths are bound by the imposed experimental lengths as, $0 < L_\omega, gap$ and $L_\Gamma \leq dp$.

We are using here particle velocimetry on a material containing monodisperse spherical particle tracers of radius R. The probed velocity profile is that of the tracers, which does not always coincide with that of the underlying material. In particular, the particle center of mass cannot approach the wall closer than R. Therefore, the slowest velocity in the system corresponds to the particle with center at distance R from the wall. In this case, hydrodynamic interaction of the tracers with the wall leads to a slowdown of the tracer velocity (compared to the one of the fluid) (with the approximate equation $v(z)/(\dot{\gamma}z) \approx 1 - 5/16(z/R)^{-3}$, see Fig. 3.5) [27]. The measured slowest velocity v_0 of the nearest to the wall tracers, with center of mass situated at a distance R from the wall should be about 70% of $\dot{\gamma}R$ i.e. $L_\omega \approx 0.7R$.

The defined length scales can be used to describe a variety of near wall flow. Stick boundary condition is characterized by $L_\omega \approx 0.7R$, $L_\Gamma = dp$. Weak slip is described as $L_\omega \geq 0.7R$ with a finite slip length having no significant consequences on the rheological measurement and $L_\Gamma = dp$, $(\dot{\gamma} = \dot{\gamma}_n)$. Strong slip is given as, $gap > L_\omega \gg R$ (or $L_\omega \sim gap$), and $L_\Gamma < dp$. The existence of slip is expected to affect the shear rate, so that the real shear rate can become less than the nominal shear rate $\dot{\gamma} < \dot{\gamma}_n$.

Given the specifics of our experimental conditions where the probe particle radius is comparable to the penetration depth, $R \sim dp$, the two velocities/lengths L_ω and L_Γ are expected to have similar values for no slip or weak slip. In case of strong slip, L_ω could become much larger than L_Γ resulting in much smaller damping in the correlation function.

Slowest velocity and slip length: A commonly used way to evaluate slip is through the use of slip length defined as $b = v_0/\dot{\gamma}$ [28]. This is apparently equivalent to L_ω. However, the slip length b usually refers to the material and not to the tracer velocity. Measuring the material slip length from the tracer velocity requires careful modeling as done in [21] for the case of simple (Newtonian) fluids.

Influence of $c(z)$ and $v(z)$: The measured correlation function depends on $c(z)$ and $v(z)$. Eq. 3.3 assumes homogenous particle distribution and linear flow velocity, namely $c(z) = constant$ and $v(z) = v_0 + \dot{\gamma}z$. The technique does not unequivocally resolve concentration distributions $c(z)$ and especially the position of the slowest particles that give rise to L_ω. The effect of non-uniform $c(z)$ and $v(z)$ have been considered in the case of near wall velocimetry and fluorescence measurements [29]. If the spatial distribution of particles is not constant and the flow profile is non-linear then Eq. 3.3 is no longer valid. As the slowest particles are situated closest to the wall, we may nonetheless expect this slowest velocity to be detectable as a low velocity cut-off even in more complicated cases. Similarly, based on Eq. 3.2, the early decay of the correlogram should remain an average velocity gradient within the penetration depth.

In case of uniform distribution of scattering probes and linear velocity profile, Eq. 3.2 has the analytical solution Eq. 3.3. In other cases of $v(z)$ and $c(z)$, $g(t)$ does not have a simple analytical expression. To test the effect of nonuniform probe particle distribution $c(z)$ and different $v(z)$ and especially the effect of hydrodynamic interaction between the probe and the hard wall on $g(t)$, we implemented Brownian dynamic simulations in the spirit of [21] to provide a numerical solution of Eq. 3.2. The routine implements the probe particle motion and computes the correlation function $g(t)$, providing the numerical solution of Eq. 3.2. The procedure, described in section 3.4 provided a good way to check the influence of various parameters on $g(t)$.

The computed $g(t)$ for a range of concentration profiles and including the effect of the hydrodynamic interaction with the wall [27] and the effect of low polydispersity are shown in 3.4.1 and 3.4.2 (Figs. 3.5-3.8). Simulations also allowed to check the validity of the Fourier transform analysis described below.

3.3 Fourier transform spectrum analysis of the correlogram

In this work we introduce the Fourier transform (FT) of the intensity auto-correlation, $C(f) = Re(FT(g_m(t)))$, as a tool to analyze EWDLS velocimetry data. This is analogous to power spectrum analysis often used in velocimetry [30, 31]. The frequency of $C(f)$ relates to the probed velocity distribution. Using $C(f)$ is especially convenient in the case of noisy data, as Fourier filtering can be readily applied. In EWDLS under flow, velocities are exponentially sampled over dp and the distribution of velocities is truncated on the slower end (the tracer nearest to the wall). It follows that $C(f)$ in relation to Eq. 3.3 consists of a dominant exponential decay of rate Γ, which corresponds to the averaged velocity distribution over dp truncated at the lowest frequency ω, which corresponds to the slowest velocity ($C(f) \sim \exp(-f/\Gamma)$ for $f > \omega$).

$$C(f) = \sqrt{\frac{\pi}{2}}\frac{1}{\Gamma}(1-B)\left(1-B\left(1-2\exp\left(\frac{\omega}{\Gamma}\right)\right)\right)\exp\left(\frac{f}{\Gamma}\right) \tag{3.6}$$

In practice, the $FT(g)$ did not show discontinuity, but a very marked asymmetric maximum. The frequency of the broad maximum was taken as a value for ω. Γ can be obtained from measuring the slope towards high frequencies in a semi-log representation. We did not attempt to fit an analytical solution to the FFT. Such a fit cannot be expected to provide a better fit than the fit of $g_m(t)$ in the time domain. As mentioned above, the cut-off was determined manually. Our choice of analysis was justified on the generality of the two features: low frequency cut-off and slope of $\log(C(f))$ vs f.

Of most relevance is that the dominating features of $C(f)$ are generic beyond Eq. 3.3. Simulations show that indeed both Γ and ω remain assessable through slope and cut-off, rather independently of the precise $c(z)$ and $v(z)$. $C(f)$ is a valuable analytical tool that straightforwardly resolves the cut-off velocity and near-wall velocity gradient. A typical theoretical spectrum $C(f)$ is displayed for the case of hard sphere at hard wall with and without hydrodynamic interaction in Fig. 3.2.

The integrating and averaging nature of EWDLS makes it difficult to discern the proper tracer's signal from "defects" within the sample such as dust, aggregates and bubbles, or even contributions to $g_m(t)$ from vibrations and stray light. We found the Fourier transform analysis to be very helpful to spot possible noise signals, in a Fourier filtering approach. In the frequency domain, noise artefacts either fall outside expected signal range or can be spotted to have unphysical characteristics.

3.4 Brownian-Langevin dynamics simulations

The Eq. 3.2 relates the measured correlation function with the concentration and velocity profiles $v(z)$ and $c(z)$, generally Eq. 3.2 does not have analytical solutions. We implemented a simple Brownian-Langevin dynamics simulation to numerically compute the correlation function $g(t)$. We used it to check the effects of the parameters like the concentration profile $c(z)$ or the velocity profile $v(z)$ on the $g(t)$. The simulations were not intended to produce an exact representation of the real experiment but to provide $g(t)$ in cases where they cannot be simply evaluated analytically.

The implemented motion of independent tracers is very similar to the ones described in [21], $v(z)$ and $D(z)$ can be included to account for the various hydrodynamic slowdowns on diffusion and flow, a potential $U(z)$ between the tracer and the wall can be included giving rise to an equilibrium $c(z)$. Interaction between the particles is not considered. The simulation was done in 2D (x, z) with periodic boundary conditions for the x axis and reflective boundary conditions for the z-axis. The following Langevin equations of motion was implemented for every particles.

$$x(t+dt) = x(t) + f_x\sqrt{2D_x(z)dt} + v(z)dt \tag{3.7}$$

$$z(t+dt) = z(t) + f_z\sqrt{2D_z(z)dt} + \frac{dD_z(z)}{dz}dt + \frac{D_z(z)F(z)}{kT}dt \tag{3.8}$$

Where f_x ,f_z are random numbers following a Gaussian distribution centered at 0, with standard deviation of 1.

The position r_n ($= x_n\boldsymbol{x} + z_n\boldsymbol{z}$) of 10^3 independent particles was computed at every time step and the scattered field $E(t) = \sum_n E_n \exp\left(i\boldsymbol{q}\cdot\boldsymbol{r_n}\right)$ where $\boldsymbol{q}$ was taken to correspond to experiments (detection at 90° from the interface) and $E_n = R_n^3 \exp\left(-z_n/2dp\right)$ corresponds to the scattered field of a particle of radius R_n at position z_n in the evanescent wave of penetration depth dp. $Re(E(t))$ and $Im(E(t))$ were fed to a multiple-tau software correlator that computes the normalized autocorrelation functions separately and then the two were added; the cross terms were not calculated.

Typical simulations were ran over ensembles of 10^3 particles, each ran for 10^4 steps and then replaced by another ensemble to better map the space. The whole process was repeated at least 800 times. The diffusion coefficient D_0 was set small enough to only observe the flow correlation (high Pe number). The finite diffusion helped to obtain a better sampling of space.

The simulation was implemented on Python. The correlator code is based on an original the C++ code kindly provided by J. Ramirez [32] translated into python. The minimum tau in the correlation was equal to 1 time-step in the simulation. The correlator used 128 channels, in a multiple tau scheme. It corresponded to half the channels of the real data. The numerical $g(t)$ were analyzed through FFT using the same approach as for the experimental data described below.

3.4.1 Effect of near wall hydrodynamic interactions, non uniform v(z) and D(z)

In the case off near wall flow, the hydrodynamic interaction between the wall and the particle results in a slow-down of the particle. The particle then does not have the velocity that the underlying fluid would have in its absence. This effect follows the approximate expression $v(z)/(z\dot{\gamma}) \approx 1 - 5/16(z/R)^{-3}$ [27] for the case of a sphere under flow, parallel to a wall, in a viscous fluid (see inset in Fig. 3.5a for a plot of the previous equation). Similarly, the in plane (x) and out of plane (z) diffusion coefficients are

$$D_x(z) = D_0\left(1 - \frac{9}{16}\left(\frac{z}{R}\right)^{-1} + \frac{1}{8}\left(\frac{z}{R}\right)^{-3} - \frac{45}{256}\left(\frac{z}{R}\right)^{-4} - \frac{1}{16}\left(\frac{z}{R}\right)^{-5}\right) \tag{3.9}$$

$$D_z(z) = D_0\left(\frac{\left(6\left(\frac{z}{R}-1\right)^2 + 2\left(\frac{z}{R}-1\right)\right)}{\left(6\left(\frac{z}{R}-1\right)^2 + 9\left(\frac{z}{R}-1\right) + 2\right)}\right) \tag{3.10}$$

As seen on Fig. 3.5b for the case of constant $c(z)$, the hydrodynamic slowdown has the effect of shifting the cut-off towards slower velocities as could be expected (∼30%) but also of "rounding" the cut-off peak.

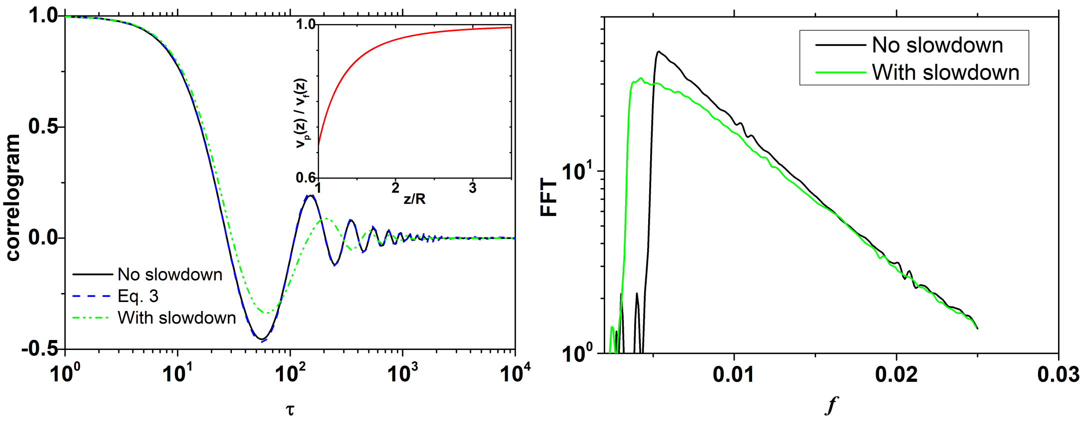

(a) (b)

Figure 3.5: Simulation on the effect of the hydrodynamic slowdown according to the method of reflection (Goldman) with $dp = 1\ R$. The rest of the simulations include the hydrodynamic slowdown. Here we visualize the magnitude of the effect of this slowdown. (a) Simulated correlogram with and without slowdown, and comparison with the result of Eq. 3.5. (The inset on the left figure is the slowdown according to Goldman) (b) Fourier transform of the simulated results.

3.4.2 Effect of tracer polydispersity

The simulations also allowed testing for the possible effect of tracer polydispersity. The smaller particles are expected to be able to come closer to the wall and get a slower cut-off velocity compared to larger ones. Tests for a 10% polydispersity are shown in Fig. 3.6. The effect appeared rather small for this polydispersity. Overall, there is a distribution on the cut-off and a 10% speed up of the maximum.

EW-TIR velocimetry measurements have a bias due to tracer size variations as discussed by Wang et al. in [29]. The bias has its origins in the different intensity as the particle size changes (R^6 for scattering and R^3 for fluorescence in terms of intensity). The strong size dependence of the scattering is of course weighted by the exponential decay of the evanescent wave.

3.4.3 Effect of c(z)

An uneven distribution of the probe particles is expected to have an impact on the correlation function $g(t)$. Uneven $c(z)$ would arise in case of interaction between the

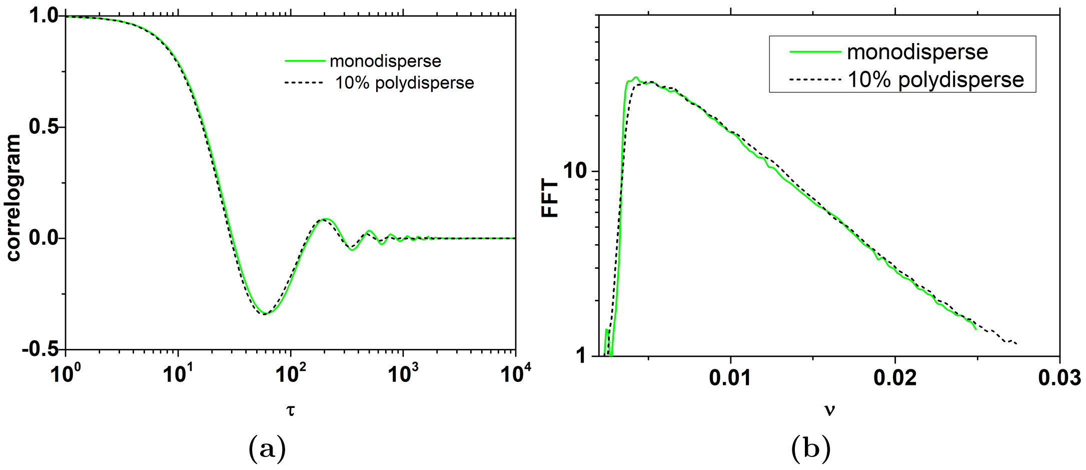

Figure 3.6: Simulation on the effect of polydispersity on the correlation function. $\langle R \rangle = 1$, $\sigma = 0.1$. The black dashed curves include polydispersity. The green curves are for the monodisperse system. (a) Correlograms. (b) FFT of the correlograms.

wall and the particles. For an interaction potential $U(z)$, the particles distribution will reach an equilibrium $c(z)/c_0 = -\ln(U(z)/kT)$.

Rather than applying a potential $U(z)$, we distributed the particles according to the desired $c(z)$ at time 0. Then, simulations were run with no potential for short enough time so that $c(z)$ remained close enough to the desired distribution as the particles stay close to their initial positions (within ∼2% of R for the values used here).

Different concentration profiles $c(z)$ have been explored and 3 different dp (0.5, 1 and 2 R) have been used. Fig. 3.7 shows the different $c(z)$ used covering near wall enrichment and depletion. The functional form of the profiles is:

$$a\left(1-\exp\left(-\frac{\left(\frac{z}{R}-1\right)}{k_1}\right)\right)+(1-a)\exp\left(-\frac{\left(\frac{z}{R}-1\right)}{k_2}\right) \tag{3.11}$$

These are set for $k_{1,2} = \{0.1, 0.2, 0.5, 1\}$ and $a = \{0, 1\}$ and k_1=0.05, k_2=0.3 and a=0.7. Follow the line styles in Fig. 3.7 to read Figs. S6 and S7.

The overall effect of decreasing $c(z)$ (attractive $U(z)$) is that there are more slower particles and the FFT regains a sharp cut-off (See Fig. 3.5 and 3.8). It looks like an apparent cancellation of the effect of the hydrodynamic slowdown. The depleted $c(z)$ (repulsive $U(z)$) strongly rounds the cut-off. In practice, ω was manually taken

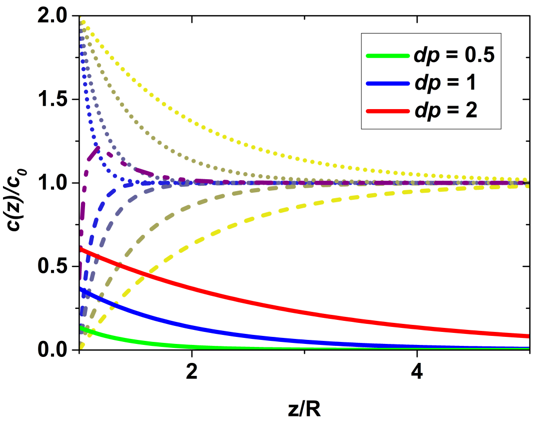

Figure 3.7: Different $c(z)$ and evanescent wave profiles used in the following simulations. Use these line styles to read the following graphs. The full lines refer to the evanescent wave field amplitude.

as the maximum in $C(f)$ and Γ was obtained from the slope "away" from the cut-off. The penetration depth affects the slope on the FFT as it is expected but otherwise it doesn't alter the qualitative picture on the data.

It is clear from these simulations, that the influence of $c(z)$ and $v(z)$ cannot be separated without complementary information. However, the overall shape of the FFT is conserved and ω and Γ can still be obtained.

3.5 Rheometer: EW-DLS Implementation

The optical set-up mounted on the rheometer to measure EWDLS under flow is depicted schematically in Fig. 3.9 and is described below.

A 100 mW 532 nm Nd:YAG laser beam (Torus 532 from Laser Quantum), B in the figure, was focused (f = 20 cm) with lens F on the bottom glass plate of the rheometer through a truncated (-1 mm) semi cylindrical lens G of radius 15 mm (Schott) assembled with a 1 mm disposable borosilicate microscope glass slide (34 × 50 mm) in optical contact through refractive index matching oil.

The incoming light was s-polarized (the electric field lies parallel to the interface). The incidence angle is varied by using the beam steering mirrors M1 and M2 and by changing the vertical position of the lens (F). The span of incidence angles was from

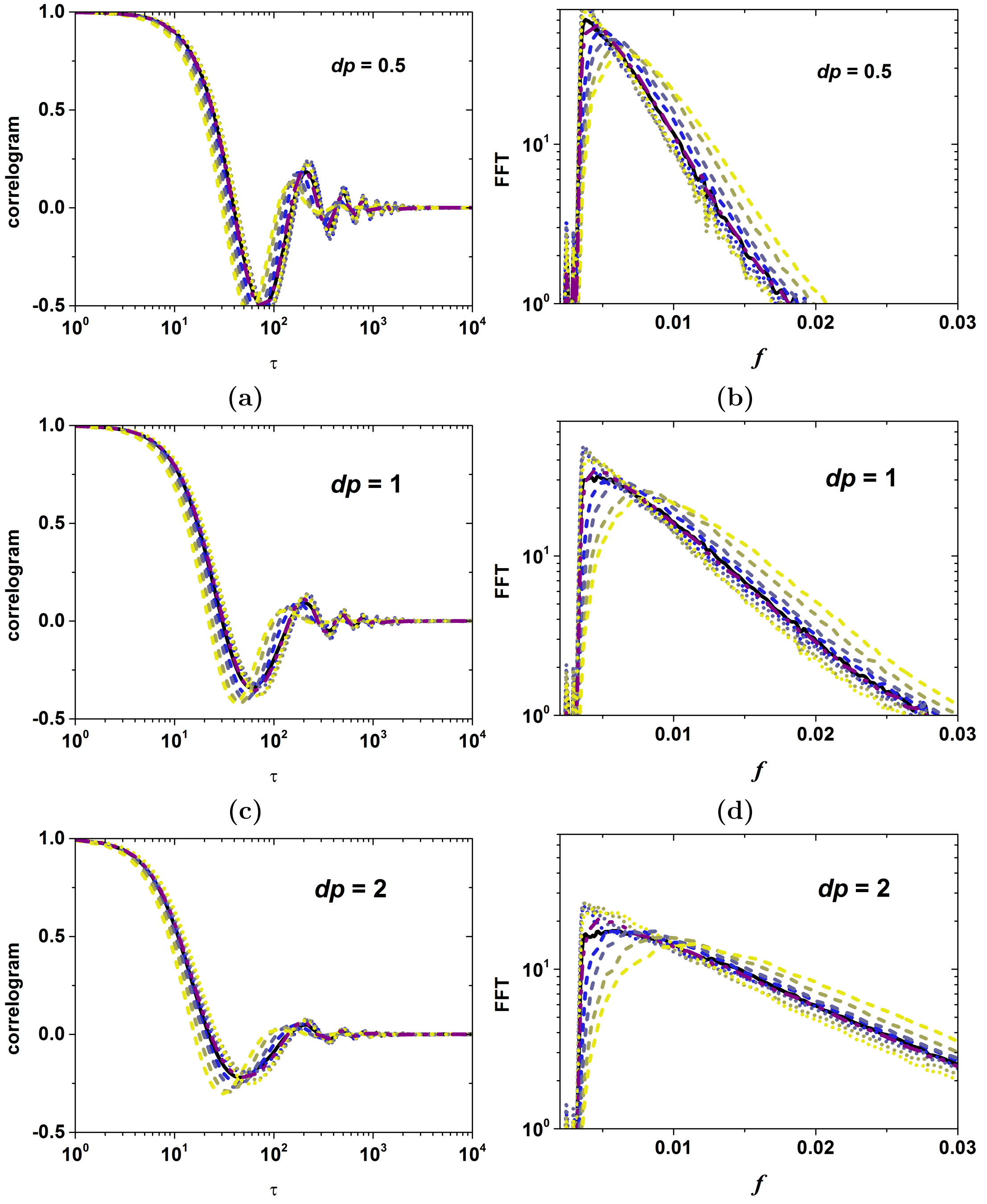

(a) (b) (c) (d) (e) (f)

Figure 3.8: Correlograms obtained for the $c(z)$ in Fig. 3.7 and real parts of the respective FFT's. (a,b) $dp = 0.5\ R$ (c,d) $dp = 1\ R$ (e,f) $dp = 2\ R$.

60° to 85°. Given the refractive index of the glass plate, n_{glass}= 1.52, it is possible to measure samples of n from 1.31 to 1.51. (The limit is set by the critical angle $\theta_c = \arcsin\left(n_{sample}/n_{glass}\right)$.) The incidence angle was estimated by simple geometrical arguments from the geometry of the setup in Fig. 3.9 typically with precision of $\sim 0.1°$.

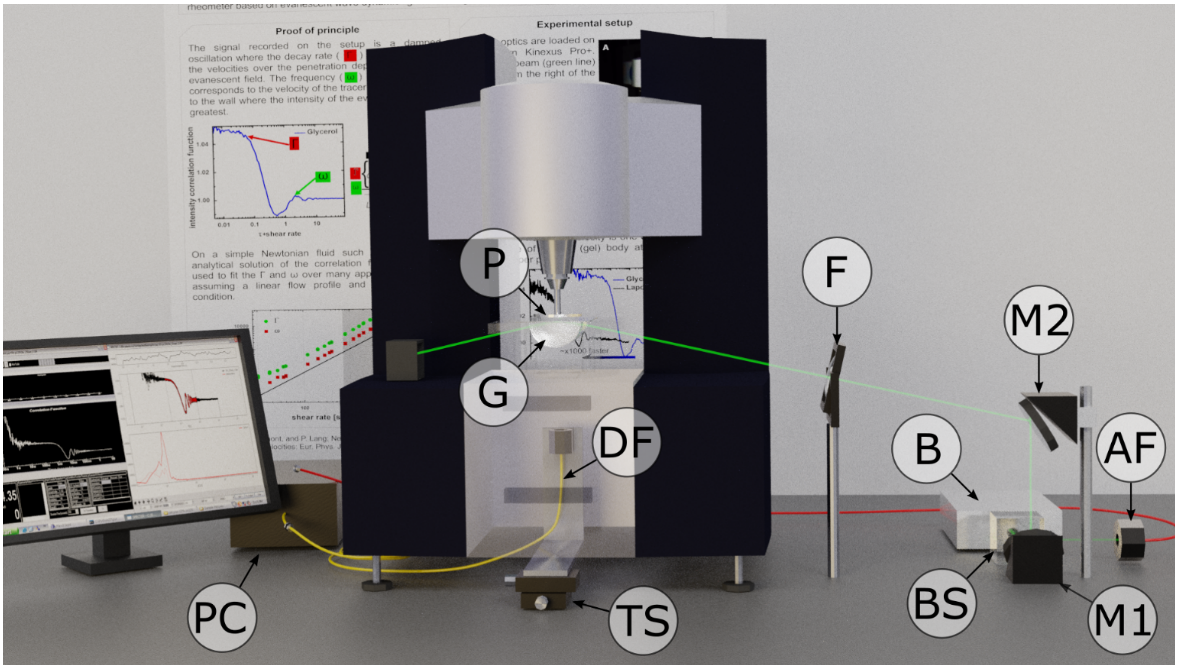

Figure 3.9: Setup description. B: 532 nm Nd:YAG laser source. BS: beam splitter. A fraction of the beam is sent to the detection spot during the alignment through the alignment fiber. AF: alignment fiber. M1 and M2: beam steering mirrors. F: focusing lens. G: semi-cylindrical -1 mm truncated lens and 1 mm glass slide (serves as a bottom plate). A detailed view on G can be seen on Fig.1 (a). P: top plate geometry. DF: detection fiber. TS: alignment translation stage. PC: PMT, correlator and PC (in real life they are separate units).

The scattered light was collected at 90° from the sample plate (equivalently, at 90° from $\boldsymbol{k}_{\boldsymbol{EW}}$) through a monomode optical fiber DF fitted with a collimator (LPC-0.1-633-4/125-S-0.396-1.8GR-25-5-3-4) and detected by a PMT (Hamamatsu, provided with the correlator unit) that operated in photon counting mode. For the samples presented here $q_{\|}/n_{sample} = 0.0118nm^{-1}$.

The detection fiber was aligned with the reflection spot by matching a portion of the beam (using the beam splitter BS) sent back through the detection fiber to the reflection spot. Once in working conditions, the position of the detection was finely tuned using a translation stage TS to maximize the intensity. The PMT output was fed to a digital correlator (model Flex01LQ-12 from correlator.com) having 1088 delay channels in a multi-tau scheme [32] with a fastest delay time of 12.5 ns. The correlator computes a normalized intensity correlogram $\langle I(t)I(t+\tau)\rangle/\langle I(t)^2\rangle$.

As mentioned previously we performed Fourier transforms of the measured correlation functions. This was done using a FFT routine, with special care to account for the non linear delay time spacing on the multi-tau correlator.

The multiple-tau correlator is very useful in the case of large variation of characteristic times. However, the non-uniform time spacing in the multi-tau correlator forbids the straight use of the FFT. Equally spaced correlations were therefore obtained through linear interpolation. The region of interest was determined ($\tau_{min} < \tau < \tau_{max}$). The interpolation time was defined as $dt = \tau_{min} - \tau_{min-1}$ and the number of equally spaced points was then $n = int((\tau_{max} - \tau_{min})/dt)$ where int is the rounding function. The python numpy.fft.rfft library was used to compute the FFT. The resulting transform was multiplied by dt.

For convenience, in some cases we rescaled the frequency axis by $q_{\|}\dot{\gamma}_{nominal}$ into units of length (referred to as L).

It is worth noting that the scheme used is subject to aliasing [33]. Aliasing is a consequence of under-sampling (poor time resolution), and is not taken care of by the interpolation (which, being linear, does not add information). It happens every time one records an oscillation with a sampling frequency less than $2 * frequency$ of the oscillation. Moreover, the FFT of a multi-tau signal suffers from numerical errors given by the sampling time and edge effects.

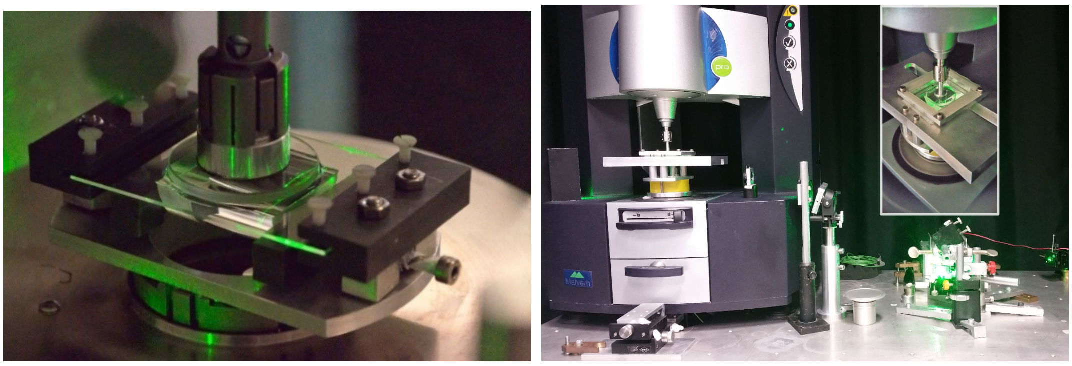
(a) Rheometrics DSR. **(b)** Malvern Kinexus Pro+.

Figure 3.10: Credit to Antje Larsen for the photographs.

The generic applicability of the technique was demonstrated on two different stress-controlled rheometers: a Rheometrics DSR (Fig. 3.10a) and a Malvern Kinexus Pro+

(Fig. 3.10b). The rheometers were used in strain-controlled mode to keep the shear rate constant. The bottom plate arrangement was mechanically fitted to the rheometers. The upper plate consisted of a flat optical fused silica window (diameter = 34 mm / thickness = 3 mm) glued on the rotational fixture of the rheometer which allowed for sample visualization and for maintaining symmetric boundary conditions.

Parallel plate geometry was used, and the nominal shear rates we report correspond to the shear rates at the position of detection. Typical gaps ranged from 200 to 400 μm while shear rates went from 0.1 to 1000 s^{-1} and the corresponding angular velocities from 0.002 to 20 rad/s. The reported measurements were obtained during steady state flow (constant stress / constant shear rate i.e constant rotational velocity). Non-uniform velocity present in parallel plate geometry and possible consequences on the data were not considered. Accounting for beam dimension ($\sim$500 μm) and radial position, the variation of shear rate within the scattering volume was below 1% deviation from the average.

3.5.1 Scattering volume

The scattering volume is fixed by the beam foot print, the detection foot print and the penetration depth. The penetration depth dp of the evanescent wave is of the order of the wavelength of the light. On the reported data, it varied from 66 to 300 nm. The "*imaged area*" is defined as the intersection of the beam footprint (A_b) and the detection area (A_d) (See Fig. 3.11.). A_b was typically $\sim 340 \times 540\ \mu m^2$ for an incidence angle of 72°, with less than 20 μm of variation on the long axis over the usable range of angles. A_d was typically $510 \times 340 \mu m^2$ as estimated from the detection fiber and lens characteristics. Both areas were non-symmetric Gaussians (the asymmetry originates from the lensing due to the semi-cylindrical substrate) at 90° from each other. The scattering volume is approximately $dp \times$ "*imaged area*".

The concentration of tracers was chosen to ensure that the number of tracer particles in the scattering volume was large enough to avoid number fluctuations, sufficient to provide good statistics, and not too large to influence the sample properties. For tracer particle volume fractions larger than 10^{-4} and 100 nm radius, the volume guarantees ∼500 particles per scattering volume, which should be enough to minimize the effect of number fluctuations.

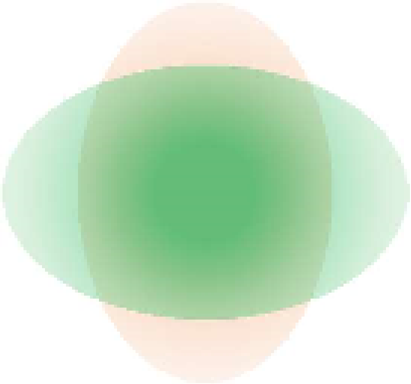

Figure 3.11: Cross sections for the detection and the footprint of the evanescent wave. The elliptical shapes are a result of the use of a semi-cylindrical lens at the lower plate (see Figs. 3.1 and 3.9). The illumination sectionvaries according to the incident angle but by no more than 10 μm on the long axis diameter, over the usual incident angles.

In the case of steady flow, typical measurement time is set by the characteristic time/frequencies to be measured and by intensity considerations (signal to noise). In the case of non-steady state flow, the measured correlogram reflect an average over the time of the measurement.

When the scattering intensity is high enough and the dynamics are fast, well resolved correlation can be measured fast and one can hope to resolve the evolution of the local flow (for example in start-up flow). Good statistics could be reached in a few seconds' measurement times.

3.6 Proof of principle on a Newtonian fluid

Newtonian fluids are first considered as proof of principle. The flow properties are described solely by a constant viscosity independent of shear rate with the anticipation of stick boundary conditions. A mixture of glycerol (76%w) and water (24%w) was used as a model fluid and is referred to as the Newtonian reference throughout the paper.

3.6 Proof of principle on a Newtonian fluid

Polystyrene (PS) latex spheres (Rh=110 nm) and gold nanoparticles (GNP) (Rh=17 nm) were used as flow tracers. The refractive index (n=1.437) was measured by an Abbe refractometer at 589 nm. Results with incidence angle $\theta_i = 71.8°$ corresponding to a dp of 290 nm are reported.

In Fig. 3.12a we show the measured intensity correlograms (symbols) for the Newtonian reference loaded with PS tracers at different shear rates, in the standard semi-log representation. The data could be well fitted using Eqs. 3.3-3.4 using ω and Γ as well as one amplitude (B in Eq. 3.4) parameter as fit parameters. The best fits are shown in Fig. 3.12a (lines). The correlograms can be rescaled by Eq. 3.4 to get the real part of the field autocorrelation function and by multiplication of the time by the nominal shear rate. In Fig. 3.13 we can see a good overlap when the data is rescaled showing how the velocities scale linearly with the nominal shear rate. The obtained values of ω and Γ are reported in Fig. 3.14a over the measured three decades of nominal shear rate. Both ω and Γ showed linear dependence with the shear rate. The evolutions when rescaled by the apparent shear rate are shown in Fig. 3.14b and found to be mostly independent of the shear rate, demonstrating that the measured near wall velocities were mostly (uniquely) imposed by the applied shear rate.

Though the time-based analysis was successful, the Fourier transform analysis, i.e. $C(f)$ was also applied. Experimental $C(f)$'s are shown in Fig. 3.12b where the frequency axis has been rescaled into units of L, using the velocity, $1/q_{\|}\dot{\gamma}$ (corresponding to the top plate velocity). The vertical shift between the different data is a result of the FT, which is proportional to Γ^{-1}, so that lower values of Γ appear higher in the plot. $C(f)$ allowed a direct reading of the low frequency cut-off ω (or the apparent slip length). The rate Γ can be obtained from the slope of $C(f)$ vs $\log(f)$ directly apparent in the semi-log representation.

The scaling of the average velocity with the shear rate is directly apparent from Fig. 3.12b (similar slope for all correlograms), as well as the low L cut-off. It clearly evidences the constant apparent slip length ($v_0/\dot{\gamma}$) and NW velocity gradient ($\Gamma/\dot{\gamma}$)

as found in the time-domain analysis and shown Fig. 3.14b. The lines in Fig. 3.12b correspond to the FFT of the best fit shown in Fig. 3.12a. Also depicted in Fig. 3.12b, are a vertical line at $L_\omega = Rh$ (orange dotted line) and the slope $1/L_\Gamma$ ($1/dp$ =1/290 nm^{-1}) slope (purple dotted line).

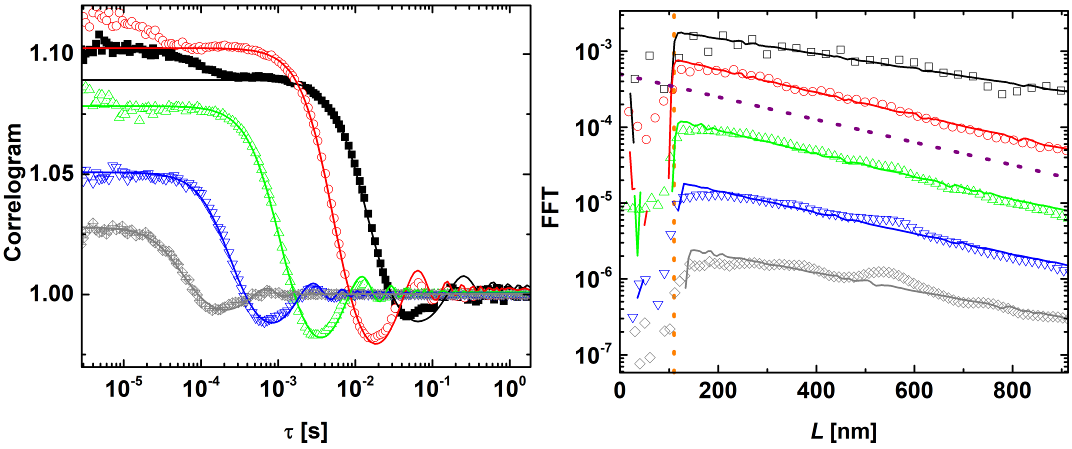

(a) (b)

Figure 3.12: (a) Correlograms for the Newtonian reference seeded with 110 nm PS spherical particles. The oscillations move towards shorter times with increasing shear rate. (b) FFT of the data on the left. The frequency axis has been rescaled into units of length. The vertical shift is natural to the data scaling as $1/\Gamma$ times a nonlinear function in the amplitude and the ratio ω/Γ. The grey lines show the predicted position of the cutoff (Particle Rh= 110 nm) and the slope for the Γ distribution ($1/dp$= 1/290nm). Shear rates (s^{-1}): 9.9, 40, 200, 900, 2800.

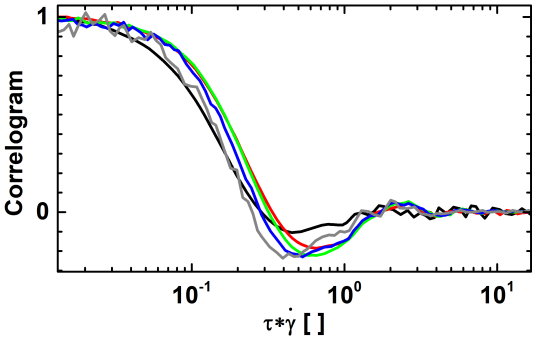

Figure 3.13: Real part of the correlation function of the data shown in Fig. 3.12a according to Eq. 3.4. The time axis was rescaled by the nominal shear rate.

3.6.1 Shear rate dependence

The characteristic rate constants rescaled by the shear rate and the length scale (R and dp) are shown in Fig. 3.14b over the shear rate range. The error accounts for various random errors (fit error, shear rate) and systematic errors (θ, dp, q, n). The random error is small, of the order of the symbol size (i.e. few %). A relatively large uncertainty on the dp (30%) occurs from the proximity of the incidence angle to the critical angle on these experiments. The systematic error accounts for errors from the gap and shear rate related to the equipment specifications of the rheometers used (Rheometrics DSR and Malvern Kinexus Pro+).

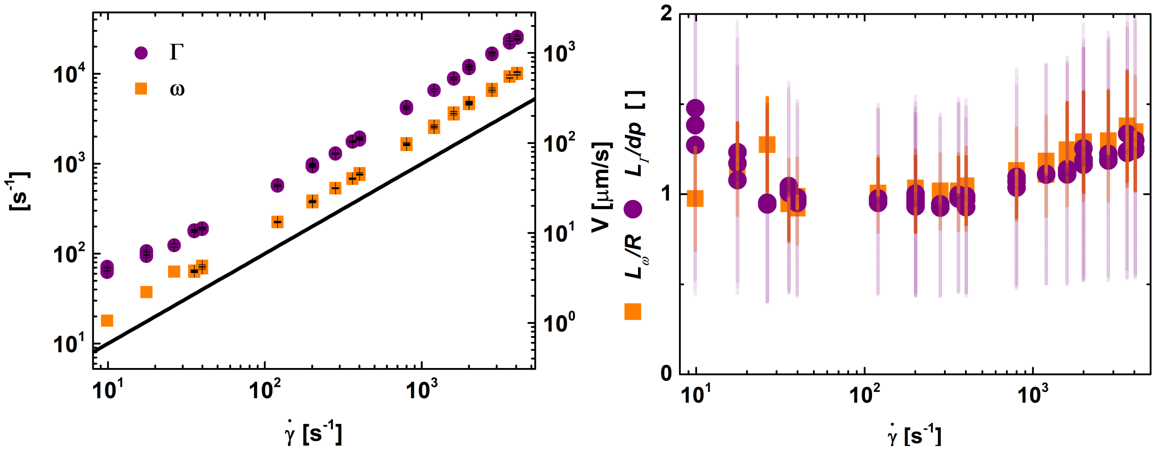

(a)

(b)

Figure 3.14: (a) The left y-axis shows Γ and ω as obtained from fitting the analytical solution to the raw data for the Newtonian reference loaded with PS 110 nm *Rh* particles. The right y-axis shows the values in units of absolute velocity, correspondingly v_Γ and v_ω. The error bars come from the fit minimization algorithm. (b) L_Γ and L_ω (Γ and ω rescaled into units of length (division by $q_{||}\dot{\gamma}_{nominal}$) and further divided by the expected values dp and R. The average error bars take into account possible misalignments and are larger on L_Γ/dp due to the strong variation of dp close to the critical angle, as is the case here.

3.6.2 Probe size dependence

The slowest velocity observed relates to the position of the center of mass of the tracer from the fixed wall (lower plate). Changing the probe size therefore should lead to changes in ω (slowest velocity) without affecting Γ (near-wall shear rate). This is confirmed in Fig. 3.15 for measurements using GNP of hydrodynamic radius Rh=17 nm and PS latex sphere of Rh=110 nm dispersed in the same Newtonian reference medium. In the Fig. 3.15a we can see the slope of the FFT on the GNP loaded sample is similar to the one of the PS loaded sample while the cut-off for the GNP occurs at a smaller L_ω in a ratio comparable to the particle size ratio.

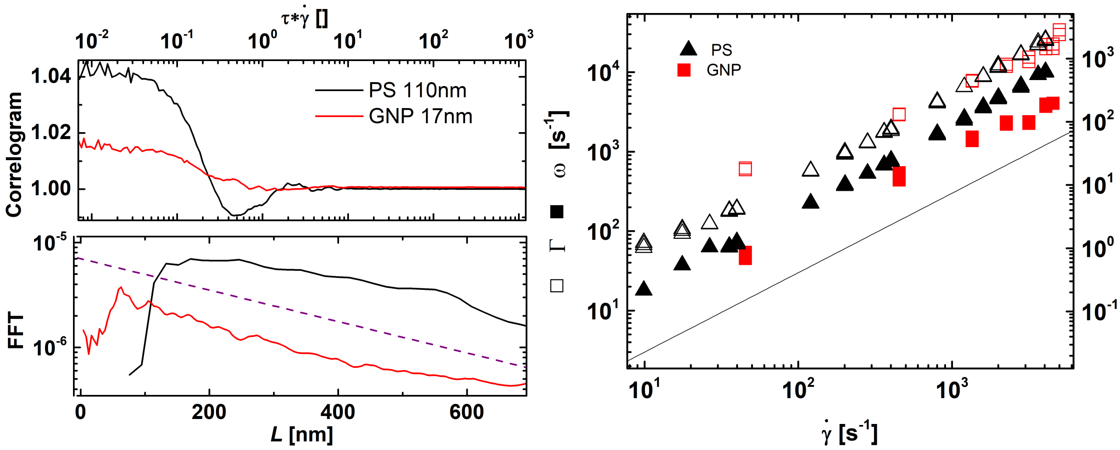

(a) (b)

Figure 3.15: Effect of tracer size. (a) (up) Correlograms normalized to ease comparison; (down) corresponding FFT's. The purple dashed line corresponds to the slope, $1/dp$, which is shared by both data. (b) Γ and ω as obtained by fitting the analytical solution at different shear rates on the two compared cases. The right y-axis shows the values in units of absolute velocity. The slanted has a slope of 1, is just a reference for the eye. Shear rates (s^{-1}): 1354 (GNP), 1200 (PS). Both measured on the Newtonian reference.

3.6.3 Velocity projection over the scattering vector

It should be noted that the technique is sensitive to the velocity projected over the scattering wave vector ($\boldsymbol{v} \cdot \boldsymbol{q}$) and not only to its magnitude. This means that by changing the alignment of the flow relative to $\boldsymbol{q}$, will affect the measured correlation and especially the magnitude of ω and Γ will change. This dependence was experimentally confirmed. Given the specific flow geometry, $\boldsymbol{q}_{||} \cdot \boldsymbol{v}$ depended on the position of the detection area. The sensitivity to the projection is illustrated in Fig. 3.16 where we aligned the EW in order to set $\boldsymbol{q}_{||}$ perpendicular to $\boldsymbol{v}$ and minimize the projection (see inset); as opposed to a standard measurement where $\boldsymbol{q}_{||}$ and $\boldsymbol{v}$ are parallel to maximizes the projection. When the laser beam is aligned to be normal to the tangent of the rheometric flow so that $\boldsymbol{q}_{||} \cdot \boldsymbol{v} \sim 0$ the correlogram decay is found to be ~80 times slower ($\arccos(1/80) \sim 89^\circ$). In practice, nulling this product is a difficult task considering the imperfections in the setup and the alignment. The slowdown hence further demonstrated the validity of the analysis (and of the origin of the signal).

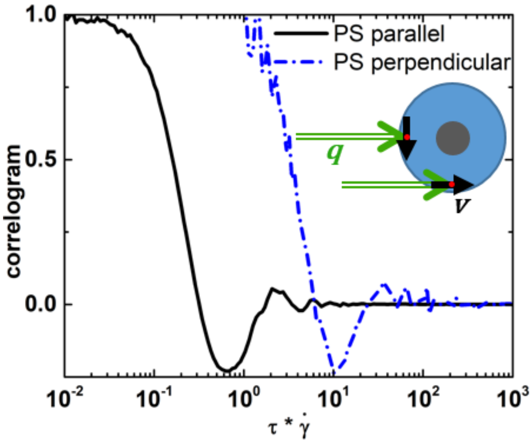

Figure 3.16: (Inset) Schematic of the approach taken to set $\boldsymbol{q}_{||} \cdot \boldsymbol{v} = 0$. The black full arrows correspond to $\boldsymbol{v}$ and the green double line arrows to $\boldsymbol{q}$. (Black full line) Normal working conditions of $\boldsymbol{v}||\boldsymbol{q}$ using 110 nm tracer particles. (Blue dot-dashed line) Correlogram of attempt to nullify the the projection of $\boldsymbol{v}$ over $\boldsymbol{q}$. Same tracer particles as on the black curve. Both correlograms were taken using the same Newtonian reference sample.

3.6.4 Boundary conditions / slip velocity for the Newtonian fluid case

Overall, the values observed are in agreement with no-slip boundary conditions. This was verified by obtaining $L_\omega \sim Rh$ for two distinct tracer particle sizes and $L_\Gamma \sim dp$ (110 nm PS spheres and 17 nm GNP). In addition, we found Γ and ω to depend on the nominal shear rate (Figs. 3.14 and 3.15) as expected from Eq. 3.3.

The current resolution does not allow to clearly resolve the coupled effect of hydrodynamics and concentration profile which would require characterization of particle-surface interactions and is beyond the scope of this manuscript. The penetration depth dp and the particle size R set the resolution of the technique. With the proper choice of R and dp, access to slip lengths as low as a fraction of R (down to 10 nm) should be accessible, which is comparable to TIRF methods [21]. It would however require better control of the experimental conditions.

3.7 Application to complex fluids

The knowledge and understanding of the near wall velocity profile is pertinent in a very broad range of systems [34, 7]. In the following we demonstrate the ability of the technique to report the velocity for strongly slipping systems like dense colloidal suspensions and emulsions, as well as for "weak-slip" situation encountered in polymer solutions.

3.7.1 Colloidal suspensions

Soft pastes and concentrated colloidal suspensions are well known to be prone to slip [35, 36, 37, 38], especially at low shear stress. The interplay between slip and yielding often proves challenging to discern when determining the value of yield stress and the actual rheometric response. We report the measured near wall velocity in a model inorganic clay gel, in a dense microgel suspension and two dense emulsions.

Nanoclay suspension

The nanoclay particles are ∼30 nm in diameter and ∼1 nm thick discs, with negatively charged faces and positively charged rim. The nanoclay suspension sample was prepared as follows. The clay powder was mixed with MilliQ water to a concentration of 2.5%w and then stirred for 2 hours. It was then filtered with a 45 μm pore filter. Finally, three months of rest were given as aging. Before the experiment, PS spheres of 110 nm Rh were introduced as tracer particles. The dp used on this experiment was 66 nm ($n = 1.33,\ \theta_i \sim 76°$).

Flow curve measurement showed a strong shear thinning of $\eta \sim \dot{\gamma}^{-1}$, equivalent to an almost constant stress for the different shear rates; see Fig. 3.18a (red circles).

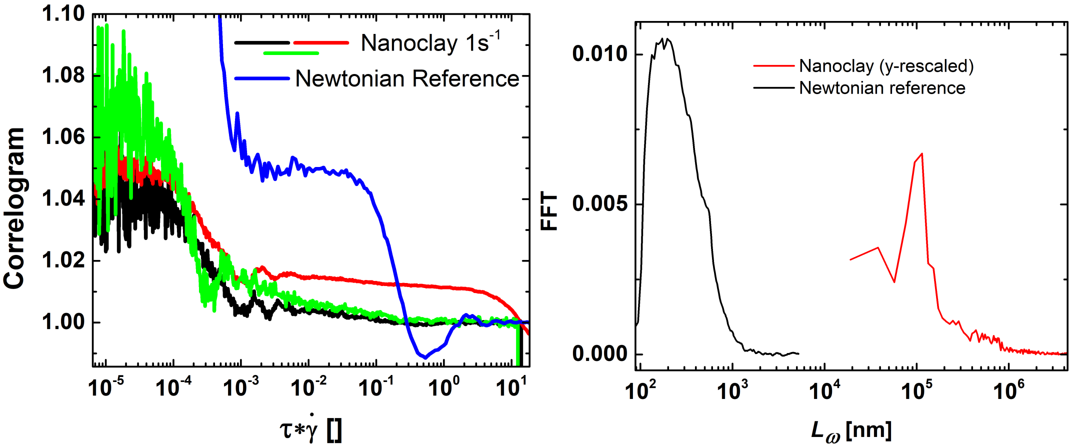

(a) (b)

Figure 3.17: Nanoclay particle 2.5%w physical gel aged for three months. (a) The time axis has been rescaled by the nominal shear rate to compare with the Newtonian reference. We put in evidence here how the nanoclay sample history dependence was observed on the near wall velocity; the three nanoclay data signals were all measured at the same nominal shear rate but had a different shear history. Shear rates (s^{-1}): 1 (nanoclay), 39.88 (Newtonian reference).(b) FFT of a nanoclay correlogram at 1 s^{-1} showing strong slip. The peak is located at 10^5 nm, of the same magnitude as the nominal gap (800 μm). For comparison the Newtonian reference is plotted, its cut-off is located at ∼110 nm, the tracers' radius.

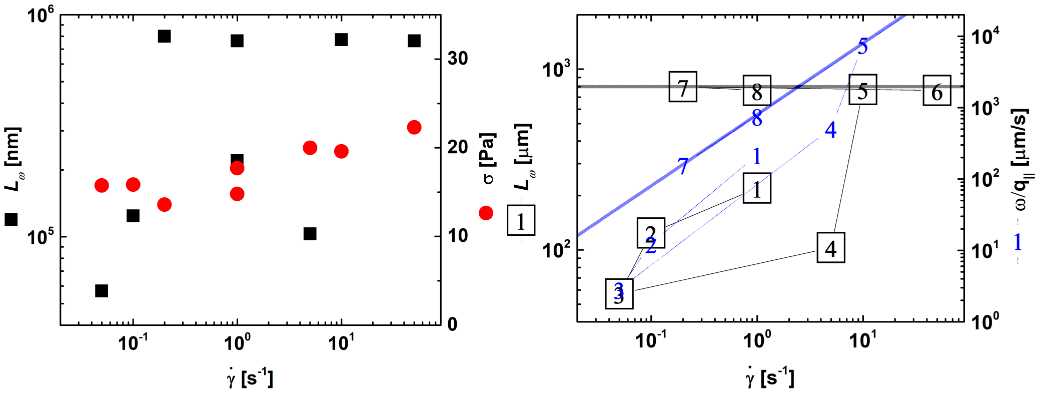

(a) (b)

Figure 3.18: Nanoclay particle 2.5%w physical gel aged for three months. (a) L_ω on the left axis and almost constant non-linear stress recorded by the rheometer on the right axis. (b) L_ω (left axis) and near wall velocities (right axis) with indexes indicating the chronological order of the measurements. The grey horizontal line is the nominal gap (800 μm) and the blue slanted line is the nominal velocity of the top plate.

It is worth noting that the measurements were done under rate control mode. We applied EWDLS velocimetry to monitor the near wall velocity at constant shear rates and quantified the presence of slip.

Measured correlograms are shown in Fig. 3.17a where the time axis has been rescaled by the nominal shear rate to bring emphasis the relative difference in the near wall velocities. Correlograms of the Newtonian reference, corresponding to stick boundary conditions, have been added for comparison. The rescaled velocities of the near wall tracers were 1000 times faster than they were in the Newtonian reference. The apparent slip length L_ω were obtained from the analysis of the $C(f)$ that are shown in Fig. 3.17b. They are reported in Fig. 3.18a as a function of the apparent shear rate, together with the applied stress. The apparent slip lengths values are very large, of the order of the gap (800 μm), revealing that the measured particle velocity was of the order of the top plate velocity. That can be achieved by the sample moving in a plug flow at the speed of the top plate.

The slip lengths obtained were found to vary with shear rate, a sign of possible flow instabilities, shear history dependence or flow hysteresis [39, 17]. This can be seen from Fig. 3.17a which shows three different measurements under the same nominal shear rate (at different time in the series of experiments) that show distinct near wall velocities. The points in Fig. 3.18a have non monotonic evolution, indicating instability in the sample. Interestingly the evolution of the slip length appears to be correlated with the sample history. Following the black boxed numbers in Fig. 3.18b, there is an apparent hysteresis in L_ω indicating the importance of shear history on the slip for the specific sample.

Very strong slip, as the one reported here has consequences on the measured rheology as the actual shear rate in the gap is very different from the nominal shear rate.

The correlograms in Fig. 3.17a show a strongly damped oscillation. This damping has to be the result of velocity distributions, either spatial or temporal. A distribution of v along z for example would produce a microscopic shear rate incompatible with the large slip velocities measured. The observed damping was most likely the effect of velocity field variations during the measurement. Further experiments would be needed to distinguish between spatial and temporal effects.

Microgel suspension

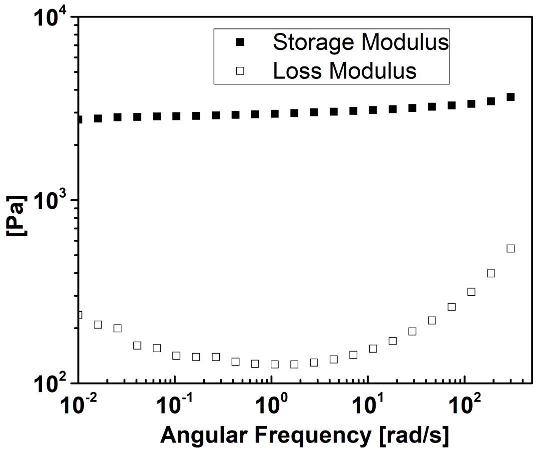

Figure 3.19: Linear rheology for the 50 mg/g fully ionized microgel suspension in water (a paste), dilute Rh = 305 nm. No added tracers. Credit to Leo Gury for this data.

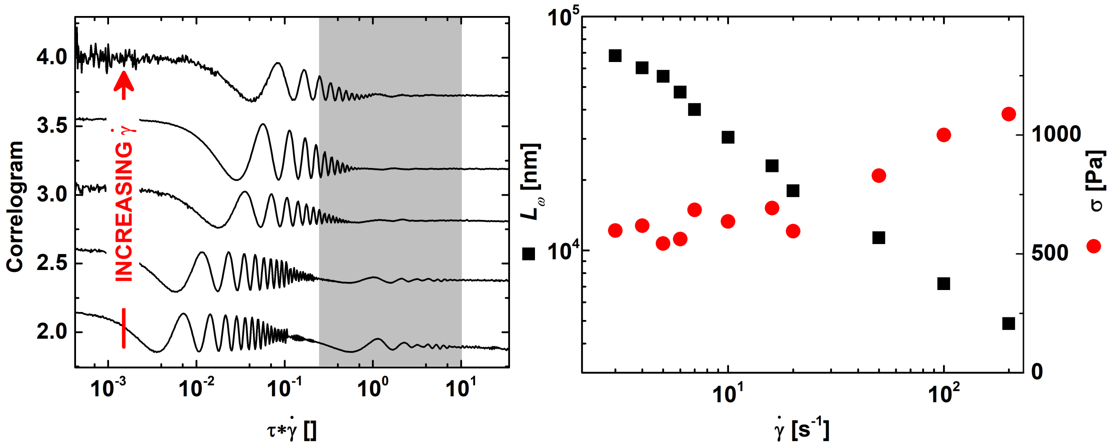

(a) (b)

Figure 3.20: 50 mg/g fully ionized microgel suspension in water (a paste), dilute Rh = 305 nm. No added tracers. (a) Selected correlation functions. The time axis was rescaled by the shear rate. The curves are translated vertically with increasing shear rate to visualize the different near wall velocity trend. The grey area contains a slow stick mode ($L_\omega \sim 350\ nm \sim Rh$). (b) L_ω and non-linear shear stress σ as a function of the nominal shear rate.

We further tested slip detection in a microgel suspension. The rheology of microgels in dense phases and the possible presence of slip has been studied with great detail [40, 41, 42, 38]. For this system we did not add tracer particles as the microgel themselves provided large enough scattering intensities. The velocities of the colloidal microgels were directly probed.

The microgels used were fully ionized and have a hydrodynamic radius Rh of 305 nm when in dilute conditions. The concentration was 50 mg/g in water and is expected to be in the jammed suspension regime [43]. The sample formed an elastic suspension with G'$\sim$3 kPa as seen from linear rheology in Fig. 3.19. We report measuring near-wall velocimetry while establishing a bulk flow curve, using smooth glass plates making no effort to prevent slip. Rheological measurement of these type of systems are usually done on rough plates to prevent slip. The nominal dp used here was 72 nm ($n = 1.33$, $\theta_i \sim 73°$). The EWDLS measurements were done during steady state shear, at a fixed shear rate (strain-controlled mode).

The flow curve was generated simultaneously with near-wall velocimetry data as shown in Fig. 3.20b. It shows a weak dependence of the shear stress to the shear rate, as expected for these microgels [43]. A change of slope around $\dot{\gamma}$=10 s^{-1} was clearly noticeable, which is usually attributed to the onset of slip.

Fig. 3.20a shows a set of measured correlograms at different shear rates (times axis rescaled by the nominal shear rate and vertically translated for clarity) for the high concentration suspension. Noticeably, the correlation functions show periodic oscillation that are only slowly decaying. Moreover the small damping does not relate to probed velocities as it is most likely due to the aliasing present in multitau-correlators. The undamped oscillation is a sign of a single probed velocity (or narrow velocity distribution). Undamped correlogram can be expected from Eq. 3.3 when $\omega \gg \Gamma$, corresponding to low shear rate as in the case of high slips and plug flow. Experimentally we expect Γ to not be measurable when $\omega \gg 20\Gamma$. The single velocity v_0 or equivalently $L_\omega = v_0/\dot{\gamma}$ can easily be extracted from the peak of $C(f)$. The obtained values for L_ω were large, decreasing with increasing shear rate from 60 to 4 μm. Note that near-wall slip in these type of systems is known to depend on the physical conditions of the surface (roughness, chemistry, ...) [42].

Large slip velocities (or slip lengths) were observed at low shear rates, indicative of slip and plug flow prior to yielding. On increasing the shear rate, the slip length was observed to decrease. Even at the highest shear rate, slip lengths remained rather large at $L_\omega = 10\ \mu m$ in comparison to stick boundary conditions ($0.3\ \mu m$) found for the Newtonian system. The results are in good agreement with macroscopic velocimetry [44]. In this regime, we found velocities (or L_ω) to be independent of the gap for the same apparent shear rate. We infer that slip was mostly present on the bottom plate.

A weaker, slower mode was found for the microgel suspensions. This is contained within the grey area in Fig. 3.20a The corresponding L_ω is of the order of the particle radius that would correspond to stick conditions. The amplitude of the slower mode was found to decrease with increasing shear rate. The slower mode may have originated from stick conditions at low shear prior to the fracturing of flow. Unlike the fast velocity, the slow velocity scaled with the nominal shear rate. The mode was more visible on the lower shear rates with decreasing amplitude as the shear rate was increased. The ratio of the two velocities was therefore shear rate dependent. This stick-like velocity could be a signature of stick-slip behavior as we may expect it to happen predominantly at lower shear rates.

Concentrated emulsions

Here we present the finding of slip for two emulsions. One oil rich (85%w) in water emulsion with RI 1.4, $\theta_i = 72.8°$, $dp = 220$ nm and gap $= 400\ \mu m$; and one water rich (78%w) in oil emulsion with RI 1.425 $\theta_i = 72.8°$, $dp = 300$ nm and gap $= 600\ \mu m$. Both emulsions were carefully produced by Zhang et al. to be indexed matched to limit their scattering for optical studies. Both emulsions are therefore optically dilute but provide enough contrast to be studied without added tracers in the single scattering regime. In spite of this, we show in chapter 4 that we are able to obtain the velocimetric information even in the case of optically concentrated materials.

As seen in Fig. 3.21b, both emulsions were weak solids. Fig. 3.21a shows L_ω normalized by the corresponding gap size. The near wall velocities were comparable to the top plate velocities ($L_\omega/gap \sim 1$) at low shear rates, implying full slip. Corre-

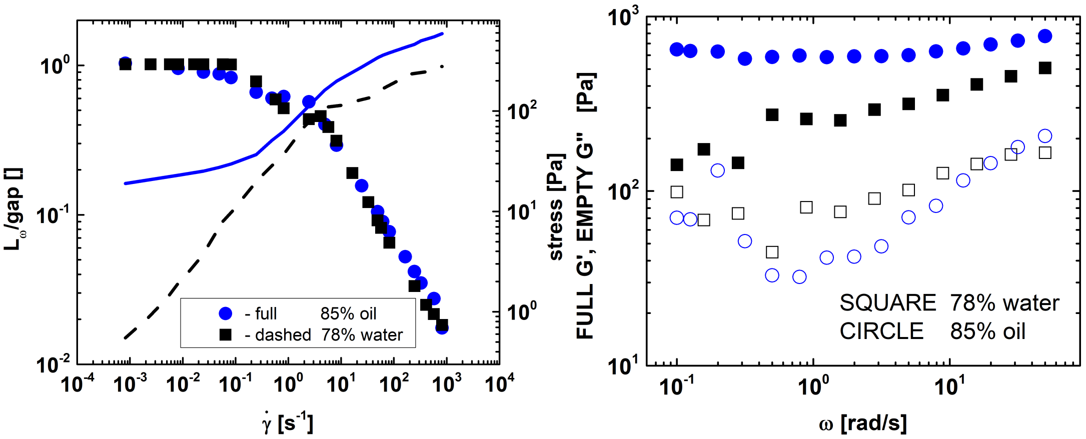

(a) (b)

Figure 3.21: Water and oil emulsions. (a) L_ω normalized by gap length (symbols) and shear stress (lines) vs nominal shear rate. (b) Linear frequency sweeps.

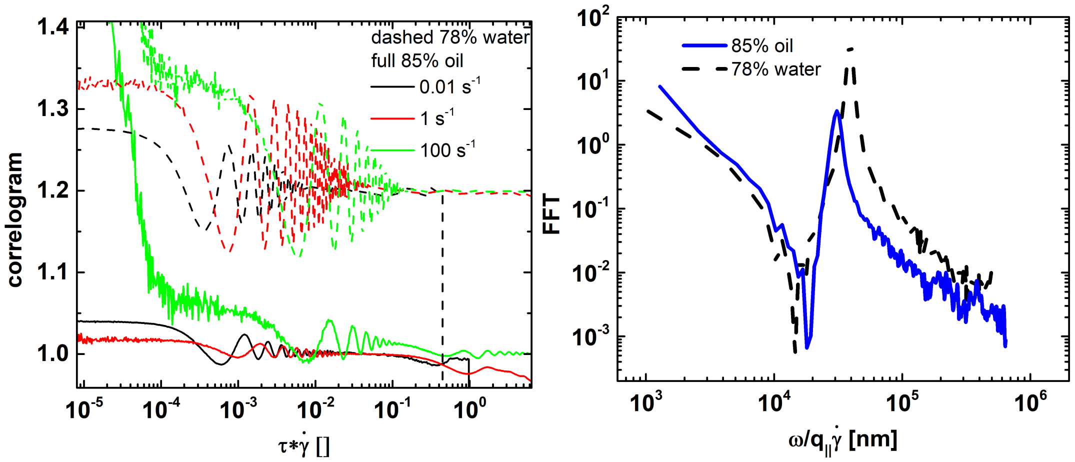

(a) (b)

Figure 3.22: Water and oil emulsions. (a)Intensity correlograms with rescaled x-axis. The water rich (dashed lines) correlograms were vertically shifted for clarity. (b) FFT's of the correlograms at 100 s^{-1}.

spondingly, the correlograms in Fig. 3.22a show strong persistent oscillations. As the shear rate was increased L_ω decreased systematically, going through one short plateau at $\dot{\gamma}_{nominal} \sim 1\ s^{-1}$ and there on rapidly falling. In a manner similar to L_ω, the shear stress increased systematically from low to high shear rates. The bulk yield stress encountered in Herschel-Bulkley fluids was masked by the presence of strong slip at the low shear rates.

Zhang et al. [38], who used a roughened top plate and a smooth lower plate, reported similar slip to be common on a series of soft jammed systems of different nature (including a similar emulsion) suggesting the origin of slip to be given in first order by the jamming structure filled with a mobile interstitial liquid. Differently, we observed a two step process in the near wall velocities and in the shear stress. This might be a consequence of using two smooth plates.

The technique is suitable for tracer-free measurements of colloidal gels. Measurements are straightforward and can be recorded in less than 10 seconds. The scattering from the microgel suspension was appreciably strong. This tracer-free capability provides a clear advantage over other velocimetric approaches and can be applied to multiphase systems. The only criteria is the necessity of having appreciable scattering intensity. EWDLS revealed a single near wall velocity of the microgel suspension; nonetheless, the onset of local shear rate (meaning actual deformation within the material) cannot be resolved when $\omega \gg \Gamma$.

3.7.2 Polymer solutions: weak slips

The case of polymer slip has received a considerable amount of attention maybe more so in melt than in solutions [45, 46, 10, 47, 48, 49]. Slip in polymer solutions is somewhat more complicated than in melts as coupling between concentration and stress provides possibilities of additional deformation mechanisms [34, 50]. We here present results on polymer solutions.

We used solutions in ethylene glycol of PVP360 (Aldrich) and 450 kD PAA (Aldrich) with 10% weight concentration. The solutions were loaded with PS latex tracers (Rh = 110 nm). Nominal dp were respectively 94 nm and 130 nm (n=1.439 and 1.425, $\theta_i \sim 82^\circ$ and 74°). The dynamic viscosities of the two solutions are given respectively in Figs. 3.23b and 3.25b showing weak shear thinning.

For the analysis, we used the FFT of the correlograms shown rescaled with the shear rate in Figs. 3.24b and 3.26b. Typical correlograms acquired at steady flow at fixed shear rates are shown in Figs. 3.24a and 3.26a covering a range of shear rates between 10 and 10^3 s^{-1}.

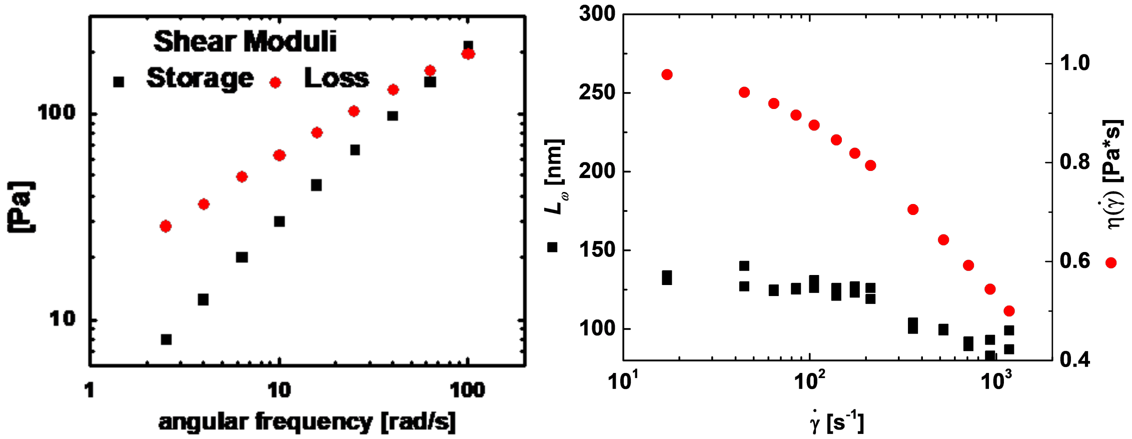

(a) (b)

Figure 3.23: PVP360 10% w in ethylene glycol: (a) Linear rheology. (b) L_ω and viscosity as a function of the nominal shear rate.

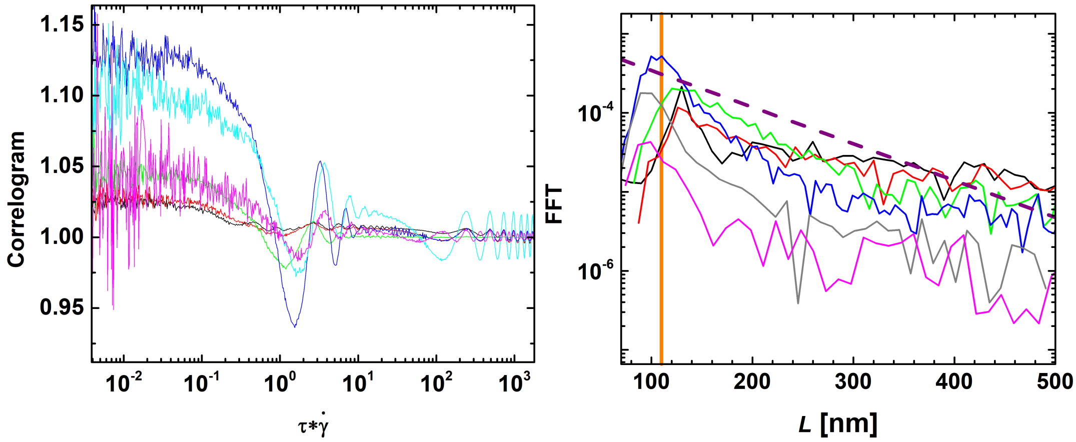

(a) (b)

Figure 3.24: PVP360 10% w in ethylene glycol: (a) Correlograms with time axis rescaled to length. Shear rates (s^{-1}): 64, 106, 175, 358, 711, 1176 (b) FFT's with frequency axis rescaled to length. Shear rates (s^{-1}): -64, -106, -175, -358, -711, -1176

In the case of PVP solution, the FFT were close to the expected shape of the FFT of Eq. 3.3. The obtained values of the low velocity cut-off were almost independent of shear rate up to 200 s^{-1} at L_ω ~125 nm (Fig. 3.23b). This value is slightly larger but close to the value measured in the Newtonian reference (110 nm) and reflects weak slip boundary conditions. At higher shear rates, the value of L_ω went down by ~20% (from 125 to 80 nm) with increasing shear rate.

For the origin of the lower slip length at higher shear rate, several possibilities can be mentioned: instability in the rate control by the rheometer at high shear rate (measured on the Rheometrics DSR) or a wrong estimation of the shear rate. A downward migration of the tracer and the accompanying slow-down of their velocity as they get closer to the immobile plate would also lead to such a decrease; however, such an effect is not really expected [27, 50]. Tracers getting closer to the wall should lead to an increase of the scattered intensity and tracers getting away from the wall should lead to a decrease of the intensity [51]. However precise intensity measurements are difficult to achieve in heterodyne conditions. We are not able to answer this matter with certainty.

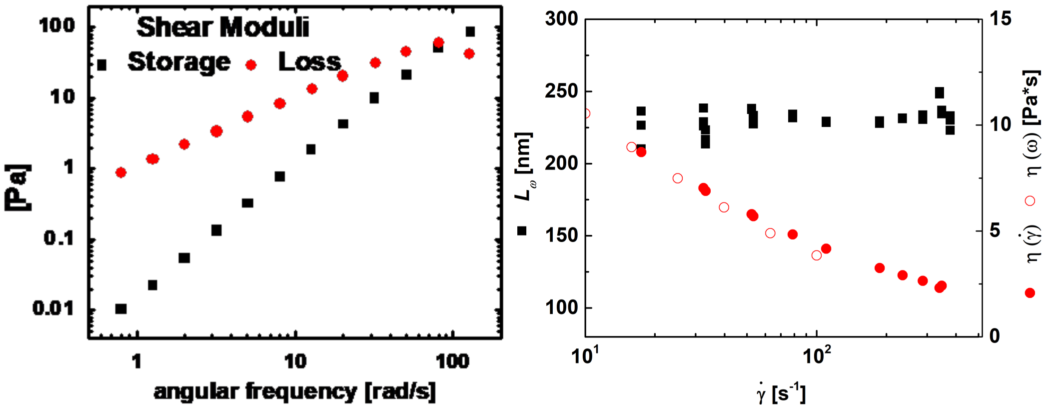

(a) (b)

Figure 3.25: PAA 10% w in ethylene glycol: () Linear rheology. (B) L_ω and viscosity as a function of the nominal shear rate.

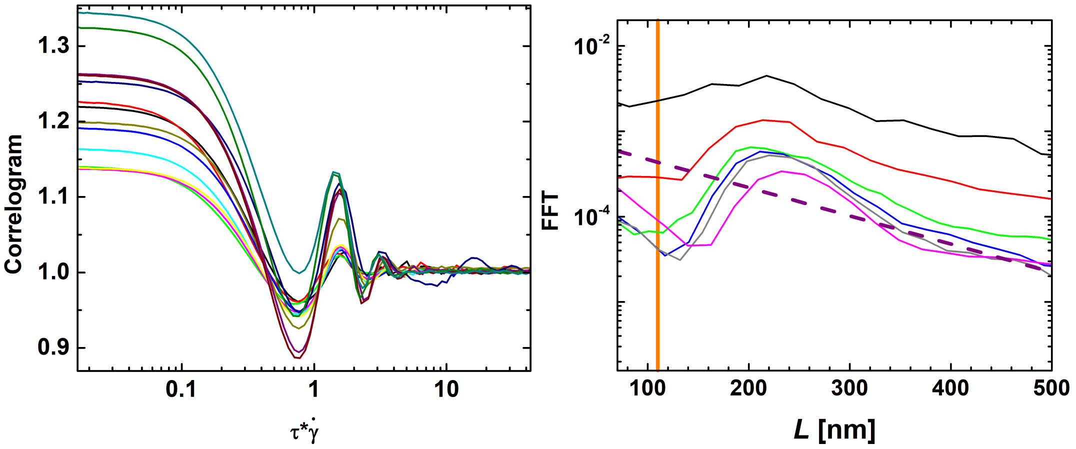

(a) (b)

Figure 3.26: PAA 10% w in ethylene glycol: (a) Correlograms with time axis rescaled to length. Shear rates (s^{-1}):17, 53, 110, 187, 288, 378. (b) FFT's with frequency axis rescaled to length.

In the case of PAA solutions, the correlograms showed a different shape (Fig. 3.26a), especially visible in the Fourier transform $C(f)$ where a low frequency peak was observed instead of a cut-off. This peak was found to scale with the macroscopic shear rate and the associated apparent slip length L_ω ~230 nm. L_ω was found to be almost constant over a broad range of shear rate. This value was larger than in the Newtonian reference and in the PVP solutions. Such value corresponds to a “weak” slip case with a “true” slip length, $L_\omega - R$ ~100 nm (Fig. 3.23b). This value is large for molecular slip ($> Rg$ of chains), but reasonable for hydrodynamic slip.

Both solutions showed what we can characterize as non-slip to weak slip. These small slip lengths are not expected to have significant impact on the overall velocity profile and on the rheology measurements.

The small but established difference between the two solutions could originate from different interaction between the polymer and the surface and/or between the polymer and the tracer [34, 50]. As illustrated in 3.4.3 (Fig 3.7 and 3.8), a change of $c(z)$ would lead to change of shape of $C(f)$. The tracer particles in the PAA measurements would need to be depleted from the wall as a result of a repulsive interaction for example. A weak wall-tracer attraction would rationalize the PVP solutions findings. The slip length in polymer solution could be expected to be set by the size of the polymer chain, i.e order of $Rg \sim$ nm, or by the blob size $\xi < Rg$ [28, 52]. This small slip length is in qualitative agreement with our measurements.

Noticeably, the correlogram measured in polymer solutions were noisier when compared to the Newtonian reference. This posed the question of dispersion of the probes which may not always be easily attainable in polymer solutions. Similar requirements apply to most tracer velocimetry techniques. To further extract conclusions for polymer solutions would require better control of the experimental conditions [52] and lies beyond the scope of this manuscript.

3.8 Conclusions

We have presented a practical approach to incorporate EWDLS in a bulk rheometric apparatus. The evanescent wave at TIR provides interfacial sensitivity, as the probed volume extends within the first micrometer or so from the bottom plate. The technique provides a good way to detect slip and quantify near plate velocity in rheology experiments. We introduced a spectrum analysis through Fourier transform of the correlation function to allow the direct determination of two local quantities; the near wall velocity and the local near wall shear rate (velocity gradient).

A proper interpretation of the data in terms of velocity profile $v(z)$ requires the pre-knowledge of the tracer concentration profile $c(z)$ in the penetration depth, which with the present implementation cannot be measured by the technique. However, we were able through the use of simulation to confirm that the simplified analysis is rather robust and returns correct values of velocities in case of realistic non uniform $c(z)$.

The scattering-based technique measures the velocity of scatterers, being either added probes or inherent to the sample (if the scattering is sufficiently strong). Proper choice of probes with good dispersion and predictable $c(z)$ is therefore essential. The good dispersion should be checked, for example by bulk scattering. The requirements of good dispersion and distribution of probes are generic to most probe velocimetry techniques, but they are specifically important in the present case as the measured velocities depend on the size and position of the probes (which as mentioned above are not easy to crosscheck with the technique). Individual "bad probes" cannot be eliminated from the analysis, unlike in most imaging techniques where individual probes are analyzed separately and the probe-wall distance can be estimated.

EWDLS analysis relies on single scattering, therefore scattering has to be large enough to provide good statistics and short measurement time. It is worth noting that due to the reduced scattering volume, the single scattering condition is less stringent than in bulk scattering experiments. The single scattering condition also guaranties that the simple Fresnel interface evanescent field assumption are met.

EWDLS requires the ability to reach TIR conditions, that is high enough refractive index of the plate, $n_{plate} > n_{sample}$. Measurements of high refractive index sample (like some polymer melts) will require the use of special high n plate. In the case of water based systems standard BK7 glass plate can be used (as shown in this study).

Thanks to the use of multiple-tau correlator, the accessible range of velocities (see Fig. 3.12) covers up to 5 decades from 10^{-1} to 10^{4} $\mu m s^{-1}$ and therefore the technique is suited for a broad range of shear rates. The full range of slip length (from very small in stick boundary condition to the gap in case of strong slip) can be detected in that very broad range of shear rate. We have established the no-slip boundary condition for the Newtonian fluids with $L_{\omega} \sim Rh$ and $L_{\Gamma} \sim dp$. Weak slip was observed in polymer solutions. The presence of strong slip was established in the case of yielding colloidal dispersions. Noticeably, microgel suspensions were measured without the use of added tracers.

All measurements were done in the ballistic regime (Pe$\gg$1), i.e. when the diffusion term can be neglected. It is possible to do measurements at lower Peclet number, but the measured correlation functions will have a contribution from diffusion as well as flow and their analysis will be more complicated.

Other (mostly) optical techniques have been applied to measure near wall velocimetry. Compared to them, EWDLS presents several advantages and disadvantages. Its implementation is relatively simple as the detection does not need to be very close to the probed samples (unlike microscopy). It is a probe based technique but does not require fluorescent tracers compared to particle tracking based velocimetry that measures the individual velocities of probes. We established a simple real time analysis for EWDLS velocimetry that directly provides velocities averaged on a large number of probes. Moreover the multi-tau correlator provides a very broad range of measurable velocities. The technique has several limitations (not necessarily present in the other techniques), mostly originating in the averaging nature of DLS, like the difficulty to assert the tracer distribution and possible heterogeneities within the flow.

To conclude, EWDLS has been integrated into commercial stress-controlled rheometers. This hybrid rheo-optic measurement apparatus is able to resolve near-wall (sub-micron penetration depth from the bottom plate) velocity profiles during bulk flow measurements on a variety of materials over a broad range of time scales and shear rates. The technique is robust in its measurement capacity and can be applied tracer-free to colloidal suspensions.

3.9 Acknowledgements

We thank the following people for their contributions. M. Cloitre, for providing us with the microgel sample and useful comments and critical reading of the manuscript. L. Gury for the microgel suspension preparation and many useful discussions. Malvern for the Malvern Kinexus. R. Kumar for his help on the sample preparation of the nanoclay dispersion. J. Ramirez for the correlator used for the simulations in the simulations. D. Vlassopoulos and G. Petekidis for useful discussions.

This chapter was adapted from the published paper [53] that was a joint effort with R. McKenzie.

Bibliography

[1] M. Mooney, “Explicit Formulas for Slip and Fluidity,” *Journal of Rheology*, vol. 2, no. 2, pp. 210–222, 1931.

[2] D. Mehta and M. C. Hawley, “Wall effect in packed columns,” *Industrial and Engineering Chemistry Process Design and Development*, vol. 8, no. 2, pp. 280–282, 1969.

[3] S. G. Hatzikiriakos and J. M. Dealy, “Wall slip of molten high density polyethylene. I. Sliding plate rheometer studies,” *Journal of Rheology*, vol. 35, no. 4, pp. 497–523, 1991.

[4] H. Shuzui, “Process of slip-surface development and formation of slip-surface clay in landslides in Tertiary volcanic rocks, Japan,” *Engineering Geology*, vol. 61, no. 4, pp. 199–219, 2001.

[5] B. Elhweg, I. W. Burns, Y. M. J. Chew, P. J. Martin, A. B. Russell, and D. I. Wilson, “Viscous dissipation and apparent wall slip in capillary rheometry of ice cream,” *Food and bioproducts procressing*, vol. 87, pp. 266–272, dec 2009.

[6] R. G. Larson, *The Structure and Rheology of Complex Fluids*, vol. 150. New York Oxford, 1999.

[7] M. Cloitre and R. T. Bonnecaze, “A review on wall slip in high solid dispersions,” *Rheologica Acta*, vol. 56, pp. 283–305, mar 2017.

[8] H. A. Barnes, “A review of the slip (wall depletion) of polymer solutions, emulsions and particle suspensions in viscometers: its cause, character, and cure,” 1995.

[9] D. W. Lee, X. Banquy, and J. N. Israelachvili, “Stick-slip friction and wear of articular joints,” *Proceedings of the national academy of sciences of the United States of America*, vol. 110, pp. E567–E574, feb 2013.

[10] S. G. Hatzikiriakos, “Wall slip of molten polymers,” *Progress in Polymer Science*, vol. 37, no. 4, pp. 624–643, 2012.

[11] G. A. Abers, P. E. van Keken, and B. R. Hacker, “The cold and relatively dry nature of mantle forearcs in subduction zones,” *Nature Geoscience*, vol. 10, pp. 333–337, may 2017.

[12] R. Buscall, “Letter to the Editor: Wall slip in dispersion rheometry,” *Journal of Rheology*, vol. 54, no. 6, pp. 1177–1183, 2010.

[13] G. Vleminckx and C. Clasen, “On the inseparability of slip and gap-error,” *Journal of Rheology*, vol. 60, pp. 549–557, jul 2016.

[14] E. Manias, G. Hadziioannou, I. Bitsanis, and G. T. Brinke, “Stick and slip behaviour of confined oligomer melts under shear. A molecular-dynamics study,” *EPL*, vol. 24, no. 2, pp. 99–104, 1993.

[15] D. J. Lee, K. Y. Cho, S. Jang, Y. S. Song, and J. R. Youn, “Liquid slip on a nanostructured surface,” *Langmuir*, vol. 28, no. 28, pp. 10488–10494, 2012.

[16] A. L. Vayssade, C. Lee, E. Terriac, F. Monti, M. Cloitre, and P. Tabeling, “Dynamical role of slip heterogeneities in confined flows,” *Physical Review E - Statistical, Nonlinear, and Soft Matter Physics*, vol. 89, no. 5, 2014.

[17] P. Ballesta, G. Petekidis, L. Isa, W. C. K. Poon, and R. Besseling, “Wall slip and flow of concentrated hard-sphere colloidal suspensions,” *Journal of Rheology*, vol. 56, pp. 1005–1037, sep 2012.

[18] P. Ballesta, N. Koumakis, R. Besseling, W. C. K. Poon, and G. Petekidis, “Slip of gels in colloid-polymer mixtures under shear,” *Soft Matter*, vol. 9, no. 12, p. 3237, 2013.

[19] S. Jin, P. Huang, J. Park, J. Y. Yoo, and K. S. Breuer, “Near-surface velocimetry using evanescent wave illumination,” *Experiments in Fluids*, vol. 37, no. 6, pp. 825–833, 2004.

[20] C. Zettner and M. Yoda, "Particle velocity field measurements in a near-wall flow using evanescent wave illumination," *Experiments in Fluids*, vol. 34, pp. 115–121, jan 2003.

[21] Z. Li, L. Déramo, C. Lee, F. Monti, M. Yonger, P. Tabeling, B. Chollet, B. Bresson, and Y. Tran, "Near-wall nanovelocimetry based on total internal reflection fluorescence with continuous tracking," *Journal of fluid mechanics*, vol. 766, pp. 147–171, mar 2015.

[22] B. Loppinet, J. K. G. Dhont, and P. Lang, "Near-field laser Doppler velocimetry measures near-wall velocities," *European Physcal Journal E*, vol. 35, jul 2012.

[23] R. Pecora, *Dynamic Light Scattering: Applications of Photon Correlation Spectroscopy.* Plenum Press, New York and London, 1985.

[24] P. Holmqvist, J. K. G. Dhont, and P. R. Lang, "Colloidal dynamics near a wall studied by evanescent wave light scattering: Experimental and theoretical improvements and methodological limitations," *The Journal of Chemical Physics*, vol. 126, p. 44707, jan 2007.

[25] Y. Kazoe, K. Mawatari, and T. Kitamori, "Behavior of Nanoparticles in Extended Nanospace Measured by Evanescent Wave-Based Particle Velocimetry," *ANALYTICAL CHEMISTRY*, vol. 87, no. 8, pp. 4087–4091, 2015.

[26] R. Sigel, "Light scattering near and from interfaces using evanescent wave and ellipsometric light scattering," *Current Opinion in Colloid & Interface Science*, vol. 14, pp. 426–437, dec 2009.

[27] A. Goldman, R. Cox, and H. Brenner, "Slow viscous motion of a sphere parallel to a plane wall- Motion through a quiescent fluid," *Chemical Engineering Science*, vol. 22, no. 4, pp. 637–651, 1967.

[28] P. G. de Gennes, "On Fluid/Wall Slippage," *Langmuir*, vol. 18, no. 9, pp. 3413–3414, 2002.

[29] W. Wang, J. S. Guasto, and P. Huang, "Measurement bias in evanescent wave nano-velocimetry due to tracer size variations," *Experiments in Fluids*, vol. 51, pp. 1685–1694, dec 2011.

[30] Y. Takeda, "Velocity profile measurement by ultrasonic doppler method," *Experimental Thermal and Fluid Science*, vol. 10, no. 4, pp. 444–453, 1995.

[31] M. A. Potenza, M. D. Alaimo, D. Pescini, D. Magatti, F. Ferri, and M. Giglio, "A new technique for fluid velocimetry based on near field scattering," *Optics and Lasers in Engineering*, vol. 44, no. 7, pp. 722–731, 2006.

[32] J. Ramírez, S. K. Sukumaran, B. Vorselaars, and A. E. Likhtman, "Efficient on the fly calculation of time correlation functions in computer simulations," *The Journal of Chemical Physics*, vol. 133, p. 154103, oct 2010.

[33] W. Kester, *Mixed-signal and DSP Design Techniques.* Elsevier, 2003.

[34] C. L. Berli, “The apparent hydrodynamic slip of polymer solutions and its implications in electrokinetics,” *Electrophoresis*, vol. 34, pp. 622–630, mar 2013.

[35] R. Buscall, “The rheology of concentrated dispersions of weakly attracting colloidal particles with and without wall slip,” *Journal of Rheology*, vol. 37, no. 4, p. 621, 1993.

[36] S. P. Meeker, R. T. Bonnecaze, and M. Cloitre, “Slip and flow in soft particle pastes,” *Physical Review Letters*, vol. 92, no. 19, 2004.

[37] P. Panaseti, A.-L. Vayssade, G. C. Georgiou, and M. Cloitre, “Confined viscoplastic flows with heterogeneous wall slip,” *Rheologica Acta*, vol. 56, pp. 539–553, jun 2017.

[38] X. Zhang, E. Lorenceau, P. Basset, T. Bourouina, F. Rouyer, J. Goyon, and P. Coussot, “Wall Slip of Soft-Jammed Systems: A Generic Simple Shear Process,” *Physical Review Letters*, vol. 119, nov 2017.

[39] M. P. Lettinga and S. Manneville, “Competition between Shear Banding and Wall Slip in Wormlike Micelles,” *Physical Review Letters*, vol. 103, p. 248302, dec 2009.

[40] S. P. Meeker, R. T. Bonnecaze, and M. Cloitre, “Slip and flow in pastes of soft particles: Direct observation and rheology,” *Journal of Rheology*, vol. 48, no. 6, pp. 1295–1320, 2004.

[41] M. Philippou, Y. Damianou, X. Miscouridou, and G. C. Georgiou, “Cessation of Newtonian circular and plane Couette flows with wall slip and non-zero slip yield stress,” *Meccanica*, vol. 52, pp. 2081–2099, jul 2017.

[42] H. M. Shewan, J. R. Stokes, and M. Cloitre, “Particle-wall tribology of slippery hydrogel particle suspensions,” *Soft Matter*, vol. 13, no. 10, pp. 2099–2106, 2017.

[43] C. Pellet and M. Cloitre, “The glass and jamming transitions of soft polyelectrolyte microgel suspensions,” *Soft Matter*, vol. 12, pp. 3710–3720, apr 2016.

[44] J. R. Seth, C. Locatelli-Champagne, F. Monti, R. T. Bonnecaze, and M. Cloitre, “How do soft particle glasses yield and flow near solid surfaces?,” *Soft Matter*, vol. 8, no. 1, pp. 140–148, 2012.

[45] L. Léger, H. Hervet, G. Massey, and E. Durliat, “Wall slip in polymer melts,” *Journal of Physics Condensed Matter*, vol. 9, no. 37, pp. 7719–7740, 1997.

[46] W. B. Black and M. D. Graham, “Slip, concentration fluctuations, and flow instability in sheared polymer solutions,” 2001.

[47] A. Cuenca and H. Bodiguel, “Submicron flow of polymer solutions: Slippage reduction due to confinement,” *Physical Review Letters*, vol. 110, no. 10, 2013.

[48] M. Naiim, A. Boualem, C. Ferre, M. Jabloun, A. Jalocha, and P. Ravier, “Multiangle dynamic light scattering for the improvement of multimodal particle size distribution measurements,” *Soft Matter*, vol. 11, pp. 28–32, dec 2015.

[49] M. Ebrahimi, V. K. Konaganti, and S. G. Hatzikiriakos, “Dynamic slip of polydisperse linear polymers using partitioned plate,” *Physics of Fluids*, vol. 30, p. 030601, mar 2018.

[50] A. Nikoubashman, N. A. Mahynski, A. H. Pirayandeh, and A. Z. Panagiotopoulos, “Flow-induced demixing of polymer-colloid mixtures in microfluidic channels,” *Journal of Chemical Physics*, vol. 140, p. 094903, mar 2014.

[51] S. De Sio and P. R. Lang, “Depletion Interaction Mediated by fd-Virus: on the Limit of Low Density and Derjaguin Approximation,” *Zeitschrift für Physikalische Chemie*, vol. 229, pp. 1161–1175, jan 2015.

[52] Sanchez-Reyes, Archer, and L. A., “Interfacial Slip Violations in Polymer Solutions: Role of Microscale Surface Roughness,” *Langmuir*, vol. 19, no. 8, pp. 3304–3312, 2003.

[53] A. Giuliani, R. McKenzie, and B. Loppinet, “Near wall velocimetry on a rheometer,” *Journal of Rheology*, vol. 63, pp. 93–104, jan 2019.

Chapter 4

EW-DLS on turbid media

4.1 Introduction

Evanescent wave dynamic light scattering (EW-DLS) is in principle limited to single scattering, i.e. weak dynamic intensities [1]. This imposes a restriction in terms of concentration of scatterers and solvents to be used (contrast). Consequently the measurements are typically difficult and have poor signal to noise ratio.

Point of entrance detection has been addressed recently [2] to target the limits of the diffusion approximation [3] in the transport of light in turbid media. Due to the very specific geometry used in EW-DLS it is not clear whether multiple scattering needs to be prohibitive. Moreover strong multiple scattering in the bulk is routinely taken advantage of on the diffusive wave spectroscopy (DWS) yet the effect of an EW illumination on similar conditions is not known.

In this chapter we investigate possibility of measuring EW-DLS of samples presenting multiple scattering, up to highly turbid samples. This is done through a combination of experiments and simulation. We found that the single scattering from the EW can still be detected and used for DLS. Moreover a DWS like signal is also detected that adds to the single scattering contribution. In the case of EW-DLS on a rheometer this DWS signal provides bulk information on the flow independently from the near wall single scattering signal.

4.1.1 Effect of multiple scattering on DLS

Higher than first order scattering in dynamic light scattering results in the quantities typically measured in DLS (intensity $I(\theta)$, scattering wave vector q, correlation function $g(t)$ and polarization) to become geometry dependent and not analyzable with the traditional DLS theory. While the DWS limit can be treated as a diffusion problem, the mildly turbid remains problematic.

The relationship between detection angle and length scale being probed ($q = 4\pi\lambda^{-1}\sin(\theta/2)$) is lost. In fact the scattering wave vector is no more the relevant length scale [4]. In the diffusive limit the relevant length scale becomes the transport mean free path l^* [5] defining the smallest step in a random walk of the light.

$$l^* = l\frac{2k_0^2}{\langle q^2 \rangle} \tag{4.1}$$

with l ($= 1/\rho C_{sca}$, ρ being the number concentration and C_{sca} the scattering cross section) the mean free path and k_0 the wavevector in vacuum.

The angular dependence of the intensity $I(\theta)$ of the single scattering is also lost as the relation between the lab incidence and detection angle and scattering center incidence and scattering angle become not unequivocal. The intensity through a slab of size L becomes strongly affected on turbid samples for which the direct beam transmission drops drastically and the intensity can become homogeneous over most angles excluding the direct backward direction. For $L \sim l$:

$$T = \frac{I}{I_0} = \exp\left(-\frac{L}{l}\right) \tag{4.2}$$

Measured time autocorrelation functions have faster decays as a result of the phase shift from multiple scattering events adding up and no longer being simply $g(t) \sim \exp(-Dq^2t)$. Analytical solutions exist only for the diffusive limit and will be discussed later.

The state of polarization is also affected as a result of the multiple scattering events and not strictly by any anisotropy of the scattering centers. More information is provided in 2.3.

4.1.2 Strategies against multiple scattering in DLS

Strategies to bypass the multiple scattering in DLS exist. One alternative is to refractive index match the components [1], though this is not always a choice. Reduction of the scattering volume so that the size L of the sample is less than l^* can improve results as well.

The so called 3D-LS approach uses the cross correlation of two different scattered beams over the same $\boldsymbol{q}$ and scattering volume to preserve the common dynamic information and filter out the multiple scattering component which is decorrelated on the different detectors [6]. The two-color LS achieves the same effect using two different wavelength lasers [7]. Both approaches suppress the effect of double scattering and are applicable under weak to mild multiple scattering conditions.

4.1.3 Diffusive wave spectroscopy

In the strong scattering or diffusive limit light paths can be described by a random walk of step l^*. This is the domain of the diffusive wave spectroscopy. We briefly describe the DWS principle. Detailed description can be found in [8]. The field autocorrelation function is the result of the many scattering events. The total correlation function in the continuous limit is the following integral over all of the possible paths s (of length $s = nl$) given their normalized probability $P(s)$ [8].

$$g(\tau) = \int_0^\infty P(s')g_{s'}(\tau)ds' \tag{4.3}$$

$g_s(\tau)$ is the correlation function for path s with cumulative phase shift $\Delta\Phi_{s,B}(\tau) =$

$\sum_{i=1}^{n} \boldsymbol{q} \cdot \Delta \boldsymbol{r_i}(\tau)$ over n scattering events.

$$g_s(\tau) = \left\langle \exp\left(-i\Delta\Phi_{s,B}(\tau)\right)\right\rangle = \left\langle \exp -i\left(\boldsymbol{q} \cdot \Delta\boldsymbol{r}(\tau)\right)\right\rangle_q^n \tag{4.4}$$

On the right side we have taken the product over n steps and assumed each of them have the same average phase shift. Given the random nature of the process, we can take the leading term in the expansion of Eq. 4.4 and using Eq. 4.1 we get expression for the nth order scattering correlation function in terms of the number of scattering events or the total length of the path s.

$$g_s(\tau) = \exp\left(-\frac{n}{6}\left\langle \boldsymbol{q}^2\right\rangle \left\langle \Delta\boldsymbol{r}(\tau)^2\right\rangle\right) = \exp\left(-\frac{s}{l^*}\frac{k_0^2}{3}\left\langle \Delta\boldsymbol{r}(\tau)^2\right\rangle\right) = \exp\left(-2\frac{s}{l^*}\frac{\tau}{\tau_B}\right) \tag{4.5}$$

On the right of Eq. 4.5 we used the fact that for diffusion $\langle \Delta\boldsymbol{r}(\tau)^2\rangle = 6D\tau$ and defined $\tau_B = (Dk_0^2)^{-1}$.

The common solutions for Eq. 4.3 are for the case of samples within a infinite slab of thickness L, with a wide incident beam normal to one of the interfaces and detection either in transmission pass the slab or in backward direction.

For the transmission case, the early slope has the form:

$$\frac{\left(\frac{L}{l^*}+\frac{4}{3}\right)\sqrt{k_0^2\left\langle \Delta\boldsymbol{r}(\tau)^2\right\rangle}}{\left(1+\frac{4}{9}k_0^2\left\langle \Delta\boldsymbol{r}(\tau)^2\right\rangle\right)\sinh\left(\frac{L}{l^*}\sqrt{k_0^2\left\langle \Delta\boldsymbol{r}(\tau)^2\right\rangle}\right)+\frac{4}{3}\sqrt{k_0^2\left\langle \Delta\boldsymbol{r}(\tau)^2\right\rangle}\cosh\left(\frac{L}{l^*}\sqrt{k_0^2\left\langle \Delta\boldsymbol{r}(\tau)^2\right\rangle}\right)} \tag{4.6}$$

The decay is nearly exponential with rate $\tau_B(l^*/L)^2$ for Brownian diffusion. This characteristic time corresponds to the time the phase shift needs to become roughly unity, $nq^2\delta r^2 \sim 1$. For the diffusive limit across a distance L, $n = (L/l^*)^2$ so $\delta r = \lambda l^*/2\pi L \ll \lambda$. Therefore, in a DWS experiment ($l^*/L \ll 1$), small motions are probed, well below λ.

For the backscattering case of an infinitely thick slab the correlation function takes the form:

$$g(\tau) = \exp\left(-\gamma\sqrt{k_0^2\left\langle \Delta\boldsymbol{r}(\tau)^2\right\rangle}\right) = \exp\left(-\gamma\sqrt{\frac{6\tau}{\tau_B}}\right) \tag{4.7}$$

where $\gamma = z_0/l^* + 2/3 \approx 1$, z_0 is the distance of the first scattering from the surface, or alternatively the source of multiple scattering. z_0 is important when solving the diffusion equations in backscattering. The previous equation works relatively well, but the continuous approximation of Eq. 4.3 does not account for the discrete nature of the low order scattering paths.

The equations for $g(\tau)$ shown here are independent of the kind of motion being probed but they assume that the mean square displacement is homogeneous through the sample. Compared to single scattering DLS, DWS is sensitive to smaller displacement of the scatterers.

DWS under flow

When the scatterers are subject to flow, the ballistic motion adds an extra term to the phase shift $\Delta\Phi_{s,S}(\tau) = \sum_{i=1}^{n} \boldsymbol{q} \cdot \boldsymbol{v_i}(\boldsymbol{r_i})\tau$. Using Eq. 4.5 and the phase shift under laminar flow results in [9, 10]

$$g_s(\tau) = \exp\left(-2\frac{s}{l^*}\left(\frac{\tau}{\tau_S}\right)^2\right) \tag{4.8}$$

where $\tau_S = \sqrt{30}(\bar{\dot{\gamma}} l^* k_0)^{-1}$ is the average time per scattering event, with average shear rate $\bar{\dot{\gamma}} = \sqrt{\langle\dot{\gamma}^2\rangle}$. The factor $\sqrt{30}$ results from the spatial averaging of the velocities. According to Wu et al. [9] this equation is also valid within inhomogeneous flows.

Following Eqs. 4.6 and 4.7: In the transmittance geometry described previously correlation function decays as $(L/l^*)(\tau/\tau_S)$. For the backscattering case the decay exponent is τ/τ_S, mostly independent of the transport mean free path.

In theory, with sufficient knowledge of the scattering conditions it is possible to reconstruct the correlogram for an arbitrary flow profile and also possibly extract a full flow profile from measured correlation functions [11].

4.2 Experimental

4.2.1 Setup

2-axis goniometer

For the Brownian diffusion measurements we employed a flow cell as the one used and described in chapter 6. The thickness of the flow cell is $\sim 250\ \mu m$. Samples were introduced through syringe assisted flow. A Torus 532 nm continuous laser from Laser Quantum with 100 mW power was used. The power was cut as necessary by using combinations of achromatic filters and regulating the laser power to optimize collection time and statistics.

A semi-cylindrical lens is used to allow straight forward alignment and detection [12]. The incident beam and detection fiber intersect with the axis and lie on a plane normal to the lens axis. Given the cylindrical symmetry of the lens, both beam and detection suffer little diffraction as they are always normal to the lens surface.

Experimental angles were varied by use of two coaxial Huber step motors goniometers. The semi-cylindrical sample lens was mounted and aligned with its axis matching axis 1 on the goniometer. The detection optical fiber was mounted on an arm on axis 2 of the goniometer and aligned to collect at the reflection spot.

Both goniometers' angles were varied separately to set the angle of incidence θ_i and the detection angle θ_d shown in Fig. 4.1. The detection angle θ_d is defined with respect to $\boldsymbol{k_{EW}}$ (parallel to the flat face of the semi-cylindrical lens). The incident polarization was V in the laboratory frame and S (field parallel to the plane of reflection) according to the surface. A polarizer was introduced at the detection and the VV component or the depolarized VH component was selected. The V and H notation traditionally refer to laboratory axes (vertical and horizontal). VH or HV refer to light

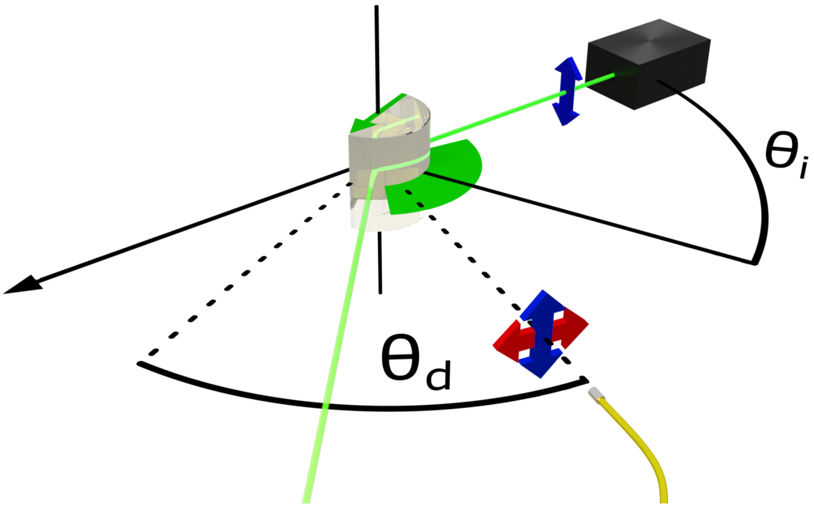

Figure 4.1: Schematic of the experimental angles for the diffusion experiments. θ_i is the angle of incidence of the laser beam with respect to the normal to the flat side of the semi-cylindrical lens. θ_d is the detection angle with respect to $\boldsymbol{k_{EW}}$. The allowed region is the green angular section confined by the critical angle θ_c in either direction from the normal. The forbidden region is comprised by all angles outside of this region. TIR is achieved for $\theta_i > \theta_c$. The initial polarization was fixed to V in the laboratory frame and S in the frame of reflection. The blue and red double arrows represent polarizer states. VV was achieved by using the second blue double arrow, VH with the red double arrow.

that has changed polarization after interaction with a sample.

Detection was done only through the semi-cylindrical lens. Given refraction at the sample-glass interface light can only propagate to the detector below the TIR critical angle. In terms of θ_d that would be the angular region $= \{90 - \theta_c \ldots 90 + \theta_c\}$. We will refer to this region as the allowed region. No light should be detected in this forbidden region for a Fresnel interface. An FPGA correlator comparable to the ALV 6010/200 according to [13] with a fastest time of 4 ns was used.

Angular dependent reflectivities were measured using a photodiode detector placed on the θ_2 goniometer and doing θ/θ_2 scans.

Rheometer

The velocimetry measurements used the same setup described in chapter 3 mounted on a Malvern Kinexus Pro+ stress controlled rheometer with the minor addition of a polarizer between the sample and detection. The lower plate on the side of detection is an untreated BK7 glass slide. The top flat geometry is made of untreated fused silica.

The incident beam polarization was V in the laboratory frame of reference and S along the reflection surface (technically the incident light was polarized horizontally in the laboratory but we stick to the same notation). No polarizer was used after the laser but only the laser's built in polarization was used. The detection polarizer is used to select the VV component or the depolarized VH component.

A Torus 532 nm continuous laser from Laser Quantum with 100 mW power was used. The beam was steered by a two mirror system. The power was cut as necessary by using combinations of achromatic filters and regulating the laser power to optimize collection time and statistics.

A PMT (Hamamatsu, provided with the correlator unit) was used for detection. The correlator used was a Flex01LQ-12 from Correlator.com with 1088 multi-tau channels.

4.2.2 Samples

For the proof of principles both quiescent and under shear, we used 190 nm in diameter PS (n=1.59) dispersion in water and water glycerol mixtures covering a broad range of concentrations.

Diffusion For the diffusion experiments water dispersions were used at 10% (multiple scattering) and 2.7 10^{-3}% (single scattering) concentrations. Corresponding transport mean free paths l^* with positional correlations [14] for the different concentrations calculated using LS Instruments' online Mie calculator [15] are 19.5 μm and 75 mm. $\theta_c = 61.0°$ for the water-BK7 interface.

Shear Newtonian reference velocimetry experiments were carried out on a 77% glycerol and 23% water mixture (n=1.438). A batch of 10%w in water was mixed with 100% glycerol, following, the water was evaporated to recover the 10%. The lower concentrations The concentrations used were: 10, 5, 2.5, 1.25, 0.62 and 0.2 %. Transport mean free paths with positional correlations [14] for the different concentrations are 67, 127, 249, 490, 1000 and 3000 μm. Fig. 4.2 shows l and l^* as a function of concentration for the system used here. Both length scales are almost linear in concentration below ϕ =0.1. $\theta_c = 71.09°$ for n_2=1.438 and incident angle $\theta_i = 72.8°$.

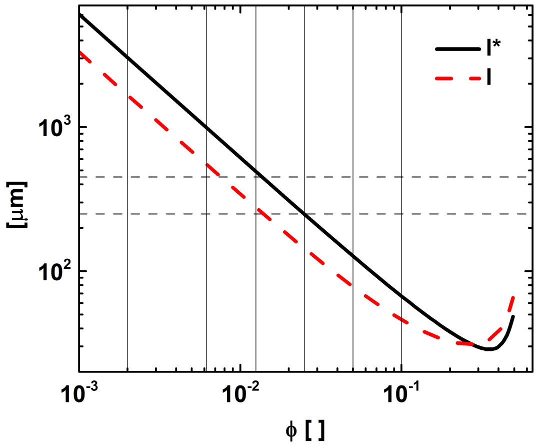

Figure 4.2: Scattering length l and reduced scattering length or transport mean free path corrected for positional correlations l^* (average distance a photon travels in a turbid medium before completely changing the direction); values calculated with LS Instruments' online Mie calculator plotted as a function of the volume fractions used on the Newtonian reference velocymetry experiments. Horizontal dash lines correspond to the plates' gaps of 250 and 450 μm. Vertical lines indicate the concentrations used.

We further tested the capacities of the techniques on dense colloidal suspension at large volume fraction close and beyond glass transition. This type of viscoelastic suspensions are known to give rise to slip under shear.

Shear: highly concentrated dispersions High volume fraction particle dispersions used PMMA (n=1.4934) spheres with 214 nm diameter in dodecane (n=1.421). $\theta_c = 69.2°$ for n_2=1.421 and incident angle $\theta_i = 77.4°$. The samples volume fractions were determined from their linear rheology plateau based on [16].

Three samples were used: A 57% repulsive system close to the 58% glass transition, a 60% repulsive glass and a 60% attractive glass.

To make the attractive glass polybutadiene of 881 kDa solution in dodecane was mixed with th 60% PMMA dispersion and then excess solvent was evaporated under heat and vacuum to back to 60% PMMA concentration. The final concentration for the polymer was 3.7% in weight. The size ratio of the polymer and the colloids was 0.28 according to the Rg in dilute solution and 0.036 according to osmotic shrinking of the polymer. The depletion at 2R has a value of -22 kT according to the Generalized Free Volume Theory [17].

4.2.3 Ray tracing simulations

Multiple scattering signals are a result of the complex paths coherent photons travel within the sample. Moreover, the phase shift gained by a particular scattering event depends on the local motion of the scatterer. The knowledge of the paths is therefore necessary to completely understand the signal in specific conditions and to be able to predict it.

Monte Carlo simulations are widely used to obtain numerical approximations of the distribution of photon paths [18, 4]. We opted for a full per single Mie scattering event simulation in contrast to the diffusive limit which would not account for the single scattering. We also took into account polarization with Stokes vectors.

Our objective is foremost to understand the nature of the signal and whether and how the near wall single scattering information can be retrieved from EW-DLS measurement of from turbid samples. In addition, our experiments were done with a wide range of l^*'s so the diffusive limit is not always guaranteed. Finally, we are also interested in the polarization of the signal.

The code

Photon tracing consists on following the path of photons as they propagate through space (the sample) according the laws of optics. Excluding interference, this gives a good picture of reality. By following the photons' propagation one can obtain the spatial distribution of the photon trajectories resolving scattering order (number of scatterings per photon). This not only allows to reproduce the experiments (correlograms and intensities), but gives access to the spatial and frequency distributions according to the scattering order.

Photon tracing simulations are well established and used when treating propagation of light in turbid media [19, 20]. That includes biological tissue as well as more rare media in atmospheric and oceanographic optics. We based ourselves on existing C code for MC polarized Mie scattering available in the website of J. C. Ramella-Roman [21], specifically, the code that uses quaternions for polarization plane rotation was used. Quaternions are mathematical tools for easy rotation of vectors about arbitrary axes [22]. The articles in reference and the website provide explanations for most of the workings of the code [23, 24]. We modified the code to mimic our experimental conditions. This included adding an evanescent wave-like illumination with proper polarization, appropriate boundary conditions, fiber like detector and the machinery to record and analyze the quantities of interest.

The scattering centers are not explicitly defined. The scattering events happen according to Beer Lambert law statistics given the specific μ_s. Positional correlations between particles are not considered ($S(q) = 1$). No scattering events occur below the particle radius (95 nm) from the wall. The simulated photons are polarized and therefore we use Stokes vectors $\boldsymbol{S}$ and Mueller matrix ($\boldsymbol{M}$) algebra [25]. The Stokes vectors contain the polarization of a photon and the Mueller matrices operate on them in terms of their intensity. The scattering is calculated only for monodisperse spheres according to Mie theory [26]. Two mutually orthogonal 3 dimensional support unit vectors are used as reference plane for the polarization ($\boldsymbol{u}$ along the direction of propagation and $\boldsymbol{v}$ originally set along the direction of the V incident polarization). The refractive indexes used had only a real part. A weak absorption coefficient $\mu_a \sim 10^{-8}\ \mu m^{-1}$ comparable to the one of water was used. Scattering angles, distance traveled, initial position and other random values are chosen using Monte Carlo (MC) methods: inverse transform sampling (described in [27] and chapter 5 of [28]) and rejection sampling. The random number generator is as used on Ramella's code and is sufficiently good for the simulations.

Photon package life cycle

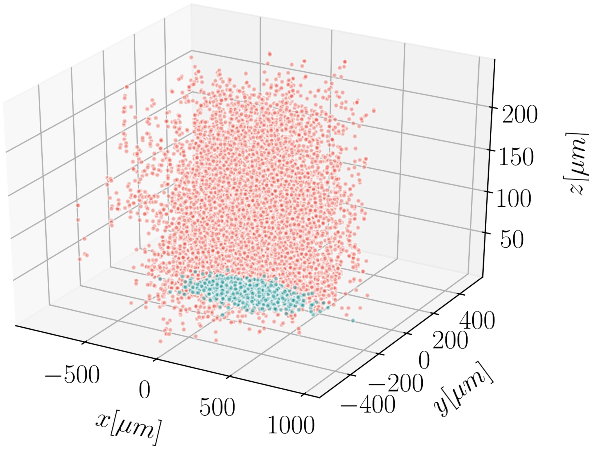

Figure 4.3: Detected scattering events within a simulation with $l^* < gap$ at $\theta_2 = 90°$. The blue dots at z ∼0 are the first scattering events of each photon launched and the rest of the dots are the following scattering events.

Several millions of photons are used in a simulation. Every photon launched is interpreted as a package of photons with weight $W = 1$ at time 0. The weight represents the intensity, it is proportional to the number of photons being traced and will go down by absorption per step or by loss at the interfaces. By having this weight decrease monotonically each photon can map more space with a given statistical weight and not disappear completely by transmission out from the box.

The life of a photon package is as follows:

1. Create a photon package within the EW distribution at $\boldsymbol{r}$ (starting from the particle radius) with the inverse sampling method (for the EW) and the Box-Muller transform (for Gaussian profiles with different width on x and y directions as in real life). Set W=1, $\boldsymbol{u}$ along $\boldsymbol{k_{EW}}$ $(= [1, 0, 0])$ and $\boldsymbol{S}$ $(= [1, -1, 0, 0])$ and $\boldsymbol{v}$ $(= [0, 1, 0])$ to the S polarization.

2. Obtain the azimuth (into the scattering plane) angle β and scattering angle α according to Mie theory with the help of the rejection method. Rotate $\boldsymbol{S}$ by β into the scattering plane with $\boldsymbol{M_{rot}(\beta)}$ and then apply $\boldsymbol{M_{Mie}}(\alpha)$. Rotate $\boldsymbol{v}$ along $\boldsymbol{u}$ by β and then $\boldsymbol{u}$ along $\boldsymbol{v}$ by α using quaternions.

3. Choose length s of travel according to the Beer-Lambert law statistics using the scattering coefficient μ_s.

4. Update the photon position, $\boldsymbol{r'} = \boldsymbol{r} + s\boldsymbol{u}$.

   According to the new coordinate:

   (a) If past an interface but not in the detector's direction. Reflect first rotating into the reflection plane with $\boldsymbol{M_{rot}^{SP}}$, then apply the reflection Mueller matrix $\boldsymbol{M_R}$ [29] (act equivalently on the support vectors) and finally $\boldsymbol{M_{rot}^{SP\,-\,1}}$. Use specular reflection on the component of $\boldsymbol{u}$ parallel to the interface normal $\boldsymbol{N}$. For our case $\boldsymbol{N} \parallel \boldsymbol{z}$ therefore $\boldsymbol{u'_z} = -\boldsymbol{u_z}$. Move according to 3 with the new $\boldsymbol{u'}$. Reduce weight according to Fresnel's reflection equations.

   (b) If past an interface and after refraction $\boldsymbol{u}$ in the detector's direction do as on 4a. Additionally transmit (refract) applying the transmission Mueller matrix $\boldsymbol{M_T}$ and pass by the polarizer applying the polarizer Mueller matrix $\boldsymbol{M_{pol}}$. The appropriate detector channel which discriminates according to angle and scattering order is fed overall the following

$$W\boldsymbol{M_{pol}}\boldsymbol{M_{rot}^{pol}}\boldsymbol{M_{rot}^{SP\,-\,1}}\boldsymbol{M_T}\boldsymbol{M_{rot}^{SP}}\boldsymbol{S} \tag{4.9}$$

   (c) If outside of a predefined volume threshold. The photon dies.

5. Reduce W by multiplication with the "albedo" ($= \frac{\mu_s}{\mu_s+\mu_a}$, $\mu_s \gg \mu_a$).

6. If W is more than a minimum threshold go back to 2, if not then the photon dies.

   (Here the photons still have a chance to survive. If they survive their weight is multiplied by the 1/chance.)

Every motion step is determined through a Beer Lambert law distribution (exponential) but the loss of weight is independent of the effective distance travel, it is only proportional to the number of scatterings.

Detection

We are using a slab simulation box with the EW at the lower interface just as we used in real life. For the detection we mimicked the detection apparatus in the real setup. The real detection fiber was equipped with a grin lens with divergence angle DA of 0.13° and beam diameter BD of 0.5 mm (see Fig. 4.4). We implemented detectors with acceptance angles (DA) of 1°, beam diameter of 0.5 mm and position from the sample comparable to the real life experiments. The photons are therefore detected only when they traveled towards the detector (set at discrete θ_2 values). The results were not very sensitive to the BD used so increasing the BD is a possible strategy to reduce the noise in the simulation. We did not implement the BK7-air interface of the semi-cylindrical lens.

Note that the reflected portion of the photon package continues to diffuse within the sample until it meets one of the conditions for its elimination.

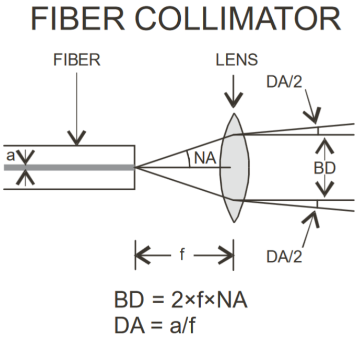

Figure 4.4: Real optical fibers' operating principle. Taken from OZ Optics' website.

Calculating correlation functions

For every single photon that makes it to the detector we store its Stokes vector, weight, order of the scattering and the coordinate $\boldsymbol{r}$ and scattering wave vector $\boldsymbol{q}$ of every single scattering event. This has to be done only once for a given set of optical and geometrical conditions. Using this data we can calculate the correlation function, power spectrum and other quantities of interest using the same photon paths. We have implemented these post processing on a Python Jupyter notebook.

Diffusion For calculating the correlograms in the diffusion case, the phase difference acquired by every detected photon s is the following sum over every scattering events i.

$$\Delta\phi_{s,B}(\tau) = 6\sum_i D(z_i) q_i^2 \tau \tag{4.10}$$

The correlogram is the weighted sum of the exponentials of the phase [30].

$$g(\tau) = \frac{\sum_s W_s \exp\left(-\Delta\phi_{s,B}(\tau)\right)}{\sum_s W_s} \tag{4.11}$$

Note that here the actual $\boldsymbol{q}$ at each scattering event is used, not an average as for the diffusive limit analytical solutions (Eq. 4.4).

Flow For the flow case the phase shift acquired at each scattering event is $\boldsymbol{v} \cdot \boldsymbol{q}$ so the total phase shift per photon detected is

$$\Delta\phi_{s,S}(\tau) = \sum_i \boldsymbol{v}(\boldsymbol{r_i}) \cdot \boldsymbol{q_i} \tau \tag{4.12}$$

where the velocity is calculated according to the coordinate $\boldsymbol{r_i}$ of the scattering event in the specific flow profile. For a linear flow profile of shear rate $\dot{\gamma}$ and slip length v_0 in the $\boldsymbol{x}$ direction the velocity is $\boldsymbol{v} = v(z)\boldsymbol{x} = (v_0 + \dot{\gamma}z)\boldsymbol{x}$. The real part of the resulting correlation function is

$$g(\tau) = \frac{Re\left(\sum_s W_s \exp\left(-i\Delta\phi_{s,S}(\tau)\right)\right)}{\sum_s W_s} \tag{4.13}$$

4.3 Simulation of multiple scattering in EW

Here we evaluate the scattering and correlation functions measured in EW-DLS on samples with varying scattering power up to turbid samples using the MC ray tracing simulations. We established that one can indeed recover the single scattering dynamics from EW-DLS measurements on turbid multiple scattering samples. Ray tracing simulations allow us to understand the effect of an EW illumination on multiple scattering (DWS in the limit of high turbidity) correlation spectroscopy by having full access to the spatial and phase statistics of the photons. With them we verify and elaborate our experimental observations. The simulations give us a grip over all the experimental variables so we can make more informed predictions.

ϕ [%]	n_{medium}	θ_i [°]	dp [nm]	l [μm]	l^* [μm]
30	1.428	73	399	11	20
10	1.33	66	212	12	20
10	1.428	73	399	33	61
5	1.428	73	399	66	121
1.25	1.428	73	399	265	486
0.3125	1.428	73	399	1061	1943

Table 4.1: Samples simulated in the section.

In what follows we show results for simulations over the samples in table 4.1. All of the simulations were performed with spherical PS particles of 190 nm in diameter using 532 nm light and a 250 μm gap. The results shown are from the average detection at 5 discrete angular detector positions ($\theta_d = \{88° \dots 92°\}$) to improve the statistics and only for the photons that made it to the detector.

4.3.1 Random walk and scattering order

In Fig. 4.5 we show trajectories projected in the xz plane for a random sample of 10 photons per optical condition. From these small samples we can see the effect of having different mean free paths under a constraint space. The shorter l values more mapping of the space near the EW and less spread in the xy directions. They also result in significantly more scattering events as shown in Fig. 4.6.

For higher mean free paths we see a tendency to select more sharp turns or more backscattering events in the trajectories. This is partially true as indeed we expect photons that travel in longer straight trajectories to necessarily escape the detection volume. From the real experiments we know that the amount of light from multiple

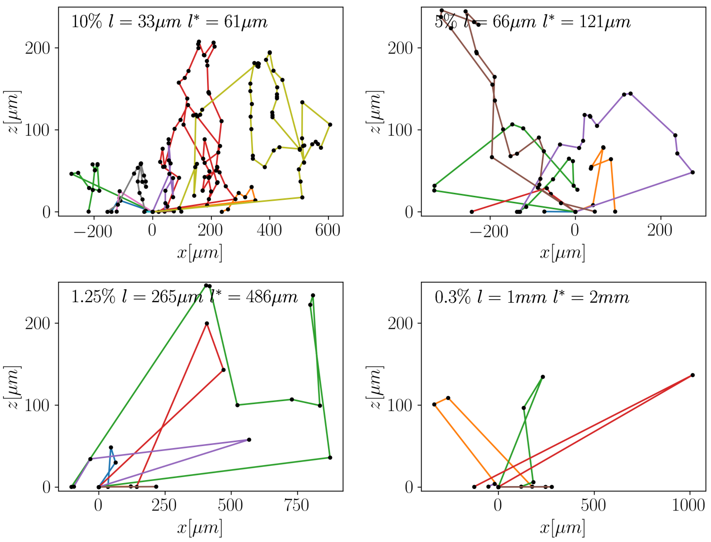

Figure 4.5: Trajectories of 10 photons for different values of l^* with *gap*=250 μm. The parameters used are similar to those used in 4.5.

scattering decreases sub-linearly with $1/l$ implying longer residence of long mean free path photons. The incongruence can be explained by our use of specular reflection within the simulations which does not match the real life experiments that contain scattering by surface defects. In fact Fig. 4.5 does not show the points where the photon was reflected. Our simulation results are therefore expected to be in poor agreement with the experiments for long l, i.e. low turbidity samples.

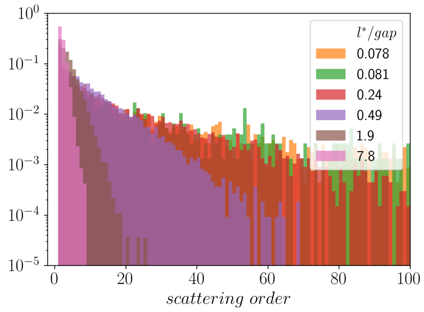

Figure 4.6: Normalized histogram of the order of scattering events of the photons. We have trimmed the x axis to highlight the lower values but the shorter l^* samples actually have contributions up to around order 500.

In Fig. 4.7 we see that the photon trajectories can indeed be well described by a random walk when $l^* < gap$ at least for the in plane components (x and y). The z component becomes quickly localized given the constraint of the top and lower wall.

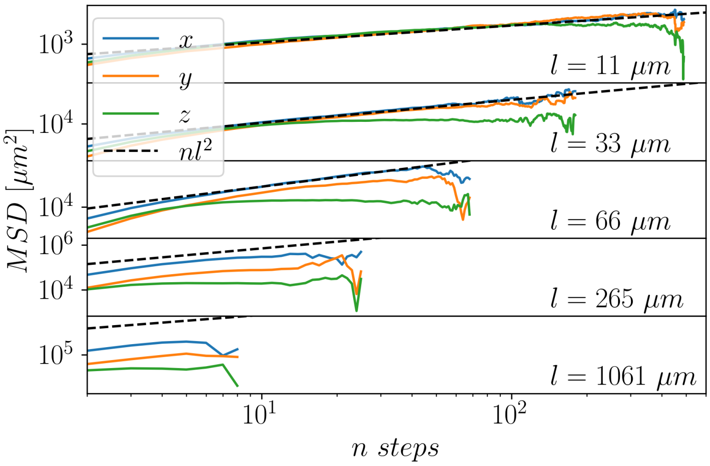

Figure 4.7: Mean square displacement of the propagating photons under the gap constrain. The dashed black lines are the values for the theoretical random walks.

4.3.2 Spatial distribution of scattering events

The near wall dynamics are explored by all photons within the first scattering event. The subsequent scattering events migrate fast into the bulk and most of the events are far from the evanescent field. We can confirm this in Fig. 4.8 that shows the histograms of the $\log(z/gap)$ for all of the scattering events. We can see in the figure the portion of single scattering near wall events that goes directly into the detector. The ratio of this to the total area within the EW is equal to the ratio single to multiple scatterd photons. Mostly strongly forward scattered photons will stay within the evanescent field.

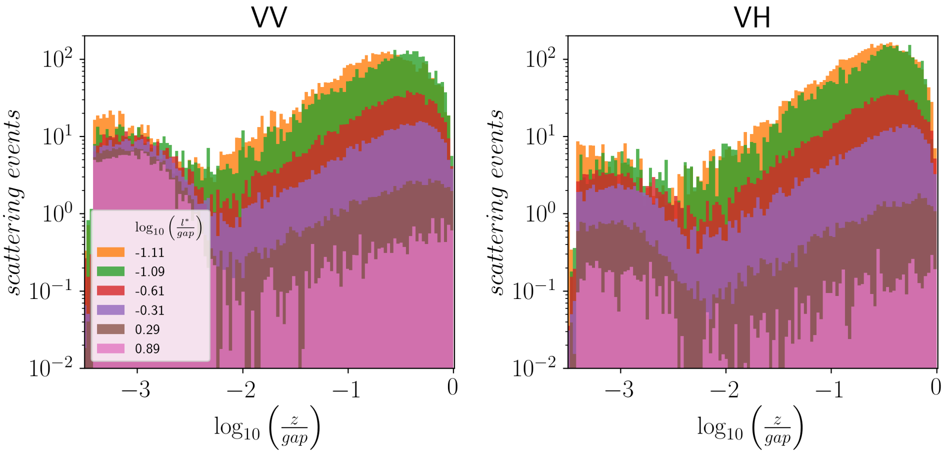

Figure 4.8: Histograms of the $\log(z/gap)$ of the scattering events of the photons detected at 90°.

The peak at -0.3 in Fig. 4.8 is close to the center of the gap and is a result from the logarithmic binning used for the histogram. The photon displacement can be better evaluated in Fig. 4.9. The density of scattering events decreases with the distance from the evanescent wave. For larger l^* values the distribution flattens.

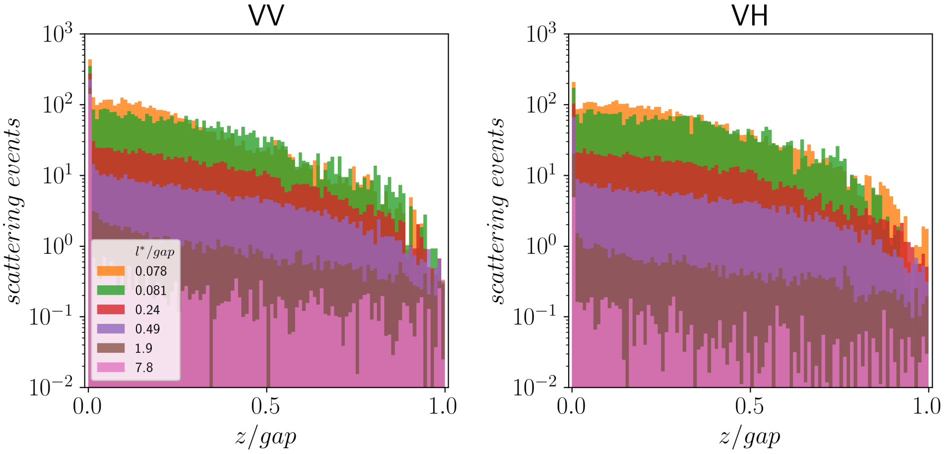

Figure 4.9: Histograms of the z/gap of the scattering events of the photons detected at 90°.

4.3.3 Phase shift and recovery of single scattering dynamics

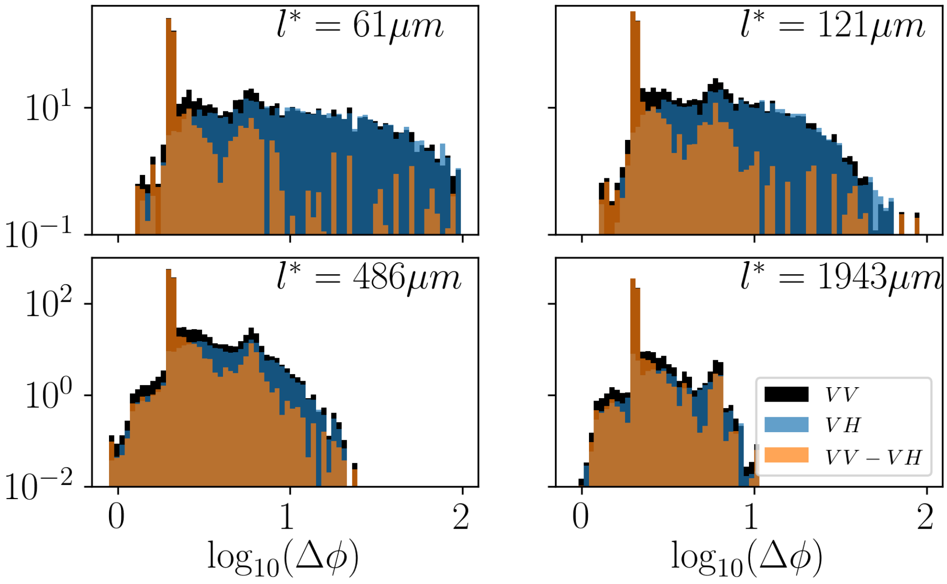

Figure 4.10: Histograms of the phase shifts due to diffusive motion of the material in the gap acquired by the photons.

Single scattered photons contain one single phase shift of magnitude Dq^2 for diffusion. In contrast, the multiple scattering of the photons results in accumulation of phase shifts at each scattering event and a consequent frequency separation from the single scattered photons. The histogram of the accumulated phase shifts in VV for constant diffusion coefficient $D_0 = 1$ in Fig. 4.10 contains a strong peak at 0.3 corresponding to the single scattering at 90°. Note that we use $k = 1$. This peak is absent from the VH histogram that does not contain single scattered signal. The multiple scattering signal is then spread over a wide range of phase shifts.

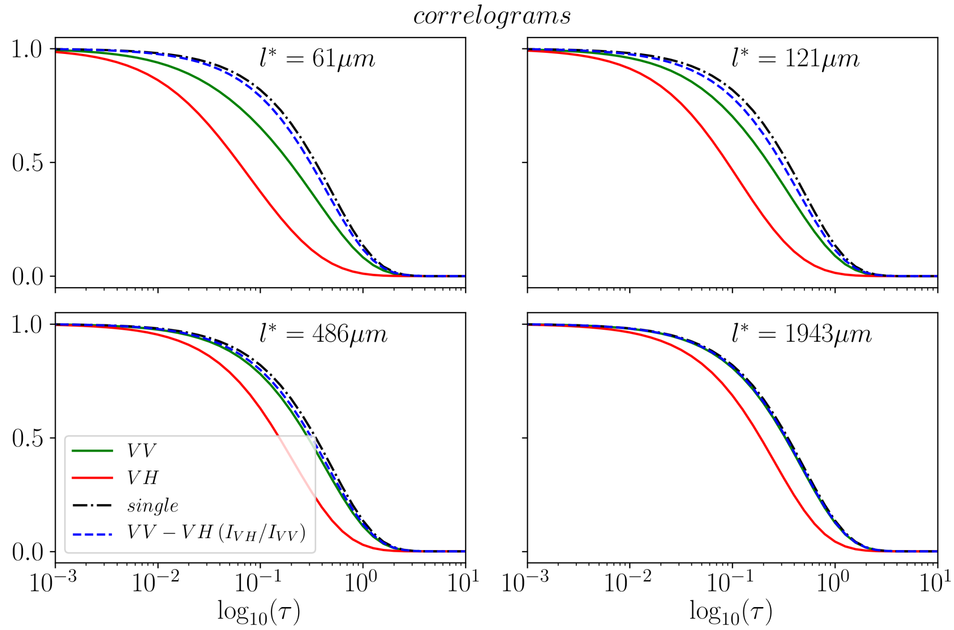

Figure 4.11: Field correlograms for the VV, the VH and their weighted difference.

Apart from the single scattering peak, the VV and VH histograms resemble one another. This means that their difference should approximate the single scattering distribution as seen in Fig. 4.10. In addition, this means that we can potentially subtract the VH correlogram from the VV correlogram to recover the single scattering correlogram. We attempt this with the next simple equation that we can apply to real experimental data.

$$g(\tau) = g_{VV}(\tau) - g_{VH}(\tau)\left(\frac{I_{VH}}{I_{VV}}\right) \tag{4.14}$$

I_{VH} and $_{VV}$ are the magnitude of the detected intensity. The treatment is shown in Fig. 4.11. It recovers the single scattering correlogram to within 10% of the theoretical values. This is thanks to the strength of the single scattering signal from the EW and to the cumulative phase shift inherent to multiple scattering. The VV correlograms are considerably closer to the single scattering one than the VH but their average time is still a factor of 2 from the single scattering for $l^* = 61\ \mu m$.

4.3.4 Strong phase shift under shear flow

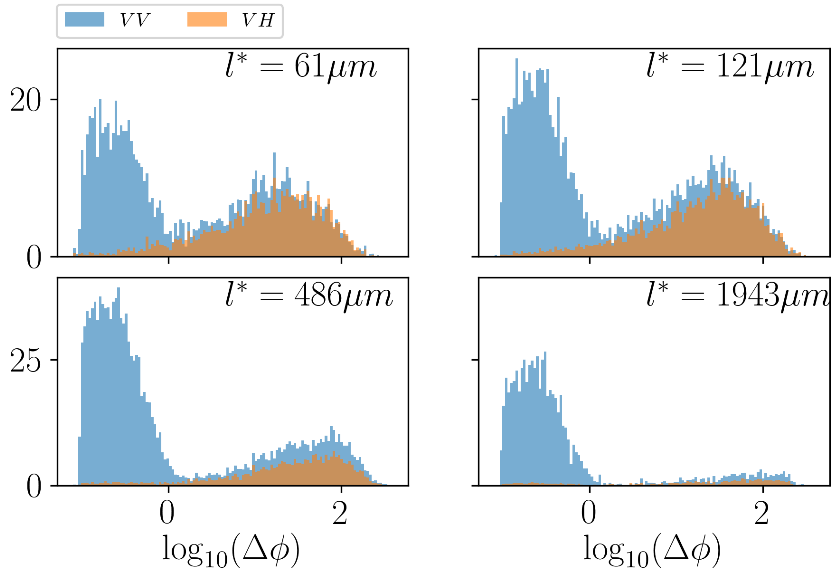

Figure 4.12: Histograms of the phase shifts due to shearing ballistic motion of the material in the gap acquired by the photons.

If the cumulative phase shift imposed by the multiple scattering is strong enough then the difference between the multiple scattering and single scattering contributions should become large. It could lead to correlation functions with two distinct modes that we should be able to see directly in the correlogram. This condition should be met when the sample is submitted to a velocity gradient along the direction perpendicular to the TIR surface. This can be realized when the material in the gap is sheared and the velocity increases with z. In this case the histogram of the phase shifts is clearly a bimodal distribution as in Fig. 4.12 and the single scattering signal becomes well separated from the multiple scattering signal.

The VV field correlograms in Fig. 4.13 are composed of a slow near wall oscillating mode and a faster multiple scattering mode. The slow mode is equivalent to the single

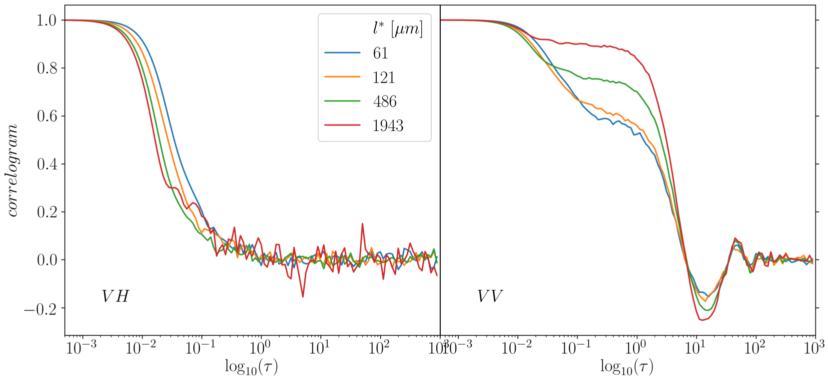

Figure 4.13: Simulated correlation functions of the photons detected at 90°.

scattering evanescent wave velocimetry with only some minor contamination of the multiple scattered photon. The faster mode is contains mostly information from the bulk and is found on both the VV and the VH correlograms. Note that the specific frequency distribution is a function of the specific flow profile in the gap and cases where one does not obtain a sharp distinction between the single and the multiple scattered light are certainly possible.

4.4 EW-DLS of turbid Brownian dispersions at rest

4.4.1 Reflectivity and penetration depth

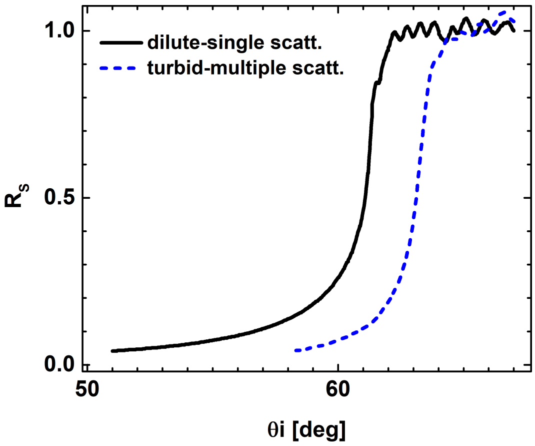

Figure 4.14: Reflectivity curves for 10% and 2.7 10^{-3}% PS in water.

We have measured the reflectivity for both the low volume fraction (single scattering) and the high volume fraction (turbid) dispersions. They are shown in Fig. 4.14. It appears that there is a shift of about 2° of the TIR regime. As discussed in chapter 5 there is no consensus of the best way to describe this shift but the most likely explanation is that there is a shift in the real part of and effective refractive index. Using simple mixing rule for PS and water leads to a variation of the refractive index n of the dispersion of 1.33 (pure water) to 1.36 for volume fraction 10%. The 3% change of refractive index is enough to account for a shift a critical angle of 2°.

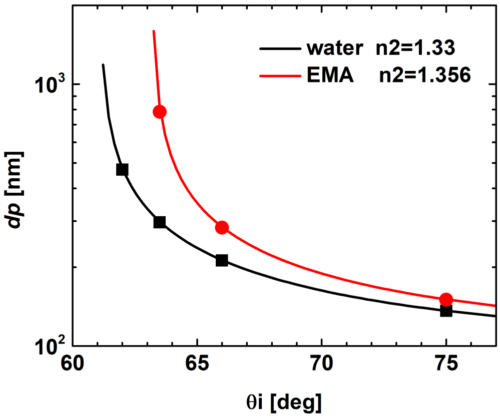

Figure 4.15: Theoretical field penetration depths for the interface of BK7 with water and with an EMA of 10% PS in water. The symbols refer to the values of θ_i used. The refractive indexes used here are $n_1 = 1.52$, $n_{water} = 1.33$, $n_{PS} = 1.59$ and $n_{EMA} = 1.356$.

The value of the medium refractive index has an incidence on the value of the penetration depth. The evolution of penetration depth as a function of the incidence angle are plotted in Fig. 4.15, for two medium refractive indexes one corresponding to water, the other corresponding to an effective medium approximation (EMA) for water and PS. *dp* varies strongly close to the critical angle of TIR but does less so far away from it. Differences between the two medium are marked close to the critical angle. The value of the penetration depth in this range of incidence angle depend strongly on the choice medium refractive index. But away from the critical angle, the value of *dp* is not too much affected by the choice of n_{eff}. The points in Fig. 4.15 correspond to the measurements done. The 62° falls outside TIR when the EMA is used. In case of a BK7-water interface, computed values of the field penetration depths for the incident angles θ_i =62, 63.5, 66 and 75° used in the measurements are 471, 297, 212 and 136 nm respectively.

It is unclear which refractive index should be used in the following. However, most of the following results are not affected significantly by the small change in refractive index. We use the refractive index of the medium from here. Do note however that the smallest θ_i in our data falls outside of the TIR.

4.4.2 Scattered intensities, angular dependence

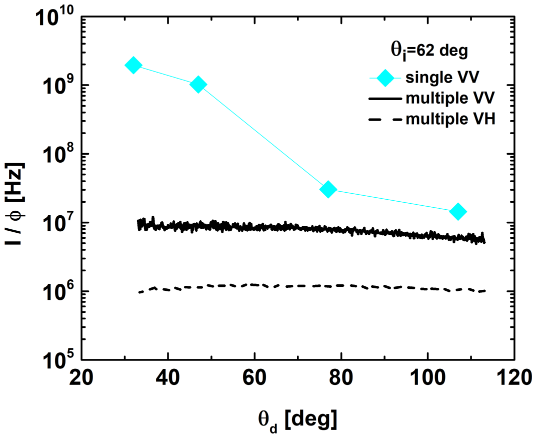

Figure 4.16: Scattered intensity normalized by volume fraction ϕ as a function θ_d with $\theta_i = 62°$ for the single scattering and multiple scattering samples. The continuous line corresponds to the turbid sample as measured by power meter, the values match those measured through the PMT (not shown).

The scattered intensity $\langle I \rangle$ measured in the case of the non turbid dispersions cannot easily be linked to EW scattering by the PS particles. This contribution is masked by an often stronger contribution from the roughness of the glass. However the latter is not expected to fluctuate in time while the former is due to the presence of the Brownian motion. Therefore we evaluate the scattered intensity by the dispersion using the measured correlation functions. We assume that the probed intensity fluctuation are all due to the Brownian motion of the particles within the EW. The proportion of that fluctuating light is retrieved by the amplitude $A = g(\tau \to 0)$ of the normalized autocorrelation function $\langle I \rangle_{dynamic} = A\langle I \rangle$ [31].

The scattered intensities normalized for particle concentration for different incident angles are shown in Fig. 4.16. The intensities fail to overlap and the angular dependence of the dilute sample is also significantly stronger than the concentrated one.

The strong low angle intensity for the dilute dispersion is attributed to the large contribution of the glass static scattering [32]. The values of the dynamic amplitude (percentage of light coming from the diffusing particles) shown in Fig. 4.18a for the dilute dispersions are lowest at low angles, confirming that in fact the static intensity is mostly due to surface imperfections.

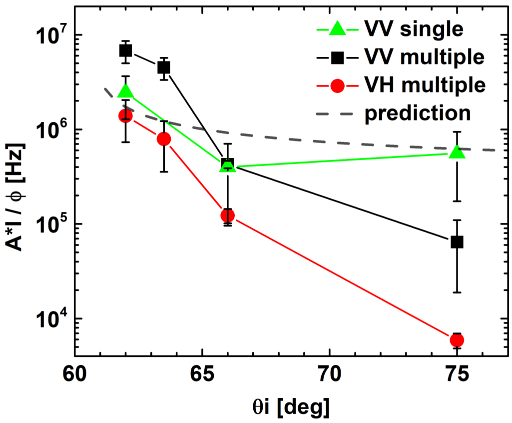

Figure 4.17: Dynamic amplitudes of correlograms averaged over θ_d. The prediction curve corresponds to $dp \exp\left(-\frac{R2}{dp}\right)$ scaled arbitrarily to match the observed values.

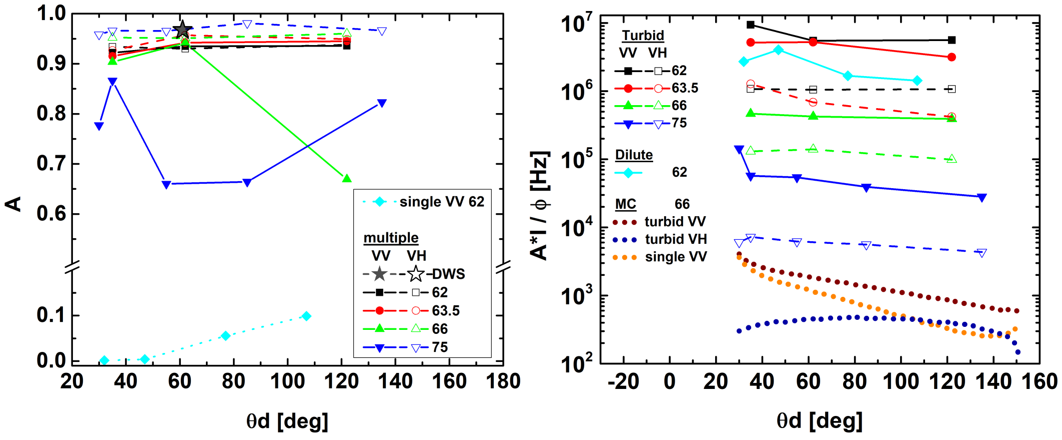

(a) (b)

Figure 4.18: (a) Dynamic amplitudes of the correlograms for different values of θ_i. The values referred to as DWS were measured with a transmitted beam ($\theta_i = 0°$) in the backscattering geometry ($\theta_d = 60°$) (b) Dynamic intensity normalized by volume fraction. The dotted lines correspond to results from MC simulations at comparable conditions to the real experiment. The MC simulation results are scaled arbitrarily.

Large intensities where measured for the 10% dispersion. Moreover a strong depolarized VH component could also be measured. VH intensities were a factor of 3 to 10 times apart from the VV intensities. A clear sign of multiple scattering presence where otherwise polarization should be conserved.

From Fig. 4.18b we see that the intensity scattered by the particles in the turbid VV and in the dilute samples is similar. This indicates that the VV multiple scattering signal contains a fair amount of single scattered light.

The dynamic intensity decreased with the distance from the critical angle in agreement with

$$\frac{I}{I_0} = \int_R^\infty \exp(-\frac{2z}{dp})dz = \frac{dp}{2}\exp(-\frac{2R}{dp}) \tag{4.15}$$

To show this we present in Fig. 4.17 the intensities (averaged over θ_d) vs θ_i. The average is justified by weaker variation in the dynamic intensity over θ_d (see Fig. 4.18b). The data from the dilute single scattering sample follows relatively well the theoretical curve though dynamic intensities in EW-DLS are usually unreliable. The multiple scattering signals on the other hand showed stronger variation with its values overlapping with the dilute case at $\theta_1 = 66°$.

In Fig. 4.18b we can see the dynamic intensities as a function of θ_d together with results from the Monte Carlo simulation (250 μm gap, 10% concentration of PS spheres of 190 nm in diameter in water). The simulation results reproduce well the measured data including: The ratio VV/VH at high angles, the weak variation of VV for the multiple scattering case, the stronger variation of the single scattering and also the kink close to the critical angle in the multiple scattering VV. From the simulations we see that for particles with non isotropic scattering the forward scattering is mostly single scattering in nature. The VH signal which is mostly of multiple scattering origin varies to a lesser extent.

4.4.3 Dynamics

We embark to measure the DLS / SLS for TIR turbid sample. As the intensity is large, measurements of both average (static intensity) and intensity autocorrelation function are relatively straightforward. The question then arise of what information on the static and dynamics of the sample can be retrieved from the measurements.

Based on the simulations shown above, we may expect to be able to retrieve single scattering type of information (q-dependent intensity and q-dependent dynamics) that will directly arise from the within EW, near wall sample. Moreover depolarized VH scattering dynamics should provide bulk like information, i.e. diffusion in the bulk.

Non-turbid dispersion

The non-turbid case showed the typical strong heterodyne EW-DLS correlation functions related to near wall diffusion [1]. Some correlograms are shown in Fig. 4.19. the early slope values at different *dp* and wavevectors can be found in Fig. 4.22. Note that the dilute single scattering near wall values are faster than the bulk values yet this is entirely a known experimental artefact [1] (for more details please visit the appendix 4.A.1). The artefact should be equally present in the multiple scattering case.

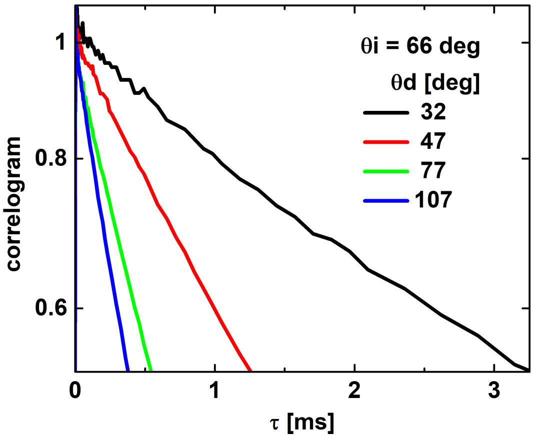

Figure 4.19: Early slopes of the dilute sample measured by EW-DLS.

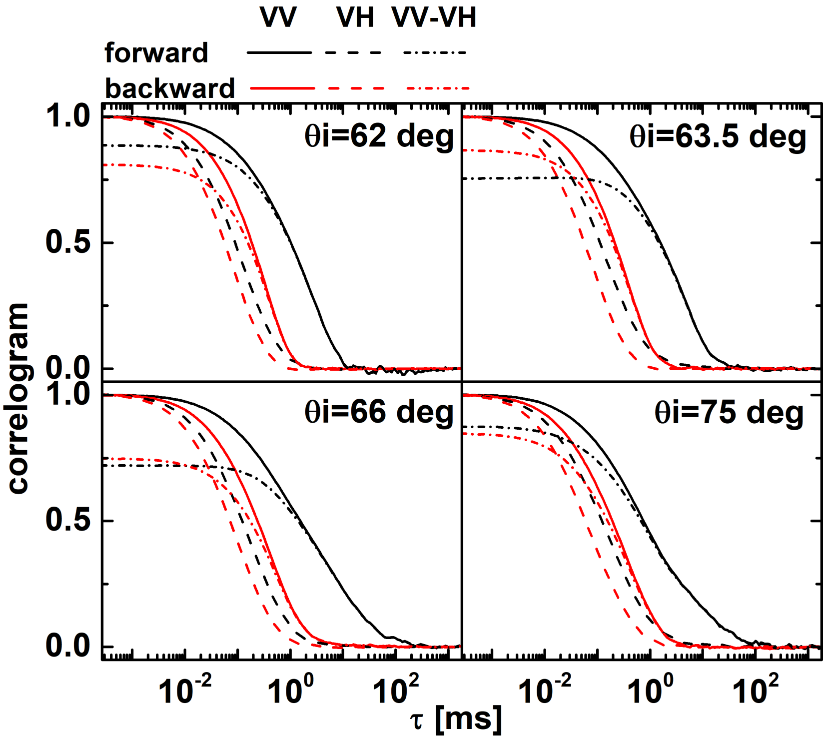

Figure 4.20: Subtraction treatment for the different θ_i for forward scattering (low θ_d) and backward scattering (high θ_d) (θ_d values vary). The results of the subtraction were not renormalized.

Turbid dispersion: recovering the near-wall single scattering dynamics

Correlograms on turbid media were easy to measure given the strong dynamic intensities available. We demonstrated with the Monte Carlo simulations that for EW-DLS experiments it is at least theoretically feasible to recover the single scattering dynamics using the VV and VH measurements with the following manipulation.

$$g_{single} = g_{VV} - g_{VH}\left(\frac{A_{VH}I_{VH}}{A_{VV}I_{VV}}\right) \tag{4.16}$$

The correlograms in Figs. 4.20-4.21 were normalized according to the general Siegert relationship (Eq. 3.4 in chapter 3 after fixing $\tau = 1$ s as the baseline and $\tau = 10^{-4}$ s as the full amplitude. The subtraction in Fig. 4.20 is far less striking than the one on simulated case in Fig. 4.11 with the effect being mostly in the early slope. The example in Fig. 4.21 shows how well the agreement between the subtraction approach and the dilute single scattering correlograms. As a characteristic time we took

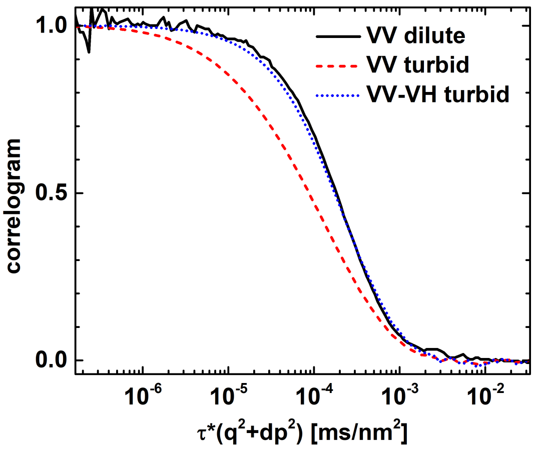

Figure 4.21: EW-DLS VV correlograms of the non-turbid dilute sample, the turbid sample and recovery of the single scattering correlogram from the turbid signal (normalized by amplitude) with the subtraction treatment. The time axis was rescaled with $q^2 + dp^{-2}$ to collapse the correlograms measured at different q values.

the early slopes determined by linear fit of the log-lin of the correlogram. The early slopes after the subtraction in Fig. 4.22 are quite close to the dilute single scattering values. The lowest dp values were considerably faster. We believe that this was a consequence of strong surface scattering leading to the lower A values in Fig. 4.18a for $\theta_i = 75°$ and following failure of the single scattering dynamics recovery. The crude

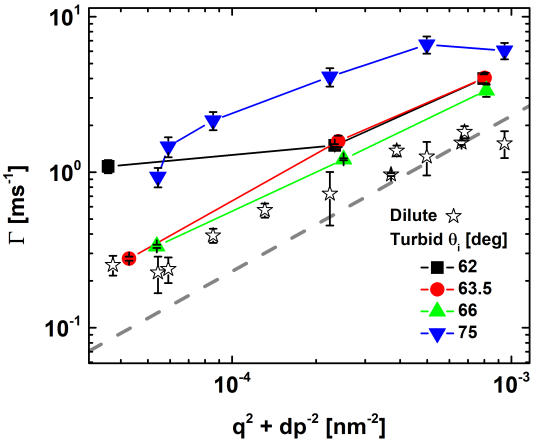

Figure 4.22: Early slope values from the near wall dilute case and values obtained from subtracting VH from VV correlograms taking into account the dynamic intensities. The star symbols refer to the near wall measurements in single scattering conditions (for why their values are faster than the bulk line please refer to the appendix 4.A.1). The slanted dashed line is the bulk dilute diffusive theoretical line which agrees with the dilute bulk measured values to within 10%.

attempt at subtracting the VH signal from the VV signal gave relatively good results of the same magnitude as the true near wall values (single scattering). Still, the turbid values tended to be faster in average, which is an indication of bulk diffusion and of multiple scattering.

4.5 EW-DLS velocimetry in a simple turbid fluid

Based on the Monte Carlo simulations and the previous section we expect to be able to separate the single scattering near wall signal from the bulk multiple scattering signal in shear flow experiments.

In this section we present the experimental results obtained through the implementation of EW-DLS velocimetry on a rheometer using the same setup as in chapter 3. To establish the principle of the approach, we used a simple Newtonian reference covering a broad range of turbidity. The samples consisted of PS latex spheres (2R=190nm) dispersed in a 77% glycerol and 23% water mixture. We varied the concentration of spheres dispersed in the fluid so l^* varied by almost two orders of magnitude around two different gap values (see Fig. 4.2).

4.5.1 Splitting of temporal decorrelation

We can get a quick impression of the what is obtained from EW-DLS velocimetry on turbid media from the shear rate ramp VV correlograms in Fig. 4.23. As the simulations predict we indeed observed two distinct modes. At low shear rates the measured overall correlograms seem pretty much the same as at no applied shear rate as we are probing diffusion. At 1 and 10 s^{-1} the upper or fast portion of the correlogram starts shifting towards shorter times leaving a slower small portion of the correlogram behind. As the shear rate is increased the split in the correlogram in terms of time and amplitude remain and become constant. The slower mode now has an oscillation resembling the one encountered during single scattering near wall velocimetry experiments. This oscillation goes below 0 indicating heterodyne conditions. Finally, both modes evolve

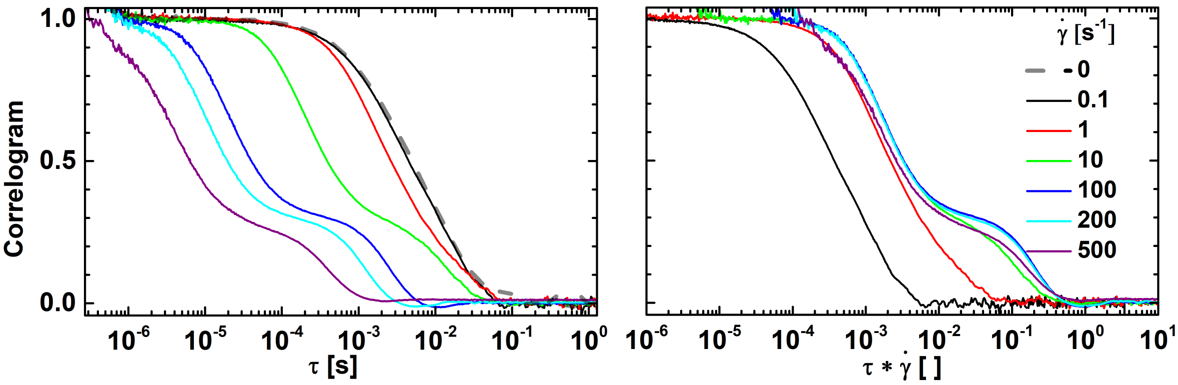

Figure 4.23: VV correlograms of 5% volume fraction ($l^* = 121\ \mu m$) with 450 μm gap. The correlograms were normalized by their respective amplitudes (~ 0.4). (right) Time axis rescaled by the nominal shear rate.

linearly with applied nominal shear rate as seen when their x-axis is rescaled by the shear rate and the lowest $\dot{\gamma}$ does not overlap with the rest as it is probing diffusion and not shear.

4.5.2 Polarization dependent dynamics

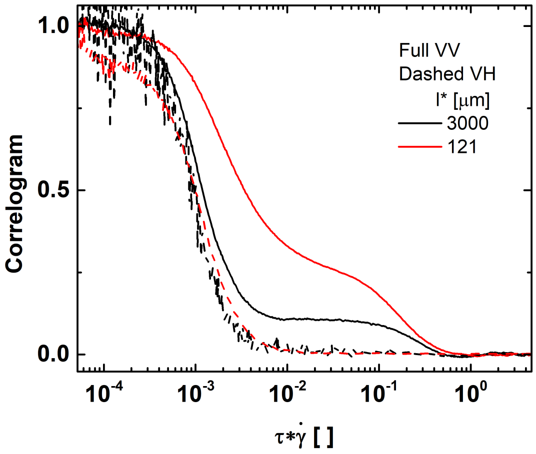

Figure 4.24: VV and VH comparison at 250 μm gap for 5 % and 0.2 % concentrations. Time axis rescaled by the nominal shear rate (100 s^{-1}). The correlograms were normalized by their respective amplitudes (~ 0.4).

The origin of the modes is reinforced by comparison of the VV and VH signals. We have seen that the VV signal possibly contains decoupled multiple scattering and single scattering near wall information. The VH signal should, by the nature of the incident polarization, contain no single scattering signal, which is strictly polarized as the incident beam for spherical tracers. Fig. 4.24 shows clearly how the slow mode is not present in the correlogram when measured in VH, leaving only the fast mode. This is in agreement with the simulation result.

4.5.3 VV slow mode: near wall velocities

We used Fourier transform analysis in the same way it was performed in chapter 3 to extract the cut-off velocity from the slow mode and utilize the same rescaling from frequency into length ($L_\omega = \omega/(\dot{\gamma} q_\parallel)$). In Fig. 4.25 the values for L_ω (3.2.2) are plotted vs volume fraction and shear rate. $L_\omega \sim Rh = 95$ nm as for stick boundary conditions indicating the signal is indeed near wall velocity. For low shear rates the values seemed to spread but became constant at sufficiently high shear rates (Pe$\approx$ 1).

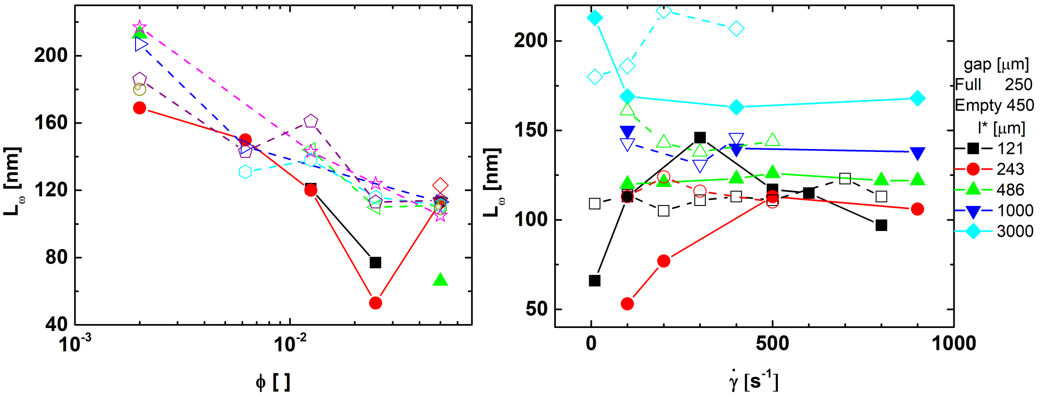

(a) (b)

Figure 4.25: Slow mode main frequency rescaled into units of length, L_ω. (a) Vs concentration, no legend is given for the different rates. (b) Vs nominal shear rate.

Comparing results for the different volume fraction ϕ, L_ω appeared to decrease as ϕ was increased. This could be due to the presence of low order scattering terms but could as well be related to different concentration profiles $\phi(z)$ as the concentration was varied. The particles are charged and increasing their concentration could alter $c(z)$ reducing L_ω. The variation in L_ω could also be related to the level of heterodyne. We were not able to obtain L_ω values for the 10% dispersion. We will address how this is related to the heterodyne level in few paragraphs.

With these results we can confidently state that VV EW-DLS velocimetry measurements in turbid media are still sensitive to near wall velocities with only a weak influence by the level of turbidity. The analysis developed for the single scattering and described in the previous chapter can be used to extract the near wall velocity ω.

4.5.4 Intensity

There is high probability of having contributions from slow or low order multiple scattering terms mixed with the near wall signal. In fact these could be responsible for the weak dependence of L_ω on ϕ.

In terms of total intensity the VV signal was up to an order of magnitude higher than the VH signal (Fig. 4.26) in the same way as the diffusion results (Fig. 4.16). The VH contribution appears to come closer to the VV at low values of l^* possibly approaching a strong DWS limit. Lastly we observe that both VV and VH intensities increase more than linearly with the particle concentration (in this regime $l^* \propto 1/\phi$) either as a consequence of glass surface scattering and stray light or of the multiple scattering probabilities being quite possibly non linear.

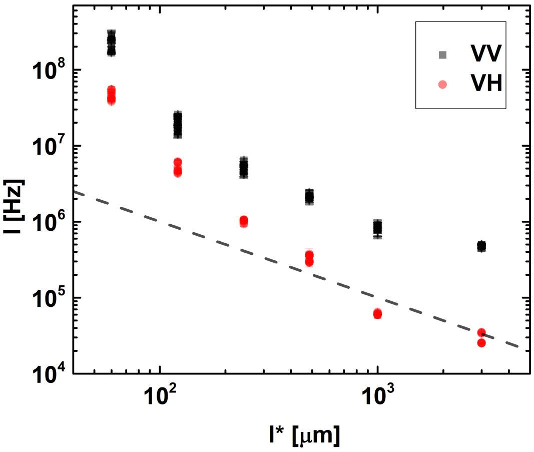

Figure 4.26: Total intensity vs l^*. All of the data are plotted together for different gaps and shear rates. The dashed line is a guide for the eye with slope of -1.

4.5.5 Signal mixing: homodyne or heterodyne

The VH correlogram is expected to be in homodyne mode as the static light from the glass is polarized there are no depolarized light sources in the samples. Differently the VV signal can be heterodyne given the presence of the VV static scattering from the glass. Typically the static intensity is of the order of 1 kHz (with some variation). The slow mode's dynamic intensity is plotted in Fig. 4.27. It varied almost linearly with concentration over 3 orders of magnitude for the concentration range used. At the lowest l^* of 60 μm (10% sample) the dynamic intensity was $\sim 10^7$ Hz, 10^4 times higher than the usual static intensity. Fig. 3.3 in chapter 3 shows how the even low levels of heterodyne ($A \sim 1$ or $I_{static} \ll I_{dynamic}$) can produce oscillations in the near wall velocimetry correlogram but the detectable limit lies at $I_{dynamic}/I_{static} \sim 10^3$. This explains why the 10% sample is lacking the oscillations necessary for measuring L_ω and the lower concentrations did contain them.

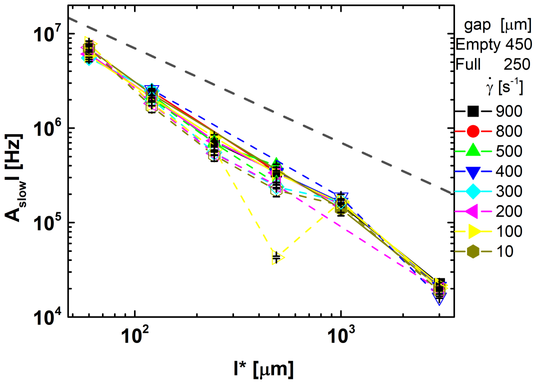

Figure 4.27: Dynamic intensity of the slow mode in VV vs l^*. The dynamic intensity is the product of the amplitude of the mode times the total intensity. The thick dash line has slope of -1.

As scattering increases the level of heterodyne decreases and the oscillations become less visible. The slow mode was therefore weakly heterodyne yet sufficiently so to measure L_ω. In case of purely homodyne measurement, the rate Γ can still be measured. It should be noted here that external heterodyne sources can be introduced to the system if wanted. For example one could mix a portion of the laser beam with the sample signal through two optical fibers coupled at the detector. This would simplify the analysis and the quantification of the near wall velocities.

The heterodyne also affects the fast bulk mode in the VV correlograms given the mixing with the slower near wall mode. This is shown in Fig. 4.28 where we have done a rough normalization of the correlograms to show the correspondence of VV to heterodyne (field correlation function) and VH to homodyne (intensity correlation function) by taking the square of the VV (field to intensity) and square root of the VH (intensity to field). The rough normalization did a fairly good job at making the VV and square root of VH and VH and square of VV to overlap.

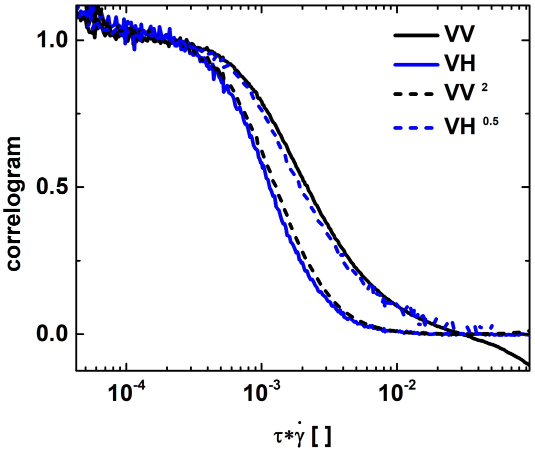

Figure 4.28: Full lines are the fast mode in VV and VH correlograms linearly normalized in the shown interval. Dashed lines correspond to the square of the VV and square root of the VH correlogram. Concentration = 5% PS, $l^* = 121\ \mu m$, gap = 250 μm.

4.5.6 Fast mode: bulk DWS

The shape of the DWS fast mode in the correlogram is often difficult to evaluate analytically [9, 10]. Traditional DWS velocimetry experiments for which solutions exist are performed on slab shaped samples with a wide beam illumination at normal incidence and detection either straight after the slab in “forward” or “transmission” geometry or from the same side as the light source but at a slight angle in “backscattering” geometry.

In our case we have an evanescent wave light source with $\boldsymbol{k_{EW}}$ lying parallel to the incident surface and with point-of-entrance detection [2]. We characterized the fast mode with a simple stretched exponential ($A \exp -(t/\tau)^{\beta}$) that quantifies the spread of the phase shift distribution and the characteristic time of the decay. We fitted directly the raw data without any normalization. This should not affect the VV values significantly (they are mostly heterodyne) and should at most require a factor of 0.5 in the VH's τ's.

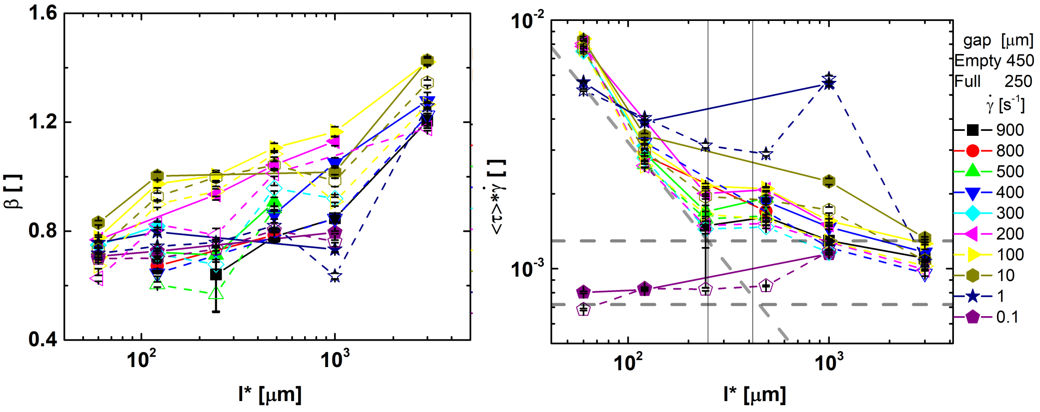

(a) (b)

Figure 4.29: Fast mode in the VV correlograms. The values correspond to fits of the raw data (homodyne). The figures share the same legend. (a) Stretch exponent β. (b) Average time of stretched exponential times the nominal shear rate. The vertical lines correspond to the two gaps used and the horizontal dashed lines correspond to the theoretical transmission prediction for the two gaps. The slant dashed line corresponds to the theoretical backscattering prediction.

In the traditional DWS under flow geometries the forward scattering has a $\beta = 2$ and for the backward scattering a $\beta = 1$ [10]. We found the fast mode in the VV signal was characterized by a slightly broad distribution with a $\beta \sim 0.8$ over the lower l^*'s (Fig. 4.29a). The distribution became more compressed at the higher l^*'s. As for the gap size, higher values have the same effect as shorter l^*'s. The change in β was small but shows that the photon path distributions does depend on l^* and the gap. The gap was the smallest length defining the available scattering volume and was also close to l^*.

Higher values of β, indicative of more compressed phase shift distributions can be rationalized as the gap acting like a filter whenever $l^* > gap$ and resulting in a narrower distribution at the detector.

Obtained values of the average decay time ($\langle\tau\rangle = (\tau/\beta)\, Gamma\,(1/\beta)$) [33] multiplied by the corresponding nominal shear rate for the VV are reported in Fig. 4.29b. Given $\beta \sim 1$, $\langle\tau\rangle \approx \tau$. For l^*'s smaller than the gaps (vertical lines in Fig. 4.29b) the characteristic times followed close to the theoretical prediction for the standard DWS backscattering velocimetry (slanted dashed line in Fig. 4.29b $= \sqrt{30}/(k_0 l^*)$). For values of l^* higher than the gap $\langle\tau\rangle$ becomes approximately constant, now close to the theoretical prediction for the standard DWS forward scattering velocimetry (horizontal dashed lines in Fig. 4.29b $= \sqrt{30}/(k_0 gap)$). It appears that the VV signal transitioned from backward to forward scattering like at $l^*/gap \approx 1$.

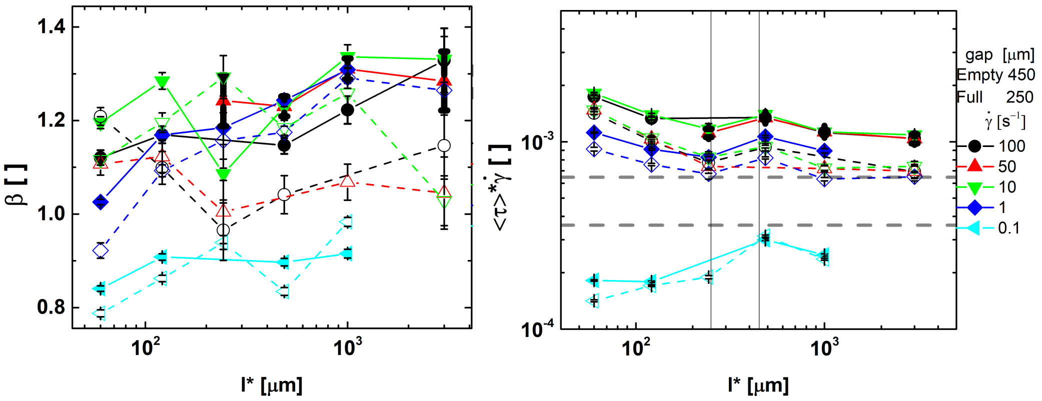

(a) (b)

Figure 4.30: Fast mode in the VH correlograms. The values correspond to fits of the raw data (homodyne). The figures share the same legend. (a) Stretch exponent β. (b) Average time of stretched exponential times the nominal shear rate. The vertical lines correspond to the two gaps used and the horizontal dashed lines correspond to the theoretical transmission prediction for the two gaps in homodyne conditions.

Values of β in Fig. 4.30a for the fast mode in the VH signal were approximately constant in l^* and closer to 1 than the VV counterparts. The characteristic times for the VH correlograms were approximately constant over all the range of l^* (Fig. 4.30b) differently from the VV case. $\langle\tau\rangle$ values are close to the theoretical prediction for the standard DWS forward scattering velocimetry (horizontal dashed lines in Fig. 4.30b).

It seems that the theoretical predictions for the standard DWS velocimetry can describe the recorded data in VV and VH to within a factor of 2. The VH case resembles the forward scattering case. The VV case has two regimes, the low l^*/gap which depends on $1/l^*$ like the backward scattering case and the high l^*/gap resembling the forward scattering case. We are therefore able to measure $\bar{\dot{\gamma}}$ over the gap.

The total internal reflection evanescent wave illumination and the point of entrance detection breaks the symmetry found in traditional DWS forward and back scattering experiments. These conditions should constrain the detected VH and high l^* VV photons to paths with number of random walk steps defined by the gap dimension ($(gap/l^*)^2$) to reach the detector as in the forward scattering case. For values of l^* lower than the gap, the backscattering behavior is recovered in the VV case. Probably photons become more likely to reach the detector without the gap size constraint.

4.6 EW-DLS velocimetry on concentrated hard spheres suspension

In this section, we apply the technique to dense suspension of hard spheres. The case of near wall slip in pure repulsive hard spheres has received some attention by Ballesta et al. [34]. They found that the index matching condition have a large effect on slip. Large slips were measured in case of index match (through hard sphere / hard wall behavior). When index matching was relaxed, then "stick" boundary conditions were observed. In general index matching is a requirement for microscopy techniques but this optical constraint can have strong effects on the slip of the sample.

4.6.1 Near glass transition

The measured correlograms are reported Fig. 4.32a, where the time axis has been rescaled by the applied shear rate. The slow decay part was analyzed through the FFT methods and L_ω was deduced. The fast decay was fitted by stretch exponential in order to deduce an “optical” bulk shear rate.

We introduce here an average optical shear rate according to $optical\ \dot{\gamma} = \Gamma\sqrt{30}/(k_0 d)$ where Γ is the decay rate of the fast bulk mode and d is the relevant length scale. We have used here $d = gap$ as we showed before that the shortest one of the two is the

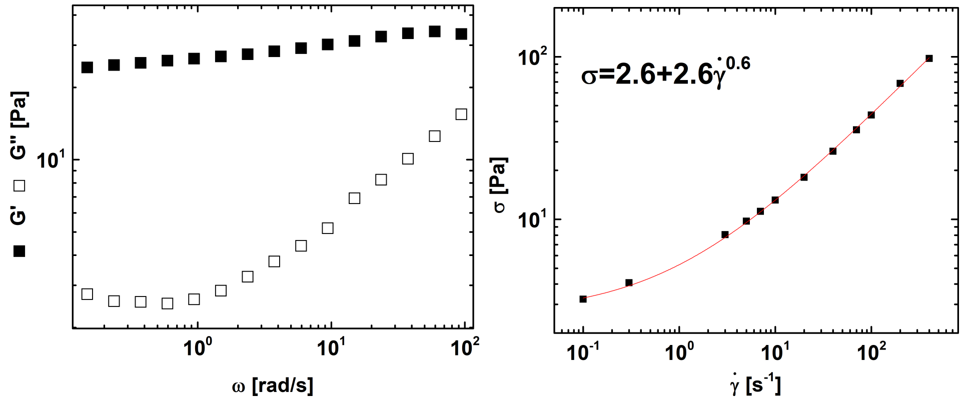

(a) (b)

Figure 4.31: 57% 214 nm PMMA HS in dodecane. (a) Linear rheology. (b) Flow curve measured together with the velocimetry.

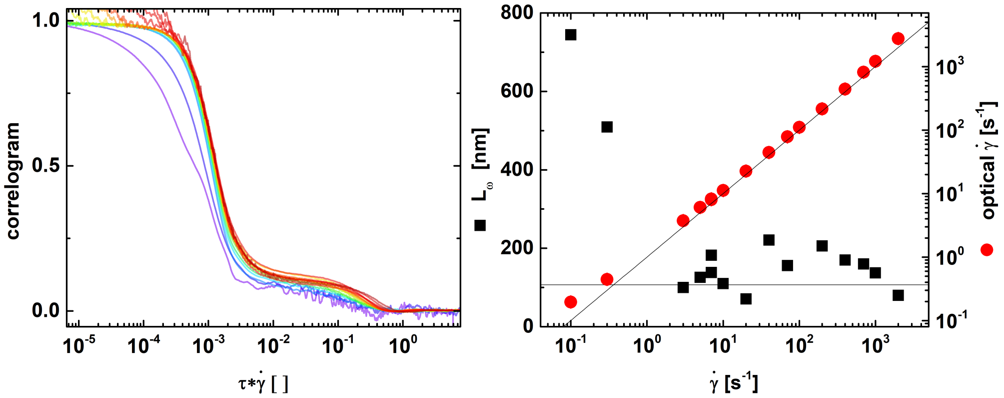

(a) (b)

Figure 4.32: 57% 214 nm PMMA HS in dodecane. (a) Correlograms normalized by the amplitude. (b) Near wall L_ω from the slow mode and bulk shear rate derived from the fast multiple scattering decay.

relevant one (l^* grows strongly for concentrated systems and becomes higher than the *gap*). In Fig. 4.32b we show how the shear rate measured by optical means is to within a numerical factor aligned with the nominal shear rate as per the stick boundary conditions determined from the near wall mode. The measured L_ω are also displayed in Fig. 4.32b. They are compatible with stick boundary conditions to within our resolution.

4.6.2 Repulsive glass

Here we use a non index matched system in contrast to the ones used in [34]. The measured flow curve in Fig. 4.33b is in agreement with the cited work. Though unlike them we find that slip is still present and of the order of 1 μm. This magnitude of slip is inconsequential in rheological measurements where the gap is typically 100's of micrometers. It is also difficult to detect by confocal particle tracking.

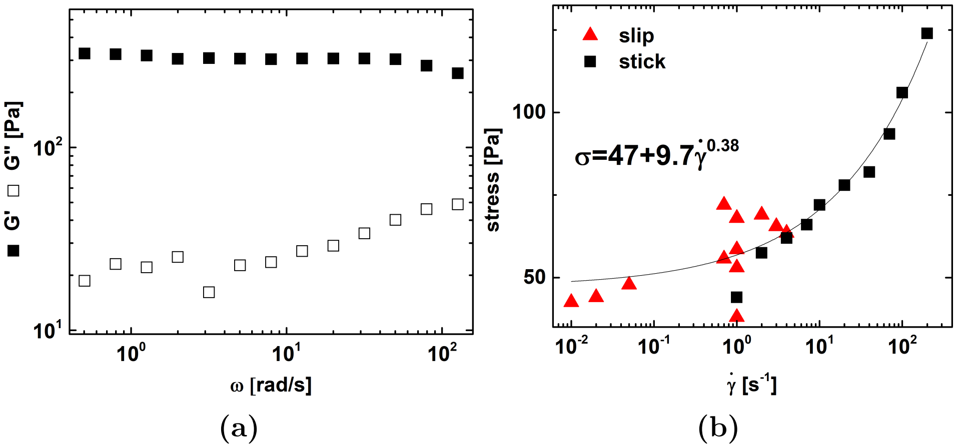

(a) (b)

Figure 4.33: 60% 214 nm PMMA HS in dodecane. (a) Linear rheology. (b) Flow curve measured together with the velocimetry.

Transient

The strong scattering signals available in concentrated turbid media permit the recording of correlograms over short periods of time (seconds). We took snapshots of the recovery after yielding at high shear rate. Fig. 4.34a shows the chronology of the applied shear rate with shaded areas of matching color to the recorded correlograms shown in Fig. 4.34b.

The initial yielded glass presents stick boundary conditions as seen from the slow mode. The near wall velocity increases as the stress slowly builds up while imposing low shear rates. At ∼65 Pa the stress becomes unstable as the material yields and the near wall velocity which was a few percentages of the top plate starts dropping towards the stick boundary values.

The values extracted from the transient are plotted together in Fig. 4.35. The optical shear rate follows the nominal shear rate as the effect of the slip is negligible. The amplitude of the fast mode evolves along the measurement, but is not clear to us why it does. We can name two possibilities: It is a result of a different flow profile,

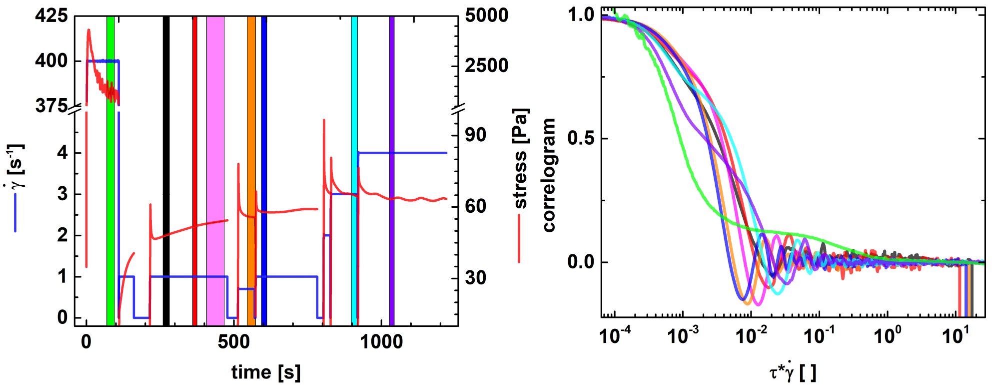

(a) (b)

Figure 4.34: 60% repulsive glass. (a) Time evolution of nominal shear rate and stress. (b) Correlograms recorded during the shaded intervals in 4.34a with matching colors.

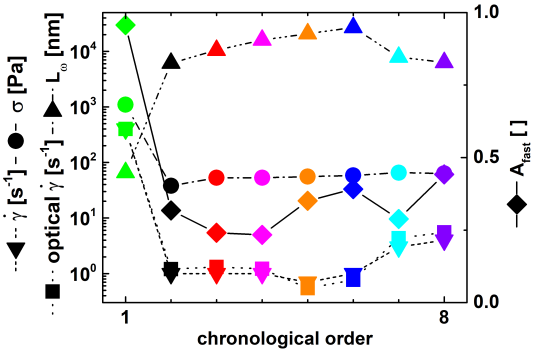

Figure 4.35: 60% repulsive glass. Values relative to the transient.

possibly banding, but we have not proven that so far. Alternatively it could be a result of a change of relevant length scale, in particular of l^* as a result of flow induced positional correlations.

4.6.3 Attractive glasses

The attractive glass case is more difficult to measure rheologically and is not fully solved [35]. Measurement by confocal microscopy is quite challenging [36]. Here we report only preliminary results that show the complex evolution of slip. We are not capable yet to interpret the measured correlograms.

As can be seen from Fig. 4.36 the correlograms were quite rich and diverse. While the highest shear rate present stick boundary conditions as previously seen the lower rate presented differences in the fast mode as well as in the near wall velocity. The lower

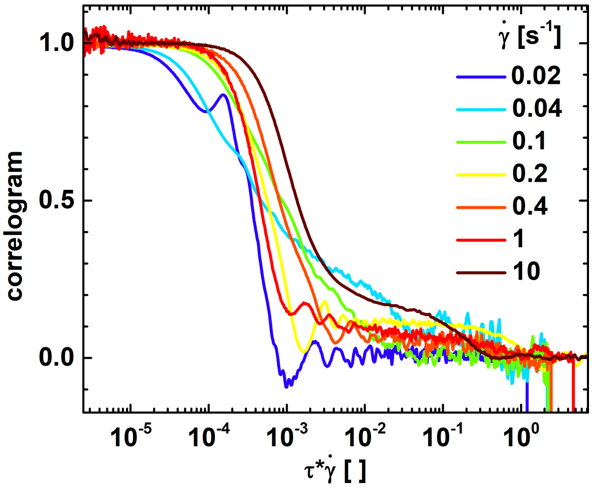

Figure 4.36: Correlograms for the attractive glass.

rates contained oscillations in the early decay. This has been seen from explorative simulations to be due to strong banding within the sample.

4.7 Dynamics in the "forbidden" region

The refraction law implies there is an angular zone where no scattered light is expected to propagate, the "forbidden" region (see 4.2.1). However simple observation shows that light can be detected there. The question then arises of how this light is produced and subsequently whether measurements in this zone could provide any information on the specific of the sample, as it is easy to detect, and measure good correlation functions.

Different origins are possible. The existence of light tunneling from optical probes into the "forbidden" angular domain is used for "tunnel" near-field optical microscopies [37, 38]. Potenza et al. [39] proposed that for TIR experiments on colloidal systems light can tunnel back into the "forbidden" region of the optically denser medium when the scatterer is in close proximity to the interface. The probability of tunneling is low so light in this region is mostly singly scattered. Other possibilities relate to "imperfections" of the interface scattering, i.e beyond Fresnel and Born approximations [32]. Scattering by rough surfaces is a complex process. It has receive some attention, especially in the case of X-ray but also in the case of light. We do not intend do dwell much in that direction. We just try to establish some phenomenology of the forbidden zone scattering with the hope that it may be of near wall origin. In that case the measured dynamics should relate to the near wall motion. It would then provide an alternative way to probe near wall dynamics.

Note that our MC simulations are not applicable in the forbidden region as they are do not include the proper electrodynamics.

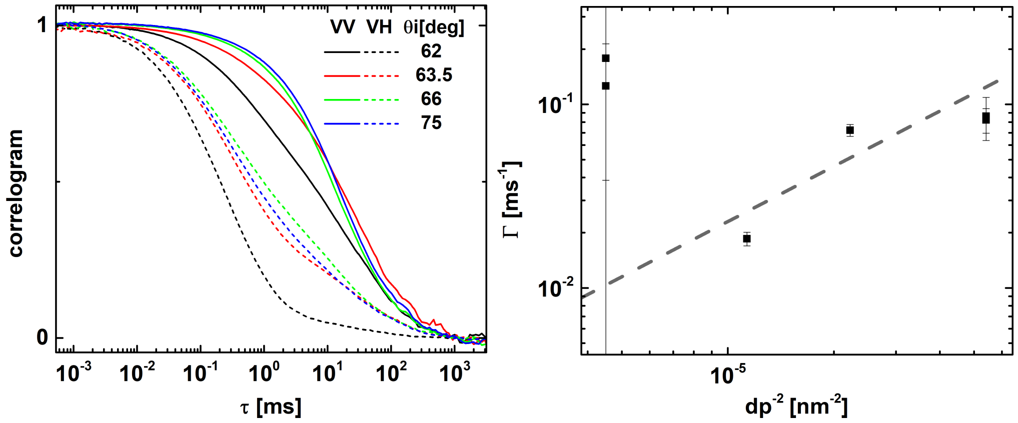

(a) (b)

Figure 4.37: Dynamics in the forbidden region. (a) VV and VH correlograms. (b) Decay times of the slow mode in the VH correlograms obtained by a stretched exponential fit. The dashed line is the theoretical bulk rate.

We could observe intensity (Fig. 4.38) and dynamics in the forbidden region for the 10% 190 nm PS spheres in water. The dilute sample’s intensity in the forbidden region was too low to make measurements practical. A few correlograms are plotted in Fig. 4.37a. The VV signal slowed down continuously as θ_d approached the critical angle and later became constant though stretched. The VH signal also slowed down continuously but at the critical angle a second slower mode appear which coincides with the decay in the VV signal.

The VV and the VH slow mode appear to share the same dynamics. We show in Fig. 4.37b the values extracted from a two stretched exponential fit of the VH signal, as it is more convenient to fit. The values are plotted vs *dp* as a plausible choice of relevant length scale.

There is no reason to expect an effect from the backreflection so we can compare the results with the bulk theoretical values (excluding of course hydrodynamic slowdowns). If the signal is of tunneling nature then the length scale will be be reflection invariant and if the signal is a result of full backward scattering then its intensity should be 10 times lower than in the allowed region (Fig. 4.38).

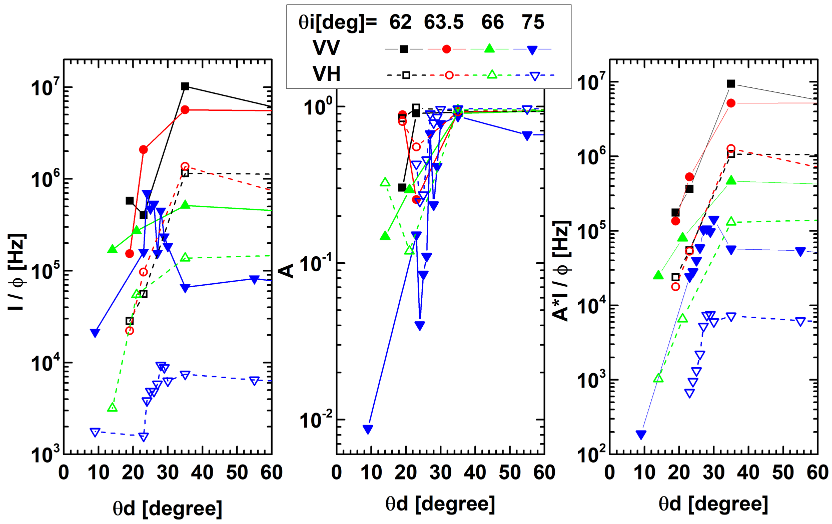

Figure 4.38: Forbidden region

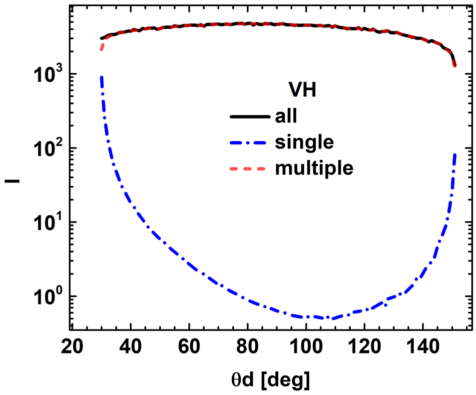

Figure 4.39: MC simulated intensity for the VH signal.

The intensity data is shown in Fig. 4.38. Going into the forbidden region the detected dynamic intensities *AI* drop fast with θ_d. They roughly preserve the θ_i dependence and the ratio of VV to VH. In particular, the dynamic amplitude *A* also falls quickly perhaps in support of tunneling arguments.

From the MC simulations for the forward scattering in Fig. 4.39 we find that half of the intensity could potentially come from the single scattering. The simulation result is given by volume effects like finite size of the scattering volume and acceptance angle of the optical fiber. This parameters are certainly more relaxed in experimental conditions so the simulation curve can be taken into account.

We cannot support whether there should be any VH intensity or not for the tunneling argument. Certainly it is possible that some of the VV signal went into the VH due to alignment imperfections. Further work and specially theoretical support is necessary to understand the motion probed and most importantly the pathway by which the light is detected in the forbidden region.

4.8 Conclusions

We have investigated the use of evanescent wave dynamic light scattering with point-of-entrance detection on turbid media. With the aim to recover the single scattering dynamics from the multiple scattering signal. We have shown with ray tracing simulations that the single scattering dynamic information is at reach with the used geometry. Using a 2-goniometer setup and a turbid colloidal dispersion we were able to recover a quasi single scattering correlation function and the near wall dynamics by using a linear combination of the VV and VH signals. This has potential application to simplify sizing of particles within turbid samples without knowledge of l^*. Application of EWDLS for velocimetry on a rheometer to turbid media was most advantageous. The single scattering near wall velocity information decouples in the frequency domain from the multiple scattering signal allowing for the clear distinction between the two in the case of a linear shear profile. Moreover the multiple scattering information relates to the bulk dynamics in a similar way as traditional DWS velocimetry making for contemporary measurement of the near wall boundary condition and the bulk shear rate. We also reported dynamics from the forbidden region with times comparable to the diffusion though it is not clear how the signal would come to be.

The technique still has untapped potential. Use of an external heterodyne source would simplify analysis and improve sensitivity to the near wall velocities. With aid of the simulations it should be possible to fit data with a flow profile given known optical properties similarly as done in [18] though with the advantage of the extra near wall information. Preliminary experiments under oscillatory measurements (see Fig. 4.40) show possible applicability to oscillatory measurements with echo [40, 41] like results at low amplitudes and bulk velocities that scale in a Cox-Merz [42] fashion with the continuous flow counterpart.

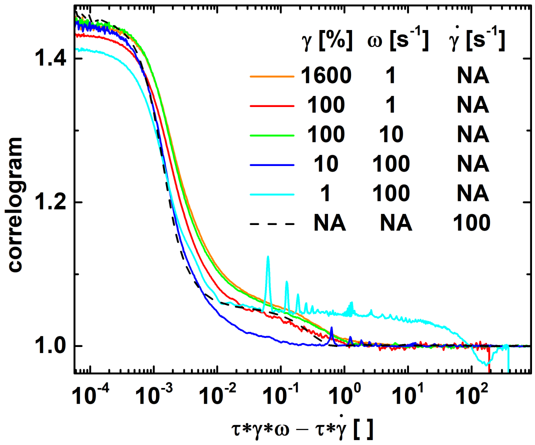

Figure 4.40: VV correlogram under oscillatory shear for the 57% PMMA sample. The time axis was rescaled with the strain amplitude and the frequency. One continuous flow curve is plotted for comparison (time axis scaled with the shear rate). At all strains the fast bulk mode overlap to some extent. At the lower strains the slow mode resembles echo measurements [40, 41]. At the higher strains the slow mode is comparable to the near wall under continuous flow.

4.9 Acknowledgements

We thank the following people for their contributions. E. Moghimi for taking care of preparing the concentrated PMMA spheres dispersions and sharing much of his knowledge and expertise. J. C. Ramella-Roman for making the MC Polarized Mie scattering code used in the simulations freely available on the web. Malvern for the Malvern Kinexus.

4.A Appendix

4.A.1 TIR EW-DLS and back reflection

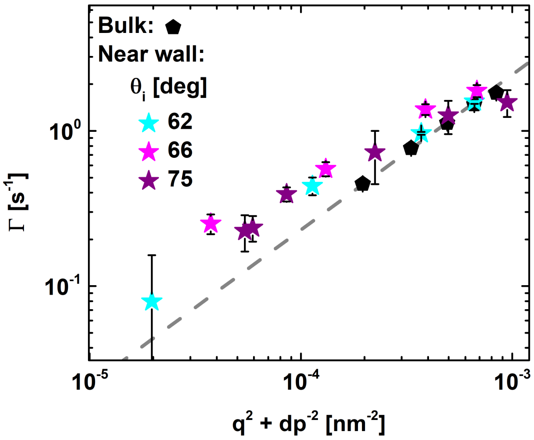

Figure 4.41: Single scattering early slope values (dilute 2.7 10^{-3}%) from bulk DLS measurements and near wall EW-DLS measurements. Different penetration depths were used for the near wall measurements. Plotted vs $q^2 + dp^{-2}$. The slanted dashed line is the bulk dilute diffusive theoretical line.

Given the cylindrical geometry of the lens, non anti-reflection coated lenses have backreflections originating from the lens-air interface that can be mixed in with the detected signal or even be mistaken for it [1]. The result of the backreflections is faster dynamics at small q's and slower dynamics at high q's. The effect is eliminated normal detection as light scattered from both reflections share the same $\boldsymbol{q}$ value.

We are aware of the presence of the backreflection in our measurements. Fig. 4.41 shows the characteristic decay rate of the correlograms from single scattering bulk DLS measurements obtained from early slope analysis. The bulk values agree to within 10% of the predicted value (dashed line in Fig. 4.41). The single scattering near wall early slopes should be lower than the bulk values given the hydrodynamic slowdown from the wall proximity [1] but we see faster dynamics given the backreflection signal. The results agree at 90° scattering ($q^2 \sim 5\ 10^{-4}$ nm^{-2}) where the effect is also canceled by symmetry.

Our measurements contained main and backreflection single scattering terms as well as multiple scattering main and multiple scattering backreflection contributions.

Bibliography

[1] Y. Liu, N. Claes, B. Trepka, S. Bals, and P. R. Lang, “A combined 3D and 2D light scattering study on aqueous colloidal model systems with tunable interactions,” *Soft Matter*, vol. 12, pp. 8485–8494, oct 2016.

[2] E. Vitkin, V. Turzhitsky, L. Qiu, L. Guo, I. Itzkan, E. B. Hanlon, and L. T. Perelman, “Photon diffusion near the point-of-entry in anisotropically scattering turbid media,” *Nature Communications*, vol. 2, p. 587, sep 2011.

[3] K. M. Yoo, F. Liu, and R. R. Alfano, “When does the diffusion approximation fail to describe photon transport in random media?,” *Physical Review Letters*, vol. 64, pp. 2647–2650, may 1990.

[4] Z. Fahimi, F. J. Aangenendt, P. Voudouris, J. Mattsson, and H. M. Wyss, “Diffusing-wave spectroscopy in a standard dynamic light scattering setup,” *Physical Review E*, vol. 96, p. 062611, dec 2017.

[5] L. F. Rojas-Ochoa, S. Romer, F. Scheffold, and P. Schurtenberger, “Diffusing wave spectroscopy and small-angle neutron scattering from concentrated colloidal suspensions,” *Physical Review E*, vol. 65, p. 051403, may 2002.

[6] K. Schätzel, “Suppression of Multiple Scattering by Photon Cross-correlation Techniques,” *Journal of Modern Optics*, vol. 38, pp. 1849–1865, sep 1991.

[7] P. Segrè, W. Van Megen, P. Pusey, K. Schätzel, and W. Peters, “Two-colour Dynamic Light Scattering,” *Journal of Modern Optics*, vol. 42, pp. 1929–1952, sep 1995.

[8] D. Weitz and D. Pine, “Diffusing-wave spectroscopy,” in *Dynamic Light Scattering* (W. Brown, ed.), ch. Diffusing-, pp. 652–720, Oxford University Press, 1993.

[9] X.-L. Wu, D. J. Pine, P. M. Chaikin, J. S. Huang, and D. A. Weitz, “Diffusing-wave spectroscopy in a shear flow,” *Journal of the Optical Society of America B*, vol. 7, p. 15, jan 1990.

[10] D. Bicout, E. Akkermans, and R. Maynard, “Dynamical correlations for multiple light scattering in laminar flow,” *Journal de Physique I*, vol. 1, pp. 471–491, apr 1991.

[11] A. Raudsepp, *A Rheo-Optic Study of Wormlike Micelles Solutions*. PhD thesis, Victoria University of Wellington, 2009.

[12] B. Loppinet, J. K. G. Dhont, and P. Lang, “Near-field laser Doppler velocimetry measures near-wall velocities,” *European Physcal Journal E*, vol. 35, jul 2012.

[13] S. Kalinin, R. Kühnemuth, H. Vardanyan, and C. A. M. Seidel, "Note: A 4 ns hardware photon correlator based on a general-purpose field-programmable gate array development board implemented in a compact setup for fluorescence correlation spectroscopy," *Review of Scientific Instruments*, vol. 83, p. 096105, sep 2012.

[14] J. K. Percus and G. J. Yevick, "Analysis of Classical Statistical Mechanics by Means of Collective Coordinates," *Physical Review*, vol. 110, apr 1958.

[15] "LS Instruments: Scattering length calculator for Mie spheres, http://intranet.lsinstruments.ch:8080/lstar/lstar.php."

[16] N. Koumakis, A. Pamvouxoglou, A. S. Poulos, and G. Petekidis, "Direct comparison of the rheology of model hard and soft particle glasses," *Soft Matter*, vol. 8, p. 4271, mar 2012.

[17] G. J. Fleer and R. Tuinier, "Analytical phase diagram for colloid-polymer mixtures," *Physical Review E*, vol. 76, p. 041802, oct 2007.

[18] A. Raudsepp, P. Callaghan, and Y. Hemar, "A study of the nonlinear rheology of complex fluids using diffusing wave spectroscopy," *Journal of Rheology*, vol. 52, pp. 1113–1129, sep 2008.

[19] L. Wang, S. L. Jacques, and L. Zheng, "MCML-Monte Carlo modeling of light transport in multi-layered tissues," *Computer Methods and Programs in Biomedicine*, vol. 47, pp. 131–146, jul 1995.

[20] Q. Fang and D. A. Boas, "Monte Carlo Simulation of Photon Migration in 3D Turbid Media Accelerated by Graphics Processing Units," *Optics Express*, vol. 17, p. 20178, oct 2009.

[21] J. Ramella-Roman, "Polarized Light Monte Carlo, https://omlc.org/software/polarization/index.html."

[22] J. Vince, *Quaternions for Computer Graphics*. London: Springer London, 2011.

[23] J. C. Ramella-Roman, S. A. Prahl, and S. L. Jacques, "Three Monte Carlo programs of polarized light transport into scattering media: part I," *Optics Express*, vol. 13, p. 4420, jun 2005.

[24] J. C. Ramella-Roman, S. A. Prahl, and S. L. Jacques, "Three Monte Carlo programs of polarized light transport into scattering media: part II," *Optics Express*, vol. 13, 2005.

[25] J.-J. Gil and R. Ossikovski, *Polarized Light and the Mueller Matrix Approach*. CRC Press, 2016.

[26] W. W. Hergert and T. Wriedt, *The Mie theory : basics and applications*. Springer, 2012.

[27] S. Prahl, "Monte Carlo Light Scattering Programs, https://omlc.org/software/mc/."

[28] S. L. Jacques and L. Wang, "Monte Carlo Modeling of Light Transport in Tissues," in *Optical-Thermal Response of Laser-Irradiated Tissue*, pp. 73–100, Boston, MA: Springer US, 1995.

[29] X. Ben, H.-L. Yi, and H.-P. Tan, "Polarized radiative transfer considering thermal emission in semitransparent media," *Chinese Physics B*, vol. 23, p. 099501, sep 2014.

[30] D. A. Weitz, J. X. Zhu, D. J. Durian, H. Gang, and D. J. Pine, "Diffusing-wave spectroscopy: The technique and some applications," *Physica Scripta*, vol. T49B, pp. 610–621, 1993.

[31] E. Filippidi, V. Michailidou, B. Loppinet, J. Rühe, and G. Fytas, "Brownian diffusion close to a polymer brush," *Langmuir*, vol. 23, no. 9, pp. 5139–5142, 2007.

[32] A. K. González-Alcalde, J.-P. Banon, Ø. S. Hetland, A. A. Maradudin, E. R. Méndez, T. Nordam, and I. Simonsen, "Experimental and numerical studies of the scattering of light from a two-dimensional randomly rough interface in the presence of total internal reflection: optical Yoneda peaks," *Optics Express*, vol. 24, p. 25995, nov 2016.

[33] I. S. I. S. Gradshteiin, I. M. I. M. Ryzhik, A. Jeffrey, and D. Zwillinger, *Table of integrals, series and products.* Academic Press, 2007.

[34] P. Ballesta, G. Petekidis, L. Isa, W. C. K. Poon, and R. Besseling, "Wall slip and flow of concentrated hard-sphere colloidal suspensions," *Journal of Rheology*, vol. 56, pp. 1005–1037, sep 2012.

[35] P. Ballesta, N. Koumakis, R. Besseling, W. C. K. Poon, and G. Petekidis, "Slip of gels in colloid-polymer mixtures under shear," *Soft Matter*, vol. 9, no. 12, p. 3237, 2013.

[36] N. Park, E. J. Umanzor, and J. C. Conrad, "Aqueous Colloid + Polymer Depletion System for Confocal Microscopy and Rheology," *Frontiers in Physics*, vol. 6, p. 42, may 2018.

[37] B. Hecht, D. Pohl, H. Heinzelmann, and L. Novotny, "âĂIJTunnelâĂİ near-field optical microscopy: TNOM-2," *Ultramicroscopy*, vol. 61, pp. 99–104, dec 1995.

[38] L. Novotny and B. Hecht, *Principles of Nano-Optics.* Cambridge: Cambridge University Press, 2006.

[39] M. A. C. Potenza, D. Brogioli, and M. Giglio, "Total internal reflection scattering," *Applied Physics Letters*, vol. 85, pp. 2730–2732, oct 2004.

[40] P. Hébraud, F. Lequeux, J. P. Munch, and D. J. Pine, "Yielding and Rearrangements in Disordered Emulsions," *Physical Review Letters*, vol. 78, pp. 4657–4660, jun 1997.

[41] G. Petekidis, P. Pusey, A. MoussaÄśÌĹd, S. Egelhaaf, and W. Poon, “Shear-induced yielding and ordering in concentrated particle suspensions,” *Physica A: Statistical Mechanics and its Applications*, vol. 306, pp. 334–342, apr 2002.

[42] E. Cox, W.P. and Merz, “Correlation of Dynamic and Steady Flow Viscosities,” *Journal of Polymer Science*, vol. 28, no. 118, pp. 619–622, 1958.

Chapter 5

Ellipsometry of turbid media

5.1 Introduction

Turbid dispersions are often made of one medium dispersed in a transparent fluid. The turbidity arises from the difference in refractive index of the two constituents, and the characteristic sizes of the dispersion. Typical examples are milk (fat globules dispersed in water) or colloidal dispersion. The characterization of such dispersions by optical means of (determining the composition and or the characteristic size of the dispersed phase) is made difficult by the lack of propagation of the light in the medium.

The proper description of the clear-turbid interface is not fully established. Different models mostly semi-empirical have been produced, but they don't fully agree. An approach to measure absorption cross section of strongly absorbing samples is to use attenuated total reflection (ATR). Under total internal reflection only a small part of the sample is penetrated by the beam. It is equivalent to doing experiments with very thins sample (of the order of the light wavelength). Spectroscopic ATR in the visible range has been proposed [1] to characterize turbid dispersion but not used so much. Other related approach has been to measure the angular dependent reflectivity around the critical angle [1, 2, 3, 4]. The measurement is relatively straightforward, but the analysis/interpretation of the data are somewhat model dependent.

Simpler models attempt to describe the reflection coefficient using some effective medium approximation. Here we report on internal variable angle spectroscopic ellipsometry to characterize turbid medium. The merit of effective medium approximation based models is evaluated. In the case of PS latex dispersion we found that an EMA description of the refractive index, where the real part is described by a mixing law, and the imaginary part is accounted for by the optical losses through Mie scattering, provide good representation of the internal VASE data.

5.1.1 VASE

Ellipsometry is a widely used optical technique for characterization of materials and interfaces. It relies on the measurement of the polarization dependent reflection coefficient and its relation to refractive index distribution at the interface(s). The Variable Angle Spectroscopic Ellipsometry represents the state-of-the-art development in the commercially available ellipsometers. They offer the possibility of a variable incident angle and of the wavelength dependence of the ellipsometric ratio. Variants are often available including full polarization characterization using Mueller matrices. Analysis software are also available that through modeling and fitting allows to extract the optical parameter of interest (typically thickness, wavelength dependent refractive index, composition, ...). Most of ellipsometry applications are dedicated to surface or thin film characterization, and use external reflection geometry where the incoming light access the surface under study through the air (or the vacuum) often referred as ambient. Alternatively internal reflection ellipsometry is also possible, where the incoming light accesses the interface of interest through a transparent substrate (mostly glass).

Internal reflection provides an efficient way to avoid light transmission through absorbing or scattering medium that will make the external reflectivity or ellipsometry measurements difficult. Therefore it is mostly used for the characterization of surface in contact with liquids, often in a "sensing" approach. A specific variant, known as TIR Ellipsometry [5] makes use of a thin metal film in between the substrate and the sample to take advantage of the enhanced sensitivity due to the plasmon resonance of the metallic layer. Internal reflection is the traditional geometry for refractometry, i.e techniques dedicated to the measure of refractive index of medium, as in Abbe refractometer. There, the refractive index of a substance is deduced from a precise measurement of the critical angle for total internal reflection.

The case of turbid materials As mentioned above, the case of the reflectivity between a transparent substrate and a turbid medium is of interest as it could be used to characterize the turbid medium and provide a way to estimate size and refractive index. Various effective medium approaches have been used to compute the reflectivity coefficient of these interfaces, mostly in the context of reflectivity measurements and the occurrence of total internal reflection, for refractometry application [6, 7].

Somewhat surprisingly the potentials of the wavelength dependence for characterization of turbid material do not seem to have been much investigated, neither the ones of ellipsometry. Here we show that VASE can be used to measure turbid samples, varying both the incidence angle and the wavelength. In particular we show the value of the wavelength dependence for determining the scattering losses. We propose an easy-to-implement (that should be easily implementable within ellipsometry package) fitting analysis of the VASE data based on EMA, that returns the characteristics of the turbid medium refractive index and losses. (Applied to model polystyrene latex in water as well as high fat content milk.)

5.2 Clear-turbid internal reflection

5.2.1 Reflectivity of lossy materials, ATR

Refractive index description of lossy material

Refractive index and polarizability are quantities that govern the propagation of light into media. In the case of transparent dielectric material, the dielectric constant is essentially a real number and the refractive index is well described by a real number. In the case of absorbing or more generally dissipating lossy materials, the dielectric constant is a complex number as an imaginary part of the polarizability has to be considered. Similarly the refractive index is a complex number with a real part n' and an imaginary part n''.

$$n' + in'' = (\epsilon + i\epsilon'')^{1/2} \tag{5.1}$$

A specific case of optical losses is observed when strong scattering is present. Scattering losses do not originate from absorption i.e a finite value of ϵ'' but rather from heterogeneities in ϵ'. The photons are not absorbed but merely change direction (and as such there is no loss). However, if one is interested in transmission or reflection coefficient, they appear lower than in transparent non absorbing medium and the experiments can be described by losses accounted for by an imaginary part of the refractive index n''. The relation between n'' and the heterogeneities in ϵ' has long been discussed and several attempts to establish it by scattering theories. In particular, in the case of Rayleigh or Mie scattering, the scattering cross section is estimated and can be expressed in term of losses per unit length $1/l$. The medium transmission as $T = \exp(-d/l)$ in equivalent to the absorbing medium case where the Beer Lambert law is used, $T = \exp(-d\alpha)$ where α is the absorbance.

Reflection coefficient

We are interested in the case of reflection between a transparent substrate and a turbid medium. Snell law and Fresnel coefficient provide the description of reflection and transmission at interface between two medium as obtained from continuity of fields at interfaces as derived from Maxwell laws. The Snell law gives

$$n_1 \sin(\theta_1) = n_2 \sin(\theta_2) \tag{5.2}$$

and the reflection coefficients are

$$r_s = \frac{n_1 \cos(\theta_1) - n_2 \cos(\theta_2)}{n_1 \cos(\theta_1) + n_2 \cos(\theta_2)} \;,\quad r_p = \frac{n_2 \cos(\theta_1) - n_1 \cos(\theta_2)}{n_2 \cos(\theta_1) + n_1 \cos(\theta_2)} \tag{5.3}$$

Eqs. 5.3 are valid for both real and complex numbers. In the case of purely dielectric medium refractive index is represented by a real number. In the case of lossy material n_1, n_2 can be complex number. In our case of interest where n_2 is complex, the relations become somewhat formal as θ_2 becomes a complex number. Ellipsometry is primarily concerned with the ratio r_p/r_s which in the most general case is a complex number, where the amplitude $\tan\Psi$ is the ratio of the p and s reflectivity and the phase Δ is the s-p phase shift.

$$\frac{r_p}{r_s} = \tan\Psi \exp(i\Delta) \tag{5.4}$$

The case of (attenuated) total internal reflection

In the case of no losses and when $n_1 > n_2$, total internal reflection can be reached at incidence angle $\theta > \theta_c$ where the critical angle θ_c is given by $\sin(\theta_c) = n_2/n_1$. Formally under total internal reflection, the angle θ_2 becomes imaginary, describing the strongly decaying near field evanescent wave. The reflectivity coefficient takes the form $r_s = (q_1 - i\kappa)/(q_1 + i\kappa)$. Both $q_1 = n_1 \cos(\theta_1)$ and $\kappa = \sqrt{n_1^2 \sin(\theta_1)^2 - n_2^2}$ are real and therefore $|r_s| = 1$. Similarly $r_p = -(q_1/n_1 - i\kappa/n_2)/(q_1/n_1 + i\kappa/n_2)$ and $|r_p| = 1$. The phase shift angle δ_s and δ_p follow relations $\tan(\delta_s/2) = \kappa/q_1$ and $\tan(\delta_p/2) = q_1 n_2^2/\kappa n_1^2$. The s-p phase shift $\Delta = \delta_p - \delta_s$ at TIR is directly related to the ratio of refractive index, as:

$$\tan\left(\frac{\Delta}{2}\right) = \frac{1 + \left(\frac{\kappa}{q_1}\frac{n_1}{n_2}\right)^2}{\frac{\kappa}{q_1}\left(\left(\frac{n_1}{n_2}\right)^2 - 1\right)} \tag{5.5}$$

and can be used for refractometry. It is however not extremely sensitive.

In TIR regime, the light does not propagate in medium 2 but penetrates it through the so called evanescent wave, with a penetration depth $1/dp = k\kappa$, $k = 2\pi/\lambda$ being the wave vector amplitude in vacuum. If medium 2 presents optical losses, n_2 is complex and the reflection coefficient are modified. The regime at $\theta > \theta_c = \arcsin\left(Re(n_2)/n_1\right)$, becomes an attenuated total reflection (ATR) as the reflectivity's amplitude are less than one. Formally κ becomes complex and the reflectivity coefficient takes the form, $r_s = (q_1 - \kappa'' - i\kappa')/(q_1 + \kappa'' + i\kappa')$. As a consequence $|r_s|< 1$.

In the case of small losses $n'' \ll n'$, $|r|\sim 1 - \epsilon$ and $-\log(r) \sim 1 - r \sim n''$. This is used in ATR spectroscopy [8]. Therefore measuring ATR reflectivity provides a way to measure n''. ATR is mostly used to measure the spectroscopic, i.e. wavelength dependence of absorption coefficient, known as ATR spectroscopy (mostly combined with Fourier transform infra-red spectroscopy) [9, 8, 10]. It is concerned by measuring the absorbance α (or n'') as a function of wavelength using internal reflection. Using Beer-Lambert's law and the scattering length l, $1/l = \sigma c$ where c is the number concentration and σ the scattering cross section one gets:

$$-\log(R) = \alpha d_e = 2kn''d_e = \sigma c d_e \tag{5.6}$$

d_e is a length scale associated with the TIR and α is the absorbance as it would be measured in transmission experiments. d_e is proportional to the penetration depth dp, but also has a polarization dependent geometrical factor to account for the intensity at the interface though the difference can be small for low contrast interfaces [8]. These length scales are plotted in Fig. 5.1 as a function of n_2.

$$d_{es} = dp\frac{n_{21}\cos(\theta)}{(1 - n_{21}^2)} \tag{5.7}$$

$$d_{ep} = dp\frac{n_{21}\cos(\theta)}{(1 - n_{21}^2)}\frac{2\sin(\theta)^2 - n_{21}^2}{(1 - n_{21}^2)\sin(\theta)^2 - n_{21}^2} \tag{5.8}$$

In the limit of small absorbance we can write an expression using Ψ and Ψ_0 (taken

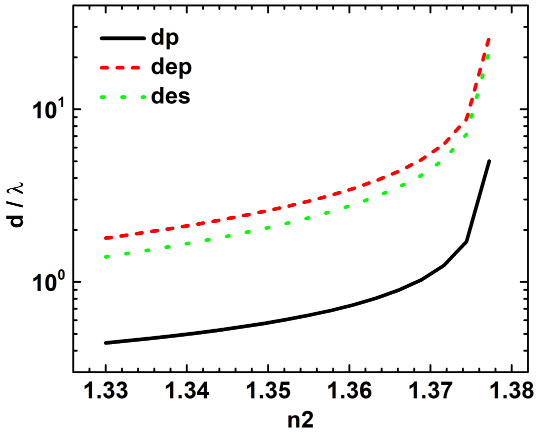

Figure 5.1: Variation of the penetration depth as a function of n_2 with fixed n_1=1.52.

from a blank measurement to correct for the background) to obtain n''.

$$\frac{|r_p|}{|r_s|}\frac{|r_{s0}|}{|r_{p0}|}=\frac{1-d_{ep}kn''}{1-d_{es}kn''}\approx 1-(d_{ep}-d_{es})kn'' \implies 1-\frac{\tan(\Psi)}{\tan(\Psi_0)}=(d_{ep}-d_{es})kn'' \quad (5.9)$$

Concerning the s-p phase shift at ATR-TIR, in the case $\theta > \theta_c$, the phase shifts under reflection are only weakly sensitive to the losses, apart from incidence close to the critical index. The s-p phase shift is sensitive to n" when $\theta < \theta_c$.

As already mentioned, the ATR spectroscopic approach does not seem to have been much considered in the case of turbid samples, though it could provide a measurement of the scattering length and its wavelength dependence, in possibly simpler way than the transmission method. We show later that ATR spectra can be obtained using VASE set-up and provide a characterization of scattering losses.

EMA model

Whereas n'' provides a good way to describe absorption losses it is not fully adapted to the case of scattering losses. It has long been proposed that the scattering losses could be described by an appropriate value of n''. van Hulst proposed to calculate n'' using Mie scattering laws. The accuracy, and physical meaning of the description of scattering losses through n'' is still discussed depending on different cases [1, 2, 11, 3, 4]

A simple effective medium (EMA) model for the overall refractive index of the turbid medium will be to consider a mixing rule according to the volume fraction ϕ for the real part and following Eq. 5.6, $n'' = \sigma c/2k$ for the imaginary part. For the Rayleigh scattering pertinent to small dielectric spheres of radius R and refractive medium n_s embedded in a medium of refractive index n_0 where $N = n_s/n_0$.

$$\begin{aligned} n_2 = n' + in'' &= (n_0^2(1-\phi) + n^2\phi)^{0.5} + i\frac{\sigma c}{2k} \\ &= (n_0^2(1-\phi) + n^2\phi)^{0.5} + i\phi(kR)^3\left(\frac{N^2-1}{N^2+2}\right)^2 \end{aligned} \tag{5.10}$$

This model provides a specific wavelength dependence, dominated by the Rayleigh scattering strong lambda dependence, but also influenced by the refractive dispersion of the dispersing liquids and the particles.

Concerning the reflectivity in the total internal reflection domain, as with absorbing material, the scattering losses give rise to a decrease of the total internal reflectivity ($r < 1$) that is measurable through reflectivity [8, 1]. It gives rise to the frustration / attenuation of the total internal reflection that can be measured. This approach to the transparent/turbid reflectivity has been developed over the last 20 years or so. It gives reasonable fits for the reflectivity and different variants are applied to characterize the turbid materials [1, 12, 13, 14]. The limitation of the simple two medium interface are well documented [14]. More elaborate, mostly empirical have been introduced to capture the different regimes of turbidity.

The simplest EMA model and Fresnel coefficient, i.e. single interface model provide only approximate results for the clear/turbid reflectivity. (We refer hereon to this two medium model as the 2MF.) It over evaluates reflectivities of strongly scattering medium. A better semi-empirical model was proposed that provide better agreement with the experiments [14]. It is an effective three medium model (referred hereon as the 3MF model), with one non-absorbing (n equal to the solvent) thin layer of thickness equal to the particle radius R in between the substrate and the material. It was introduced to model depletion of particles next to the solid surface. The model did not originate from a layer model, but from an attempt to model the near surface scattering process. It was found to provide a good representation of angular dependence of the reflectivities on a broad range of turbidity.

The reflection coefficients for the three medium system are of the form

$$r = \frac{r_{12} + r_{23} \exp{(i\beta)}}{(1 + r_{12} r_{23} \exp{(i\beta)})} \tag{5.11}$$

with $\beta = 2dkn_2 \cos{(\theta_2)}$. To the best of our knowledge, the model was mostly tested for near critical angle reflectivity and has not been tested on ellipsometry and in particular the s-p phase shift. We here seek to extend the application of the 3MF model to ellipsometry and not only reflectivity. We propose the following EMA approach to establish the wavelength dependence of the refractive index of the turbid sample. For $n'(\lambda)$ we use an mixing rule EMA (effective medium approximation for the real part based on the constituent refractive index and on their relative amount (concentration). $n''(\lambda)$ is described as a polynomial dispersion, in agreement with what is expected from Mie scattering theories [15]. We furthermore leave the thickness d of the transparent layer as an open parameter. The three models that we consider are graphically presented in Fig. 5.2. We show in the following that the 3MF model provides a good description of the VASE measurements. The reflectivity ($R_p = |r_p|^2$ and $R_s = |r_s|^2$) and $1 - \tan{(\Psi)}/\tan{(\Psi_0)}$ were used to propose a model for the wavelength dependence of the losses (this part was actually done outside of the main software, as this option is not available in the âĂIJstandardâĂİ version we used). Once the wavelength dependence losses have been determined (in a somewhat ATR way), we bring in the real part, using an EMA approximation (provided by the software). This allows to obtain a volume fraction. The overall ellipsometry data are then fitted.

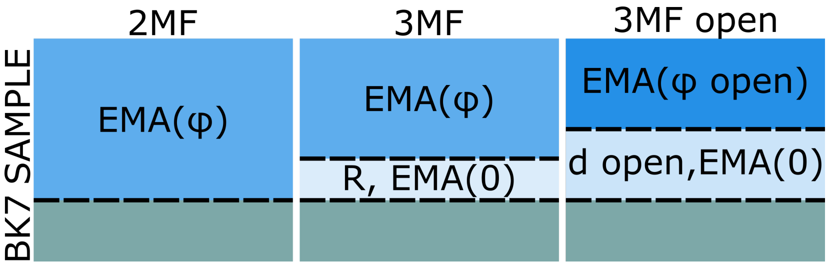

Figure 5.2: Three different effective medium models for reflectivity and ellipsometry of turbid media.

5.3 Experimental

5.3.1 Internal VASE

We implement an internal reflection geometry by adding an internal reflection flow cell to a commercial ellipsometer kindly made available to us by the Biosensors group at the University of Crete. The ellipsometer was a M-2000V from J. Woolam capable of spectroscopic measurements at variable angles with PCR$_S$A (polarizer, rotating compensator, sample analyzer) or RCE (rotating compensator ellipsometer) configuration. The setup as used is shown in Fig. 5.3 and a schematic if presented in Fig. 5.4.

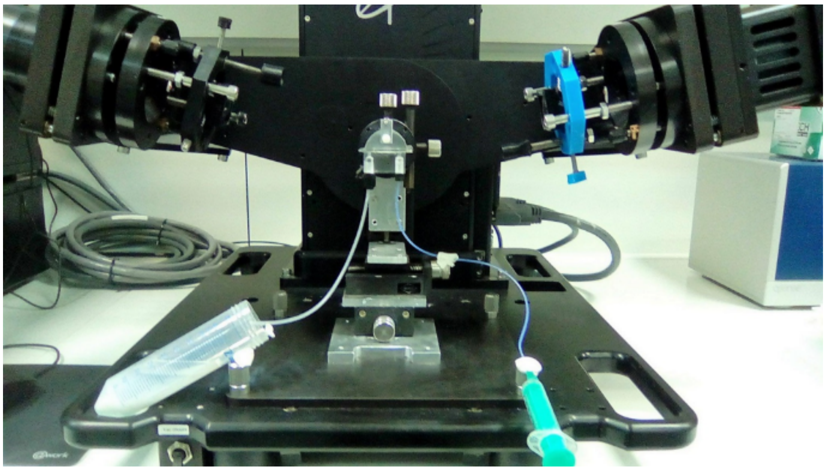

Figure 5.3: Photograph of the J. Woolam M-2000V with attachments for lensing correction and alignment stage with a sample loaded.

We used a semi-cylindrical lens (15 mm radius, with a 1 mm truncation for a disposable glass slide that serves as transparent substrate, see inset in Fig. 5.4) is used

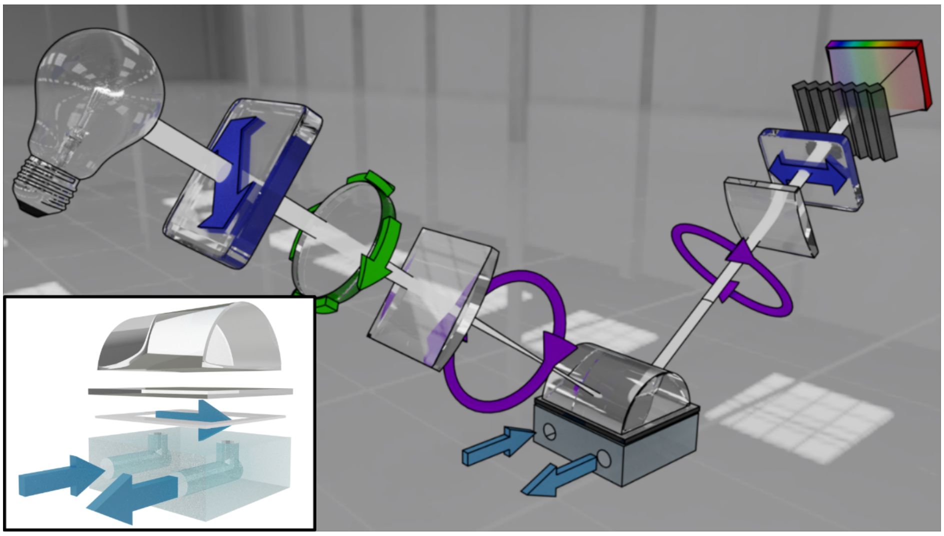

Figure 5.4: Schematic of setup. From the left: lamp, polarizer, rotating compensator, correction lens 1, semi-cylindrical sample lens, correction lens 2, analyzer, grating, CCD array detector. Inset: schematic of the flow cell used.

to introduce the light at the interface of the glass substrate and the turbid medium; the cylindrical geometry makes the light path rotational invariant, and therefore preserves the variable angle [16, 17]. An xyz and tilt alignment stage was used to align the lens.

A simple flow cell (see inset in Fig. 5.4) was constructed with a 1 mm glass slide and attached to a plexiglass piece by means of double sided tape (thickness $\sim$ 200 μm) shapped like a channel that acts as a spacer. The plexiglass piece was quipped with inlet and outlet for liquid samples. A pair of syringes was used to manipulate the sample.

To correct for the lensing of the flowcell's semi-cylindrical lens and maximize collected intensity, two more lenses are used: one for the incoming beam, and one for the reflected beam. The lenses were mounted on 3D printed mounts that fitted the machine's existing slots for focusing attachments. Both of the correction lenses had focal length of 7.5 cm and where aligned so their focus would match the one of the semi-cylindrical lens ($\sim$4.2 cm from its center).

The lenses used are all made out of BK7. They are not anti-reflection coated; we recover $\sim$80% of the source intensity. They are not achromatic; the lower bound in angular dispersion for the wavelength dispersion of the BK7 glass is of 0.12° (susceptible to alignment imperfections).

The angular range that can be covered goes from 45° to 75° of incidence (limited by the ellipsometer (45° to 90°) on the lower bound and by the sample cell geometry construction on the upper bound (75°)). BK7 glass (n 1.52 at 532 nm), allows $n_{glass} > n_{sample}$ for a large variety of samples, especially water based samples.

The M-2000V is equipped with a 50W QTH quartz tungsten halogen lamp and a grating plus CCD detector array for a spectral range of 370 to 1000 nm with 1.6 nm resolution.

The instrument is unaware of the presence of the focusing and TIR lenses and does not allow to collect normalized reflectivity curves. It does however give access to the reflected intensity (unnormalized) which for an attenuated total reflection approach (ATR). The specific ellipsometer is not meant to measure reflectivity data, and the intensity signals are rather noisy. The $\tan(\Psi) = r_p/r_s$ though less sensitive to losses than R_p or R_s was found to provide a better (less noisy) signal than the intensities. Note that there is little difference between R_p and R_s, therefore there is not a great sensitivity of the TIR ellipsometry for the losses, but it is there nonetheless. The software can also use the intensity information on the fits, but this is helpful only if the software was aware of the correction lenses.

The light travels through 4 cm of BK7 glass. This results in a considerable birefringence (a few degrees in phase difference) which is angular dependent and varies with the alignment, position of the beam and wavelength. Thankfully, the CompleteEase software is equipped to handle phase shift corrections (by subtraction) as they are common whenever windows are used; unfortunately, the angular dependence has to be taken care of manually. The birefringence is of the order of a few degrees, small enough so that a simple subtraction can be applied instead of the full Mueller matrixes of the lenses.

We used a blank measurement to measure the birefringence and the reflected intensity and $\tan(\Psi_0)$ for every measurement. This gave us the best results. We achieved

0.1° angular reproducibility with the M-2000 (on par with the setup's technical specifications). To do this one needs to take extreme care to take a reference measurement of the optical path birefringence and losses while disturbing to the least possible degree the alignment. Once the proper care has been taken, one can hope to measure differences the ellipsometric angles of 0.1°.

5.3.2 Samples and refractive indexes

As model turbid samples, we used dispersions of polystyrene latex spheres (190 nm in diameter) in water with varying concentration (10%, 5%, 2.5% and 1%). We further tested the applicability on milk.

We use the database values for the BK7 glass. We use an EMA of database values PS and water. Concerning the losses, we used a polynomial fit of the Mie scattering losses ($n'' = C_{sca}c/(2k)$) calculated with the software MiePlot [15] and the imaginary component in Eq. 5.10 for the Rayleigh scattering losses. The dispersions of the refractive indexes used in the chapter are plotted in Fig. 5.5.

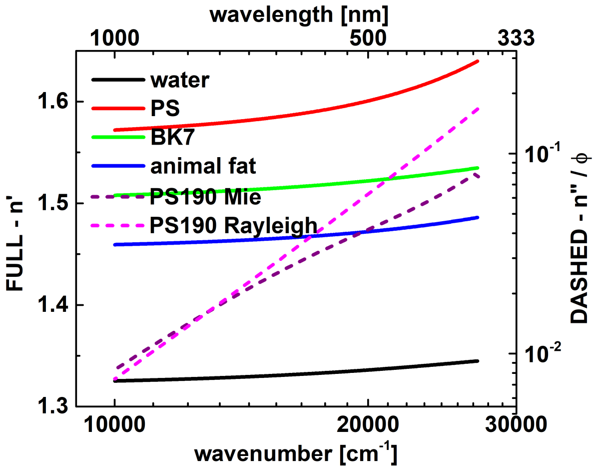

Figure 5.5: Refractive indexes used throughout the chapter. Only the scattering losses contributed to the imaginary part.

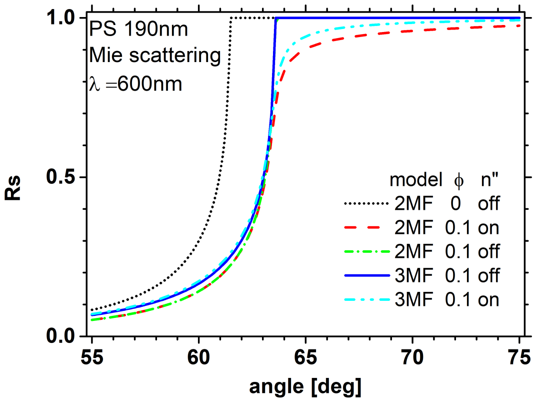

Figure 5.6: Simulations. R_s for the different models with and without losses. For the case of 10% PS. Transparent layer thickness of 95 nm = R.

5.4 Simulated reflectivity and ellipsometry

The effect of losses on the reflectivity is shown in Figs. 5.6 and 5.7 for the s polarization. As shown, the reflectivity decreases, more significantly close to the critical angle in the TIR region. The critical angle is displaced according to the EMA for all of the models shown. The use of the non-lossy layer in the 3MF model results in an increase of the reflectivity in the TIR region.

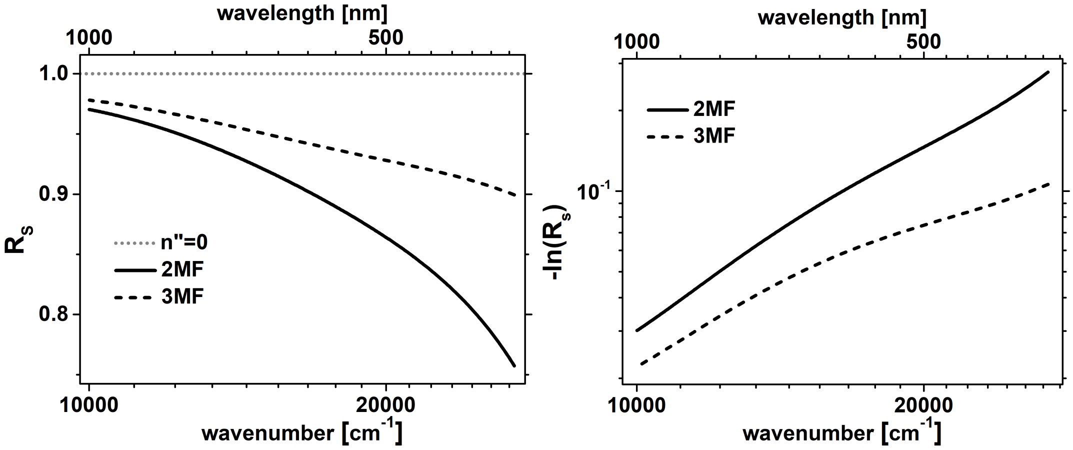

(a) (b)

Figure 5.7: Simulations. Effect of the 2MF and 3MF models on the reflectivity dispersions at 66° for a 10% dispersion of PS spheres of 190 nm in diameter.

The critical angle as seen from Δ in Fig. 5.8a also shifts according to n' given by the EMA. In addition, the presence of the non-lossy layer is seen as a non constant shift in Δ. This phase shift is present when the optical contrast exists and is positive when the layer is of lower refractive index than the bulk of the material. In Fig. 5.8b the models are compared vs. wavelength at 65°. The effect of the losses is seen mostly from some rounding before the critical angle. The phase angle is therefore not strongly sensitive to the imaginary part of the refractive index. A quick comparison between the simulated Fig. 5.8a and the typical results in 5.9 shows that the 3MF model is a good candidate to describe the data.

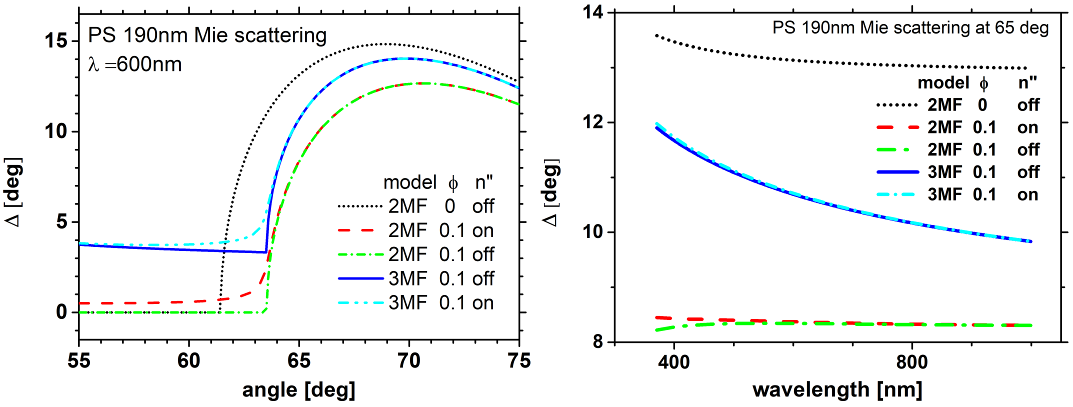

(a) (b)

Figure 5.8: Simulations. Effect of the different models on Δ. (a) Versus angle. (b) Versus wavelength.

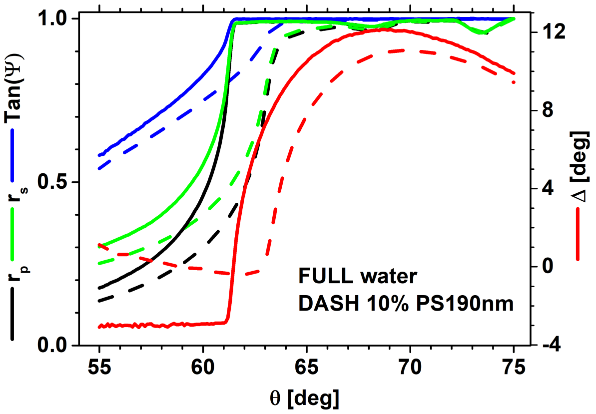

Figure 5.9: Effect of the presence of turbidity on a internal reflection VASE ($\lambda = 500$ nm). Comparison between water and a 10% dispersion of PS spheres of 190 nm in diameter.

5.5 Results and analysis

5.5.1 Wavelength dependence of Reflectivity - ATR

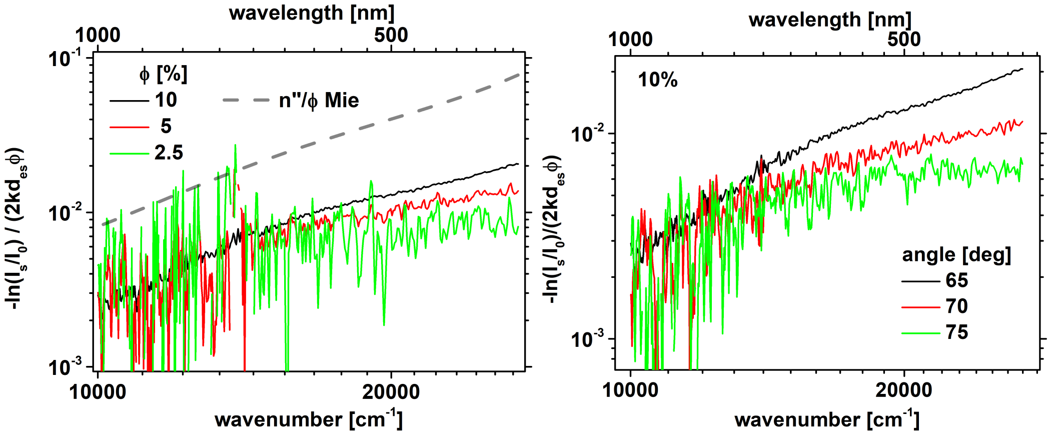

(a) (b)

Figure 5.10: Losses normalized by concentration from the ATR spectrum. Eq. was used to rescale (a) At different concentrations. Angle = 65°. (b) At different angles. ϕ=0.1.

Using the intensity recorded by the ellipsometer we have calculated the ATR spectrum according to Eq. 5.6. The ATR spectra are shown in Fig. 5.10 rescaled by the volume fraction. This approach reveals the almost k^3 dependence of losses of Rayleigh scattering. A better description of the data is given by Mie scattering theory (dashed line in Fig. 5.10) that includes the kink observed in te spectrum. There seems to be a systematic deviation with the predicted Mie curve. The lowest measurable value for αd_e was 10^{-3}. Note that to calculate d_e we used n' of the EMA according to the nominal values of ϕ. The angular do not overlap exactly, nor do the ϕ dependence. The apparent scattering losses grows faster than the concentration. In bulk in these conditions the dispersion scattering should be linear with concentration (no strong effect of particle-particle interaction). The deviation in case of ATR could be due to interfacial effects.

The scattering losses in TIR appear to be mostly independent of the polarization as seen from partial overlap of the ratio $\ln(r_p)/\ln(r_s)$ and d_{ep}/d_{es} in Fig. 5.11 according

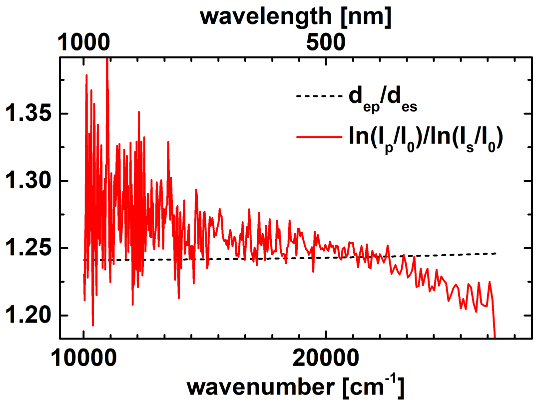

Figure 5.11: Ratio d_{ep}/d_{es} and the equivalent for the data $\ln(r_p)/\ln(r_s)$ for the 10% dispersion at 65°.

to Eqs. 5.6 and 5.7. The difference is accounted by the difference in d_e.

5.5.2 Turbid ellipsometry analysis

Here we show $\Delta - \Delta_0$ and equivalently $\tan(\Psi)/\tan(\Psi_0)$ to compare the different models with the recorded data. The $\tan(\Psi)$ plots are proportional to kn'' as per Eq. 5.9. The analysis performed here for the clear glass-turbid solution interface in the ellipsometry software (CompleteEase in our case) should be possible in any VASE software.

The best fit returned number in very good agreement with what we expect from the well-known samples, covering a very broad range of turbidity. We can obtain the composition from n' and the EMA and the scattering losses (α) from n''. This is usually considered enough for a good characterization [12].

The fit over Ψ was not sufficiently sensitive to the losses we opted for external analysis. But it did reproduce the TIR phase correctly. It also does good around TIR (as can be expected from the works on refractometry).

Two medium Fresnel (2MF) The simple Fresnel interface is poorly suited to describe the measurements. It over estimates the losses and does not capture the phase shift. As previously seen, the critical angle is given by the EMA but the extra layer missing in the 2MF model is necessary for the strong phase shift encountered.

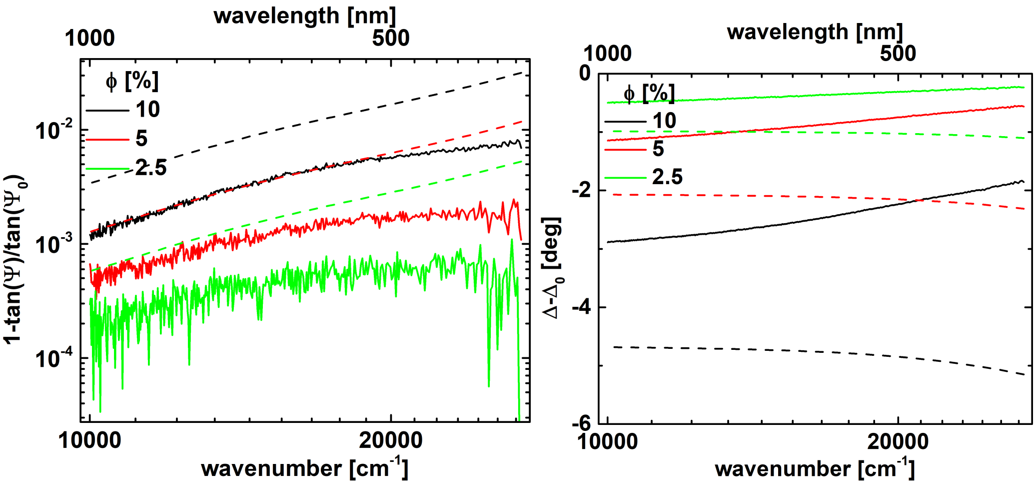

(a) (b)

Figure 5.12: Comparison with the 2MF model at 65°. The full lines are the data and the dashed lines the model.

Three medium Fresnel (3MF) The three mediums Fresnel model gives good results in [14] where it is applied to reflectivities close to the critical angle. In Fig. 5.13 we see the comparison of the model with the measured data. There is good agreement both in Ψ and Δ but the wavelength dependence of n'' is not fully captured.

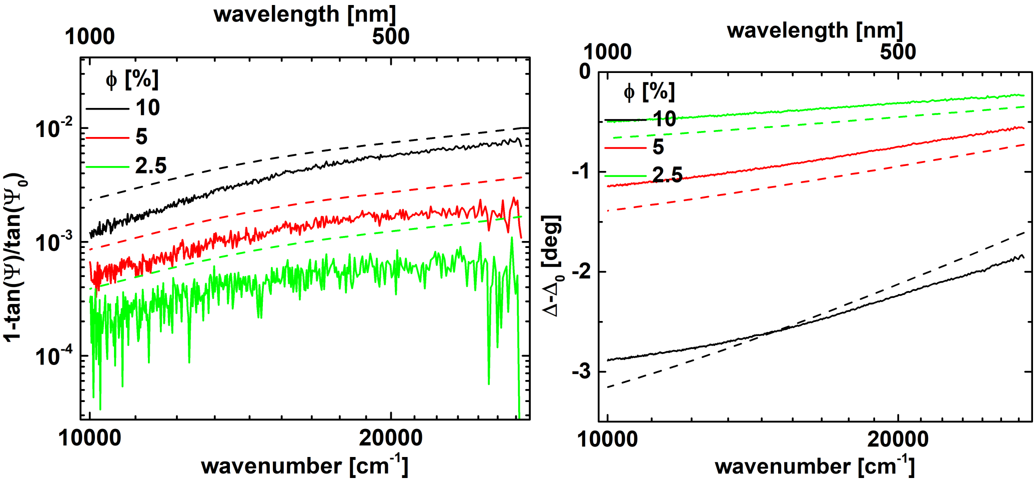

(a) (b)

Figure 5.13: Comparison with the 3MF model at 65°. The full lines are the data and the dashed lines the model.

Three medium Fresnel with open parameters (3MF open) It is possible to use $\tan(\Psi)$ to measure scattering losses. Still, the matter over the correct relevant length scale is in debate [1, 13, 14]. Allowing for the thickness d of the transparent layer, the volume fraction for the EMA and a prefactor A on the imaginary part of the refractive index to account for the discrepancies encountered in the ATR approach. Obviously this leads to better fits. The values in table 5.1 for the volume fractions are comparable to the nominal values, though lower, yet in good agreement among themselves. The value for the prefactor A did not vary much while the value of d decreased with increasing concentration. We have seen observed from the ATR spectra that the data disagree with the prediction by a prefactor. We have also seen that the different concentrations fail to overlap with each other. For which we suspect there are interfacial effects at play. Within this scenario it is possible for the value of d to be a function of the concentration.

sample	ϕ [%]	A	d [nm]
10	8.7	0.74	69
5	4.4	0.76	106
2.5	2.1	0.67	114

Table 5.1: Values obtained from fitting ϕ, d and a prefactor A for the losses.

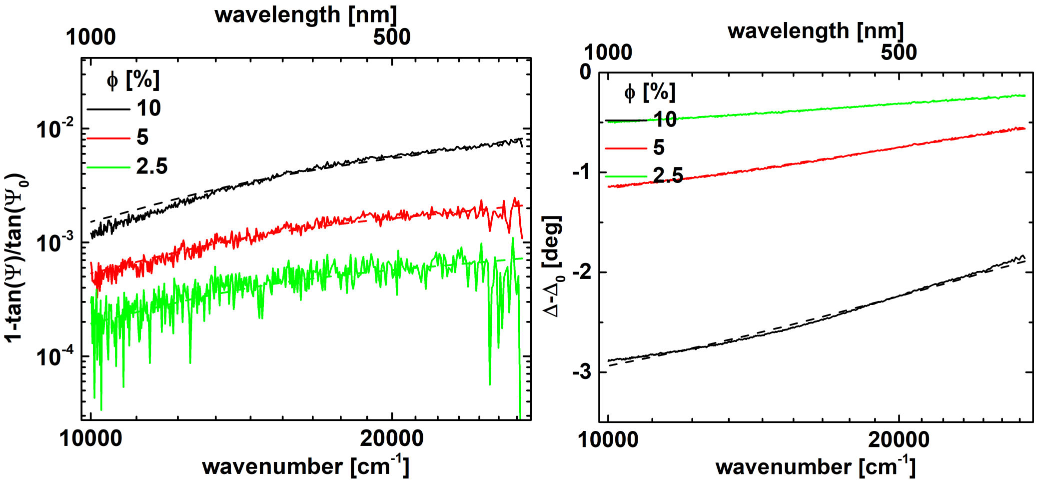

(a) (b)

Figure 5.14: Comparison with the 3MF model at 65° with free parameters to minimize $\tan(\Psi)$. The full lines are the data and the dashed lines the model.

Angle - concentration equivalence We found that there is a similarity between change of angle (length scale) and the change of concentration. In fact, in Fig. 5.15 we can see that the values of Ψ and Δ where the same for the 10% at 70° and the 5% at 65°, as well as for the 10% at 75° and the 2.5% at 65°. This empirical finding points out to a possible connection of the penetration depth (governed by the angle of incidence) and of the amount of scattering (governed by the concentration). Reducing penetration depth has somehow a similar effect on losses than reducing the concentration of scatterers.

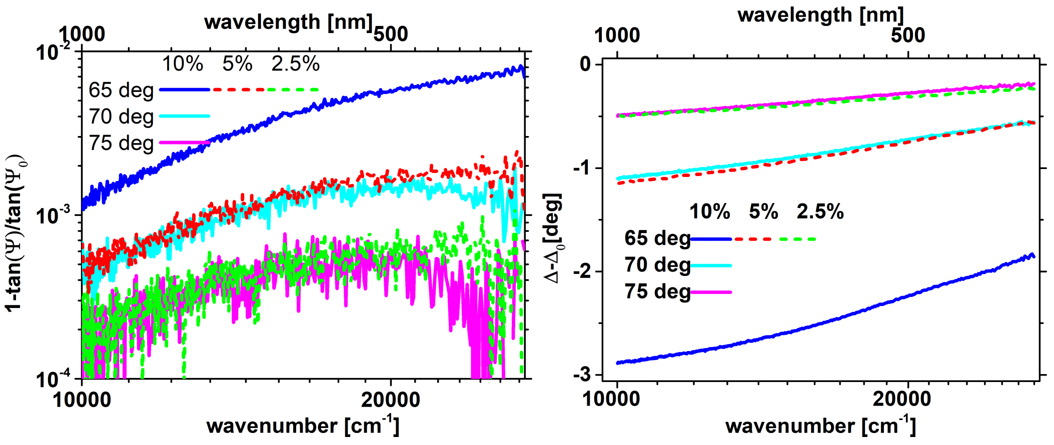

(a) (b)

Figure 5.15: Ψ and Δ as a function both of angle and concentration. For an unclear reason there is an equivalence between measurement angle and the concentration of the turbid dispersion.

5.6 Milk

We evaluated the capacity of the VASE approach with two milk samples. One full fat (3.5%) and one diluted in half. Homogenized milk as a broad fat globules size distribution depending on the process with average size in the order of a μm [18]. We can appreciate from Fig. 5.16 a clear horizontal shift in the critical angle of 1° and 2° for the half fat and the full fat respectively relative to the clear interface. Also, we see no vertical shift on the Δ indicating no transparent layer (or depleted of scatterers) or poor contrast with little contrast. From Mie scattering simulations we expect $n'' \propto k^0$ in our spectral range and therefore $1 - \tan(\Psi)/\tan(Psi_0) \propto k$ as observed in Fig. 5.17

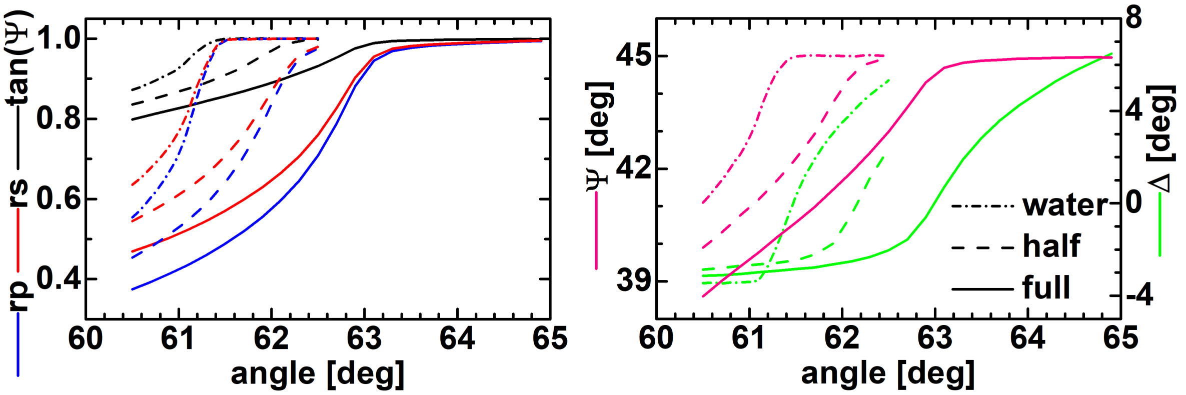

Figure 5.16: ATR and spectroscopic quantities at λ=500 nm.

is a result of a complex size distribution with high polydispersity and contribution of particles well above the 100 nm. The refractive index of proteins is known to vary considerably depending on the composition of the specific proteins which varies with origin [19]. We decided to use a simple two component EMA between animal fat and water (Fig. 5.5) to model n' where the fat component encompasses the fat, proteins and in general the whole dry content. The dry content is expected to be around 12% in mass for the full milk.

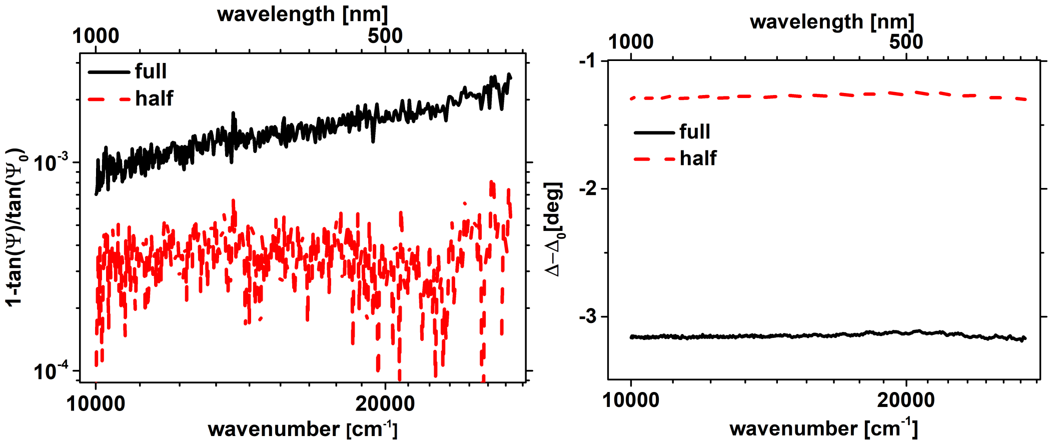

(a) (b)

Figure 5.17: Ellipsometric data for full milk and diluted milk. Angle 65°.

The best fit for the transparent layer thickness of the 3MF model was close to 0 nm so we opted for the simpler 2MF model. It would appear that there is no physical layer as on the case of the PS spheres. The values for n' and n'' in Fig. 5.18 are close to those in [12]. As for the PS dispersion we observe in Fig. (right)5.18 that

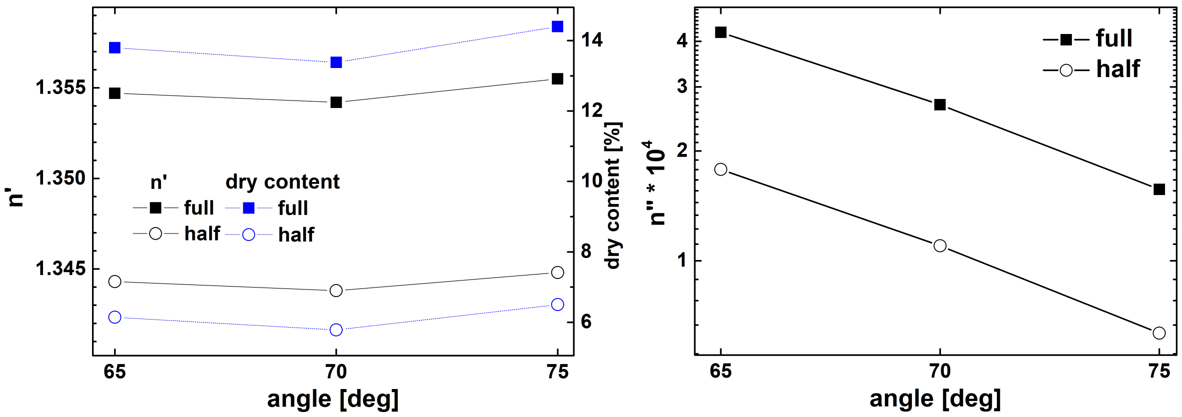

Figure 5.18: Fit results for from a flat n'' dispersion and a 2 component EMA of water and dry content. (left) n' at 500 nm and dry content percentage. (right) n''

reducing the penetration depth has somehow a similar effect on losses than reducing the concentration of scatterers. It would appear from the necessity of the 2MF model and the close agreement with literature in both components of the refractive index that the internal reflection results from milk are closer to the bulk values compared to those for the PS particle suspension. Nonetheless it is expected for milk to interact strongly with the wall as adsorption is readily observed and can be monitored with ellipsometry.

5.7 Discussion and conclusions

We have investigated the unexplored effect of losses by scattering in turbid media in internal reflection variable angle spectroscopic ellipsometry. We based ourselves in simple effective models that have been developed for use in reflectivity [14]. VASE characterization can be utilized to find the composition from the real part n' and n'' can then be used to deduce some average size.

We found that EMA models can indeed be used in ellipsometry for turbid samples capturing well the data and giving access to concentration through the real part of n. The imaginary part of n from scattering losses can be measured in an ATR fashion using either r or $\tan(\Psi)$ (provides better signal to noise ratio on the ellipsometer) but the length scale associated is still a matter of debate. We found n'' to be not sensitive to polarization withing the Fresnel picture. The low values of n'' have little effect on the ellipsometric angles making it difficult for the softwares provided by the vendors to minimize over possible dispersions unless the reflectivity is considered (the option is available in the CompleteEase, but requires correction for the extra lenses utilized which is not possible). Otherwise, it is more appropriate to measure from the attenuated reflectivity.

One of the questions that we would like to answer is to what extend the technique provides an interfacial (or bulk) characterization. In refractometry the value of the critical angle is used to measure refractive index of bulk materials. Though it is determined by the first micron or so close to the interface, this is a large enough length scale for standard liquids. In the case of colloidal solutions where the particle have radius that are comparable to the wavelength this assumption may break down. In that case the reflectivity may not average over sufficient large length scales to obtain bulk-like response, and therefore the measure might become interface sensitive.

The transparent thickness used in the three medium model was found to be physically present from the phase angle, even outside the TIR region. It plays an important role decreasing the losses with respect to the bulk value. Moreover it was seen from spectroscopic ATR and ellipsometry that the value of the scattering losses is lower than the predicted value for the bulk and that possibly both an optical (d_e) and a physical length ($\sim R$ or $c(z)$) scale within the material are responsible in regulating its value. This indicates that the measurements are surface sensitive.

5.8 Acknowledgements

We thank the following people for their contributions. E. Gizeli from the Biosensors group in the University of Crete for giving us access to their ellipsometer and laboratory. All the members of the Biosensors group for their company, smiles and delicious snacks.

Bibliography

[1] I. Niskanen, J. Räty, and K.-E. Peiponen, “Complex refractive index of turbid liquids,” *Optics Letters*, vol. 32, p. 862, apr 2007.

[2] W. R. Calhoun, H. Maeta, A. Combs, L. M. Bali, and S. Bali, “Measurement of the refractive index of highly turbid media,” *Optics Letters*, vol. 35, p. 1224, apr 2010.

[3] H. Contreras-Tello and A. García-Valenzuela, “Refractive index measurement of turbid media by transmission of backscattered light near the critical angle,” *Applied Optics*, vol. 53, no. 21, p. 4768, 2014.

[4] J. Sun, J. Wang, Q. Ye, J. Mei, W. Zhou, C. Zhang, and J. Tian, “Analysis of reflectance curve of turbid media and determination of the non-surface complex refractive index,” *Optics Express*, vol. 23, p. 24602, sep 2015.

[5] H. Arwin, M. Poksinski, and K. Johansen, “Total internal reflection ellipsometry: principles and applications.,” *Applied Optics*, vol. 43, no. 15, pp. 3028–3036, 2004.

[6] J. A. Rety and K. E. Peiponen, “Reflectance study of milk in the UV-visible range,” *Applied Spectroscopy*, vol. 53, no. 9, pp. 1123–1127, 1999.

[7] K. E. Peiponen, A. Jaskelainen, J. Raty, O. Richard, U. Tapper, E. I. Kauppinen, and K. Lumme, “Reflectance study of pigment slurries,” *Applied Spectroscopy*, vol. 54, no. 6, pp. 878–884, 2000.

[8] E. Goormaghtigh, V. Raussens, and J.-M. Ruysschaert, “Attenuated total reflection infrared spectroscopy of proteins and lipids in biological membranes,” *Biochimica et Biophysica Acta (BBA) - Reviews on Biomembranes*, vol. 1422, pp. 105–185, jul 1999.

[9] F. de Fornel, *Evanescent waves : from Newtonian optics to atomic optics*. Springer, 2001.

[10] D. A. Woods and C. D. Bain, “Total internal reflection spectroscopy for studying soft matter,” *Soft Matter*, vol. 10, p. 1071, jan 2014.

[11] K.-E. Peiponen, J. Räty, and I. Niskanen, “Measurement of the refractive index of highly turbid media: comment,” *Optics Letters*, vol. 35, p. 4108, dec 2010.

[12] W. Calhoun, H. Maeta, S. Roy, L. Bali, and S. Bali, “Sensitive real-time measurement of the refractive index and attenuation coefficient of milk and milk-cream mixtures,” *Journal of Dairy Science*, vol. 93, pp. 3497–3504, aug 2010.

[13] W. Guo, M. Xia, W. Li, J. Dai, X. Zhang, and K. Yang, “A local curve-fitting method for the complex refractive index measurement of turbid media,” *Measurement Science and Technology*, vol. 23, no. 4, p. 047001, 2012.

[14] G. Morales-Luna, H. Contreras-Tello, A. García-Valenzuela, and R. G. Barrera, "Experimental Test of Reflectivity Formulas for Turbid Colloids: Beyond the Fresnel Reflection Amplitudes," *Journal of Physical Chemistry B*, vol. 120, no. 3, pp. 583–595, 2016.

[15] P. Laven, "MiePlot software, http://www.philiplaven.com/mieplot.htm."

[16] B. Loppinet, J. K. G. Dhont, and P. Lang, "Near-field laser Doppler velocimetry measures near-wall velocities," *European Physcal Journal E*, vol. 35, jul 2012.

[17] P. Petrik, E. Agocs, B. Kalas, P. Kozma, B. Fodor, J. Nador, C. Major, and M. Fried, "Multiple angle of incidence, spectroscopic, plasmon-enhanced, internal reflection ellipsometry for the characterization of solid-liquid interface processes," p. 95290W, SPIE, jun 2015.

[18] K. Nowak, K. Kiełczewska, D. Murach, and A. Dąbrowska, "Analysis of the size of fat globules in milk and cream dispersed in different reagents solutions," *Polish Journal of Natural Sciences*, vol. 32, no. 4, pp. 719–732, 2017.

[19] H. Zhao, P. H. Brown, and P. Schuck, "On the distribution of protein refractive index increments.," *Biophysical journal*, vol. 100, pp. 2309–17, may 2011.

Chapter 6

Internal reflection study of polyelectrolyte brushes

6.1 Introduction

A typical interfacial system is the one made by swollen polymer layer grafted to a solid surface. It is widely used in different contexts, to modify surface and in particular to stabilize colloidal particles against attractive van der Waals interactions [1]. Polymer brushes (PB) designate the extended conformation that polymeric chains attached chemically or physically from one free end to a solid surface adopt when the grafting density is large enough [2, 3]. PB have been the subject of very large attention. The case of water soluble system is of particular interest. The water soluble polymers can be divided in two categories, neutral polymer (such as poly(ethylene oxide)) and charged polymers refered to as polyelectrolyte (PE). PE possess very specific properties from their polymer and electrostatic nature that renders them rather different from neutral polymers. The case of polyelectrolyte brushes (PEB) or grafted PE is different from neutral PB [4]. Large research effort have come from theory, from chemistry and from properties (not always very linked). Grafted PE are now commonly used as a powerful tool for surface functionalization. If the constituting polymer are thermo-, photo- and pH responsive, the brush can become responsive, providing versatility for applications.

Many applications have received attention including: Steric and entropic repulsion of PB's together with hydration layers make them great for anti-fouling, important for medical devices, marine application and water processing [5]. Controlled adhesion and release of cells can be achieved by use of thermoresponsive polymers. By moving through the lower critical solution temperature (LCST), one can trigger attachment or detachment of cells [6]. Controlled adhesion of reagents into ordered arrays for biosensing applications is promising [7]. Bioelectronic devices can be constructed based on switchable and tunable redox acivity of pH responsive brushes [8]. Polymer brushes can be used to tune the properties of colloidal particles, including their size and aggregation [9, 10, 11]. These colloids can be used for example in drug delivery applications [12]. Another possibility is to use PB's to control chemical gates that mimic biological channels [13].

The following reviews contain many more application and walk the reader through available architectures (block copolymers, bottle brushes, gradient films,...) and chemistries (ARTP, RAFT,...) [14, 15, 16, 17].

In this chapter, we attempt to study the equilibrium dynamics and kinetics of polyelectrolyte brushes of sufficiently large molecular weight. Very little knowledge is available on the dynamics of such systems. Measurements of internal dynamics of polymer brushes are not intensely pursued in literature, due to lack of experimental techniques. Our study was carried out using evanescent wave dynamic light scattering, that has so far mostly been applied to the case of neutral polymer brush [18, 19]. Understanding dynamics requires a good knowledge of the static picture, in this case the swelling, or more precisely the polymer concentration profile perpendicular to the substrate. We use internal reflection ellipsometry to assess these profiles [20]. Many studies have reported the swelling behavior of such PE responsive brushes. The time dependence of the response is important with practical implications. Several studies have reported rather long equilibration time of the layer following the change of pH of the surrounding fluid [21]. The origin of the slow response is not fully resolved. Fewer have also looked into the kinetics, i.e. the time needed for the specific response to become effective. Neutron or X-ray reflectivity could possible provide more precise profiles, but they are less accessible techniques. Moreover, it will also us to explore the limit of optical ellipsometry to measure the concentration profile. As we are using an optical characterization, we require relatively large molecular weight (layer of hundreds of nm).

The study was meant to examine a range of varying grafting density brushes. However, it was found from the ellipsometric measurements that the samples had undergone degrafting, so that the grafting densities of the measured samples were different from the original nominal ones. This was a considerable obstacle that prevented us from obtaining substantial results.

6.2 Experimental

6.2.1 Synthesis

We aimed for a series of large molecular weight weak base with varying grafting density.

The synthesis was kindly carried out by E. Koufakis from M. Vamvakakis laboratory at the chemistry department of the University of Crete. The polymer brushes were weak polyelectrolyte brushes of PDMAEMA (poly(2-(dimethylamino)ethyl methacrylate, commonly known as polymadame) grown with a bottom-up approach through surface initialized ATRP [22].

Silicon wafers and glass slides (1 mm thickness) were immersed in piranha solution (1:3 mixture of 30% H_2O_2 aqueous solution and 98% sulfuric acid) followed by heating to 100° to remove any organic residues and create silanol groups on the surface. After 30 min they were removed and rinsed extensively with water. Folowing they were dried under nitrogen and placed under vacuum for 1 h. A self assembled monolayer of surface initiator BIDS ((3-(2-bromoisobutyryl)propyl)dimethylethoxy silane) was formed by

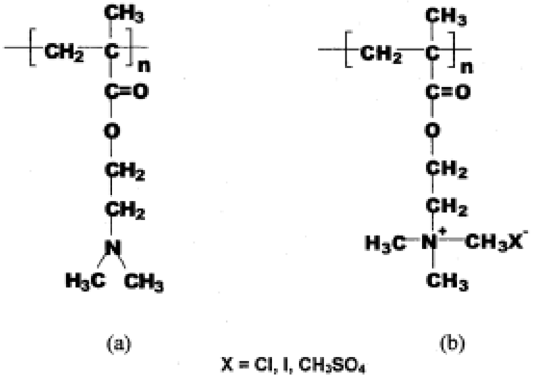

Figure 6.1: (a) PDMAEMA (samples B,C,D,E and F) (b) Quaternized PDMAEMA (sample Q-A), also known as PMETAC.

immersing the substrates overnight in a vial containing 0.5 % v/v BIDS in anhydrous toluene. After incubation period the substrates were rinsed with toluene and dried with nitrogen prior the PB growth.

For lower grafting densities PAPDS ((3-(pivaloylamido)propyl)dimethylethoxy silane) was mixed with the BIDS to block part of the sites. Different relative concentrations were used to achieve varied ratio of active initiator sites and non-reactive sites.

Following, DMAEMA monomer (157 Da), Copper(I) Bromide, HMTETA (1, 1, 4, 7, 10, 10-Hexamethyltriethylene-tetramine) and free initiator (EBIB, ethyl 2-Bromoisobutyrate) previously mixed and freeze dried were introduced into the reaction chamber. The free initiator is expected to have the same kinetics as the surface bound initiator; its purpose is to provide free polymer that can later be characterized for its molecular weight, therefore giving the molecular weight of the grafted chains [23]. The polymerization was left to run overnight for 24 hours.

For every grafting density, brushes were grown on glass and on Si wafer. The Si wafer allows easier characterization by ellipsometry.

6.2.2 Samples

Pristine samples

The samples are listed on table 6.1. The molecular of the relative PMMA standard in gel permeation chromatography is 150 kDa and the polydispersity is 1.29, for all the samples. The equivalent R_g=17 nm, from this value the inverse area per polymer is $\pi R_g^2 = 0.0011 nm^{-2}$ and the contour chain length is 170 nm. The dry thickness d was obtained from ellipsometer measurements done on the silicon wafers, from where also the refractive index dispersion of the polymer brush was obtained with a best fit to a Cauchy dispersion ($n(\lambda) = 1.487 + 0.00821 * 10^6 \lambda^{-2} - 0.00032086 * 10^{12} \lambda^{-4}$ with λ in nm). Correct characterization of the real grafting density σ requires knowledge of the molecular weight Mw and the degree of polymerization N_P according to:

$$\sigma = \frac{\rho N_A d}{N_P m} = \frac{\rho N_A d}{Mw} \tag{6.1}$$

where ρ is the bulk density (assumed equal to 1 here), N_A is Avogadro's number and m the monomer mass. According to the values in

The σ values in table 6.1 are relative to the PMMA standards and therefore "effective". The higher density brushes were approximately 600 times more compressed than the free chain. Sample Q-A and B had the same grafting density but Q-A had its ammonium group quaternized with a methyl group (known in literature as PMETAC) and therefore fully ionized and swollen in the absence of salts. Note that both of these samples have a thickness comparable to the contour length of the PMMA standard.

Fig. 6.2 shows that the dry thickness of the brushes grows almost linear as expected from density arguments. The growth though is slightly stronger than linear indicating that the surface bound activator (BIDS) seems to have been more successful at binding itself to the surface than the inactive site blocker (PAPDS).

Sample	BIDS:PAPDS	d [nm]	$\sigma[chains/nm^2]$
Q-A	10:0	145	0.6
B	10:0	145	0.6
C	5:5	56	0.2
D	3:7	27	0.1
E	2:8	16	0.07
F	1:9	10	0.04

Table 6.1: Table summarizing the samples used on this study. All samples have same according to GPC. The equivalent PMMA in THF is Mw = $150kDa$ with polydispersity PDI($M_w/M_N = 1.29$). The thickness values are from the dry brushes on silicon wafers.

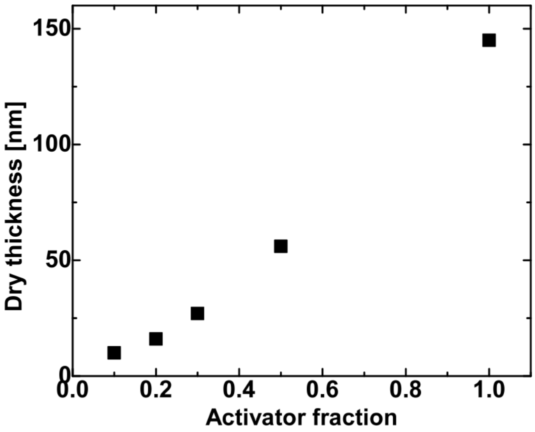

Figure 6.2: Dry thickness as measured on the silicon wafers by ellipsometry as a function of the ratio of surface initiator to inactive site according to the concentration in solution of the to reactants.

buffers Polymadame is a weak base with pKa 7 [24] so buffers of pH 4 (citric acid and NaOH, ionic strength 0.1 M, salt content 0.1 M) and 10 (Na2CO3 and NaHCO3, ionic strength 0.08 M, salt content 0.19 M) were used to alter between the swollen and unswollen state. Rinsing was done with pH 5 milliQ water. At pH 4, the polymer in bulk is expected to be ionized above 99% and, at pH 10 below 0.1% following from the mass action law $\alpha/(1-\alpha) = K_b/C_{OH}$, where α is the degree of ionization, $K_b = 10^{-(14-pK_a)}$ and $C_{OH} = 10^{-(14-pH)}$.

Storage The samples on the glass slides where kept in an isopropanol bath for at least five month before they were turned into flow cells. No reliable record of the dates was kept. Once the flow cell were built, the cell were filled with water but left unattended and no record was kept for whether the cell dried or not.

Degrafting

The samples were stored for a long period of time. As is now apparent from careful reading of literature, this type of graft may be subject to “slow” degrafting. The degrafting is caused by hydrolysis of the silane and ester groups. The samples had been stored for a long period of time in isopropanol, that seems to have undergone such degrafting. As a consequence of the long storage and possible degrafting, the value of the grafted density can not be assumed to be the same as the one estimated from the dry thickness of the brush on Si wafer. As we will explain below, different samples suffered differently from degrafting. In particular the quaternized sample Q-A remained presumably intact due to its stretched conformation [25].

6.2.3 Flowcell for internal reflection

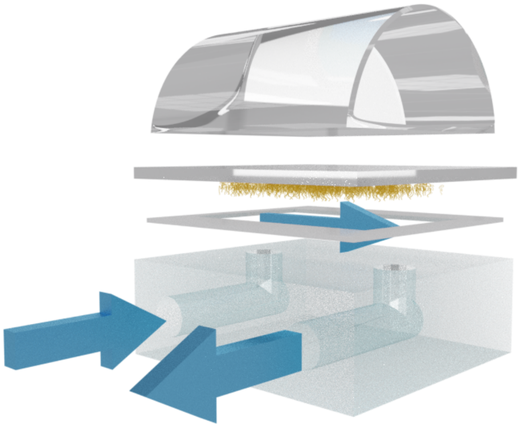

Figure 6.3: Sample construction. Glass slide with PEB is stuck to a plexiglass adaptor with via double sided tape cut in such a way to create a channel. The lens is then joined by refractive index matching liquid to the glass slide.

One of the experimental aims of the study was to ascert the possibility to measure TIR spectroscopy of typical ATRP polymer directly grafted on glass. For this we make use of standard disposable microscope glass plate, that are fitted on a truncated semi-cylindrical lens to allow the use of variable incidence angle internal reflection. A simple plexiglass flow cell was designed to be fitted on top of the glass plate to allow the insertion of liquids. The thickness of the tape joining the slide and the plexiglass piece is of the order of a few 100 microns and acts as a spacer to give height to the flowcell. The overall flow cell is shown in Fig. 6.3. The same cell could be used for ellipsometry and EWDLS.

6.2.4 Setup-VASE

Variable angle spectroscopic ellipsometry and the setup are better described in chapter 5.

The ellipsometric experiments were done on an M-2000V VASE setup by J.A. Woollam kindly made available by the Biosensors group at the biology department in the University of Crete. A sample lens, for internal reflection was adapted together with an alignment stage (xyz, tilt and rotation) onto the setup. Proper measurements require good mechanical stability. The wavelength range in use goes from 370 nm to 1000 nm with ∼1.6 nm resolution. The nominal angular reproducibility is, as written on the system documentation, 0.075° for Ψ and 0.05° for Δ on 95% of the wavelengths.

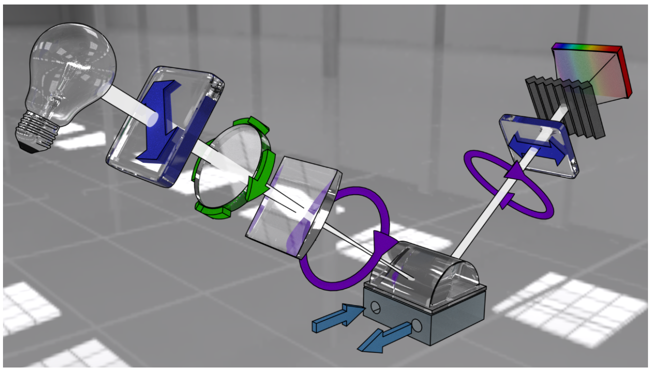

Figure 6.4: Optical path on the ellipsometer experiments for the polyelectrolyte brushes. The path is as follows: white light source - polarizer - rotating compensator - compensating lens - sample (samplelens and sample slide) - polarizer - grating - CCD array detector.

The light path used is shown in Fig. 6.4. A cylindrical lens was added to correct for the lensing of the main TIR lens. The focal points of both the sample and the correction lenses are made to match so that the rays arrive parallel at the reflection spot. Due to the chromatic dispersion of the lenses a minimum angular dispersion of 0.12° is expected. On the following fits, an angular dispersion of 0.8° is admitted given alignment imperfections and feedback from the best fits.

The glass material of the lenses is birefringent. The 3.5 cm of glass on the light path accumulate to the phase shift shown in figure 6.5. This is can be of the order of a few degrees and is a function of the position, angle and wavelength, as a result motion of the optical components and changes in alignment result in reproducibility issues on the phase angle. The CompleteEase software allows to correct for a wavelength dispersion birefringence by subtraction; this is valid for small angles as on this case. The experiments in this section were carried out without a third lens at the detection side (as on the section on Turbid ellipsometry).

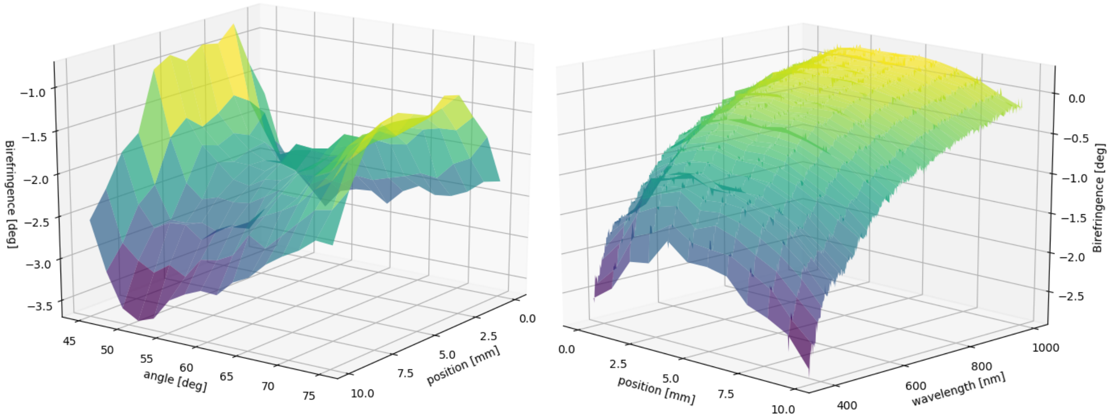

(a) $\lambda = 500nm$ **(b)** Angle = 65°

Figure 6.5: Birefringence ($\Delta - \Delta_0$) on the optical path (3.5 cm) mapped along 1 cm of BK7 glass lens.

6.2.5 Kinetics measurement protocol

Measurements of the kinetics of swelling-deswelling, were done at fixed angle of reflection on the ellipsometer. The evolution of the ellipsometric angles was recorded as buffers were changed and the PEB transitioned between states. Here we worked at 58°, before the TIR region. The time resolution is of 0.5 s, so we can only hope to observe transitions on longer time scales than that. Typical evolution of Ψ and Δ are shown

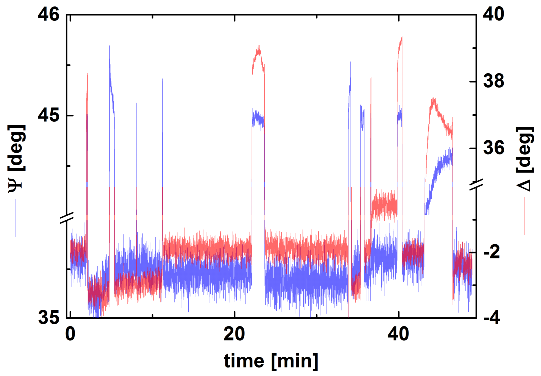

Figure 6.6: Ellipsometric angles at 800 nm for sample C during the kinetic measurement.

in Fig. 6.6.

The data were fitted over all of the time range with a box model as the one in Fig. 6.13. An effective medium approximation (EMA) was used to model the refractive indexes. The EMA is simply a linear combination of the refractive index of the polymer and of the solvent (water). A mass conservation relation was used according to the values of dry thickness and the homogeneous content of water used for the EMA. The wet thickness is then related to the dry thickness by:

$$d_{wet} = \frac{d_{dry}}{(1 - water\%/100)} \tag{6.2}$$

Air was shortly introduced in between the two fluids. Consequently, the kinetics observed correspond to a time of equilibration of the PEB system, and not precisely to a swelling-deswelling time.

The moments when the solvent was evacuated can be recognized from when the values in Ψ and Δ shoot, Ψ goes to a value close to 45, corresponding to total internal reflection with air. On those moments also, the fit for the thickness and swelling ratio fails, and the value displayed goes to 0 or another saturated value.

The buffer was changed several times between pH 4 and 10. In between the sample was rinsed with pH 5 milliQ water. The pH was periodically controlled with pH indicating strips at the outlet of the flow cell.

We used the Savitzky-Golay algorithm with 7 points interval (3.5 seconds) and a linear polynomial for smoothening the wet thickness. Keep in mind that the ellipsometer's software calculates the wet thickness with the entire wavelength dispersions which reduces the noise in advance.

As the characteristic time, we took the half time of the decay on the evolution of the wet thickness from the moment the buffer was introduced.

6.2.6 EW-DLS setup

The flow cell in Fig. 6.3 was mounted on the top of axis 1 of the 2 axis goniometer, on top on x,y,z linear stage, and a tilt base that allow the proper alignement. A more detailed description can be found in chapter 3. The setup is shown in Fig. 6.7.

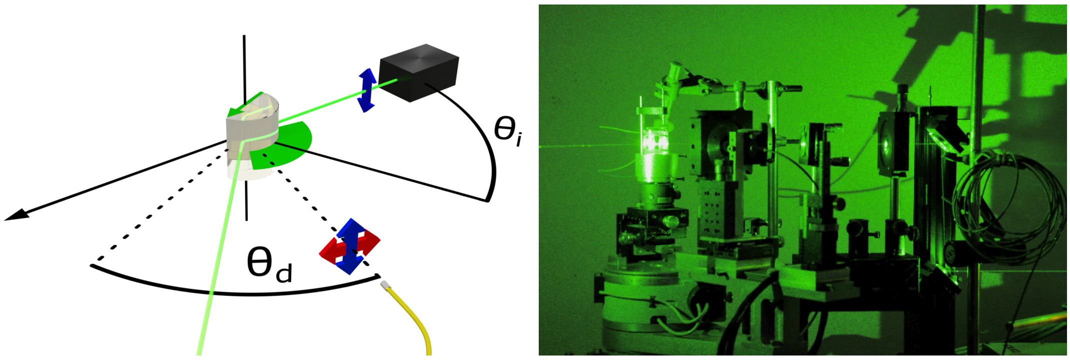

(a) (b)

Figure 6.7: (a) Schematic of the EW-DLS setup. (b) Photograph of the EW-DLS setup with the flow cell mounted on the axis 1 of the 2-axes goniometer. The laser beam comes from the right. Credit to A. Larsen.

6.3 VASE results, concentration profile

6.3.1 Computer modeling

In order to evaluate the capacity of internal VASE to resolve the concentration profile we did a lot of modeling, using the powerful Complete EASE software, as well as home developed Mathematica modeling.

Given the thickness, molecular weight and grafting density, the swollen brushes

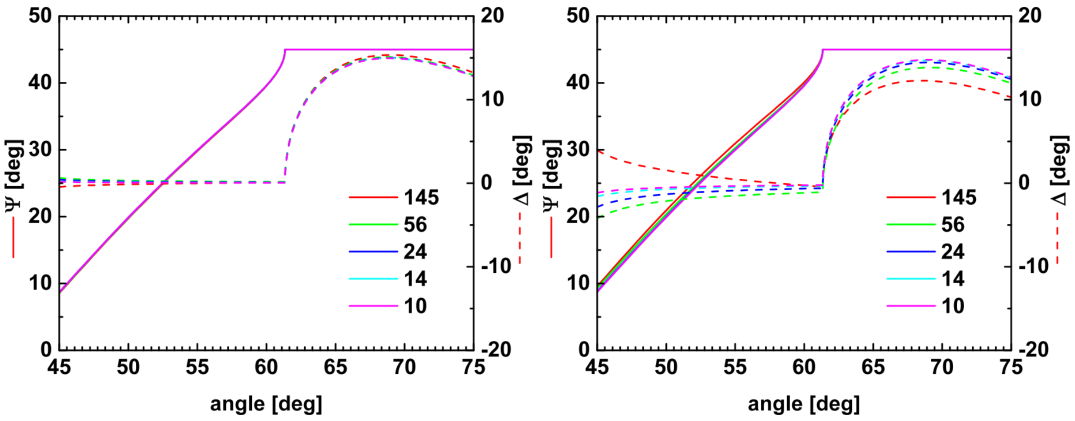

(a) 0% water content **(b)** 10% water content

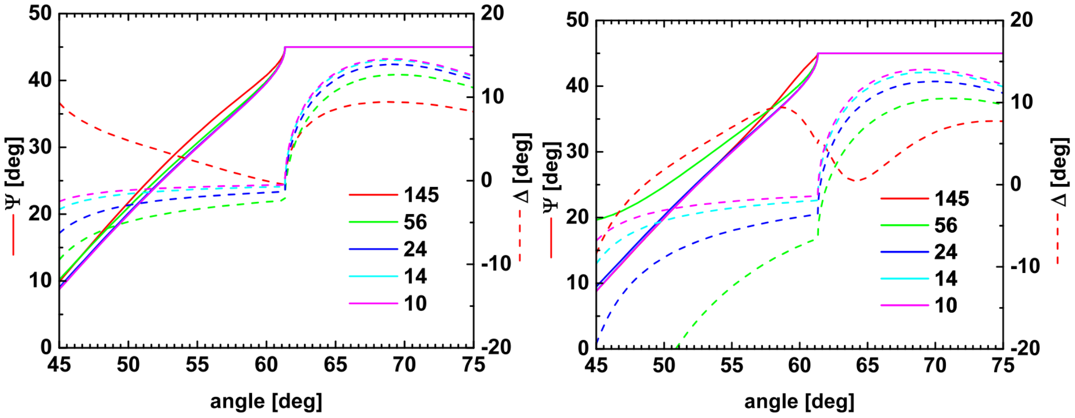

(c) 20% water content **(d)** 50% water content

Figure 6.8: Simulated ellipsometric data under internal reflection for the different dry sample thickness given different percentage of water content. $\lambda = 500nm$

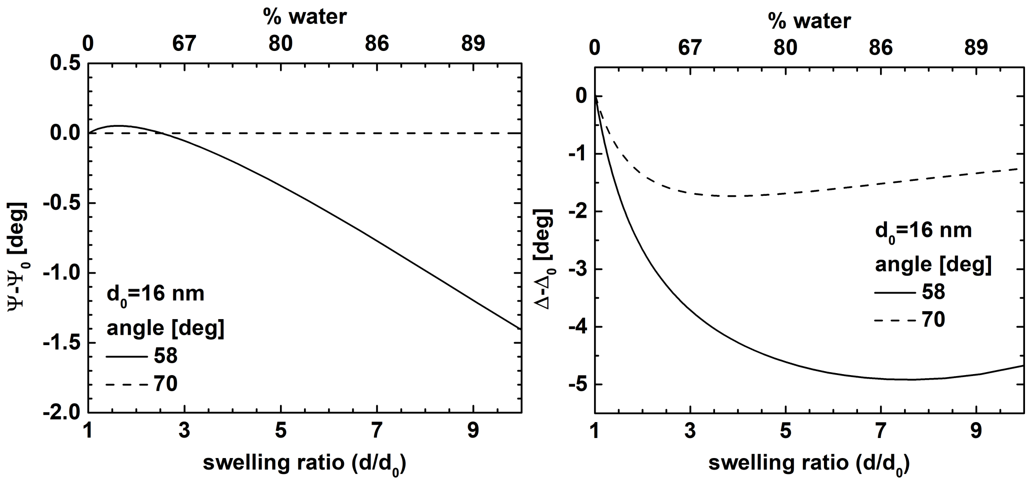

(a) (b)

Figure 6.9: Simulated ellipsometric angles as a function of the swelling ratio for a dry thickness of 16 nm at angles 58° and 70° and λ=500 nm. (a) $\Psi - \Psi_0$(b) $\Delta - \Delta_0$

thicknesses can be estimated. In particular, the maximum length is limited by the contour length 1000*0.5∼500 nm that should be independent of the grafting density. Therefore the lower grafting density samples may swell more than the higher ones. The estimated maximum swelling is ranging from 3 to 50 from sample A to F. In average concentration from 33% to 2%.

We used a simple box model for the concentration profile. The Δ and Ψ corresponding to different swelling are show in Fig. 6.8. Fig. 6.9 shows the evolution of the ellipsometric angles for a 16 nm dry thickness brush with the swelling. The variations in signal are strong and higher than the instrument resolution for swelling ratios below 3. They are though comparable to the birefringence shown in Fig. 6.5 which needs to be well known in order to extract any useful information. Furthermore it is desirable to use the spectroscopic and angular scan to find a single solution. Sensitivity in total internal reflection is not very sensitive to the swelling ratio; it is more sensitive at 58° which is beyond TIR. TIR ellipsometry is not suited for the measure of swelling. Brewster angle ellipsometry would be more appropriate. The VASE ellipsometry is therefore expected to be able to resolve the thickness and grafting density of the brush. As the thicknesses are relatively large, we should be able to retrieve both thickness and concentration.

6.3.2 Measured VASE

The vase measurement are shown in Figs. 6.10-6.14 for two pH values. As PDMAEMA is a weak base, the chains are expected to be more charged and more swollen at low pH.

A quick comparison with the simulation show that the measured data do not match the simulation. If we fixed the grafting density at the expected values, reasonable fits can be obtained but the values of the thickness are unphysical. We concluded after much data analysis that the brush systems were degrafted as previously mentioned.

We therefore relaxed the condition of conserved mass, and use both grafting den-

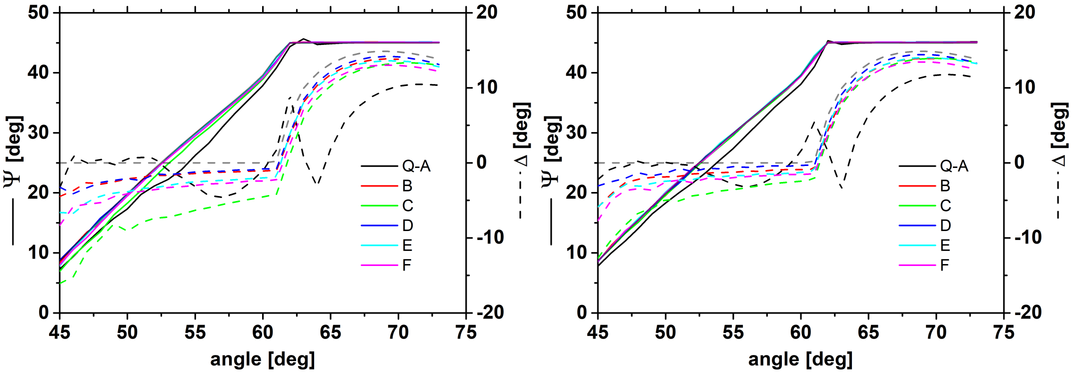

(a) pH 4, swollen state **(b)** pH 10, collapsed state

Figure 6.10: Ellipsometric data under internal reflection for the different samples. The gray lines are the theoretical prediction without accounting for birefringence. $\lambda = 500nm$

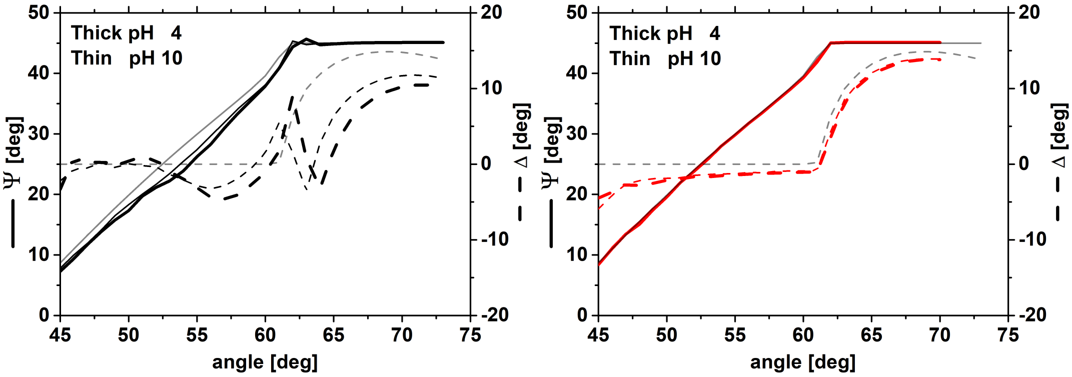

(a) Q-A **(b)** B

Figure 6.11: Ellipsometric data under internal reflection for the different samples. Comparing the data as recorded under pH 4 and 10. The gray lines are the theoretical prediction without accounting for birefringence. $\lambda = 500nm$

sity and thickness as free parameters. We used all of the available data (different measurements and spectroscopy) to attempt a reconstruction of the sample without prior knowledge.

This was only possible for sample C. Fits of the data from sample C converged to a single solution when fitting thickness (assuming dry), Δ shift and Ψ shifts even after providing different initial values. This gives us confidence on the quality of the fit.

The method did not converge for the other samples. No reasonable values of the swollen thickness and the swelling ratios could be obtained. This was primarily due to the relatively large birefringence of the cell.

The measured dry thickness for sample C was 16.1 nm as compared to the 56 nm

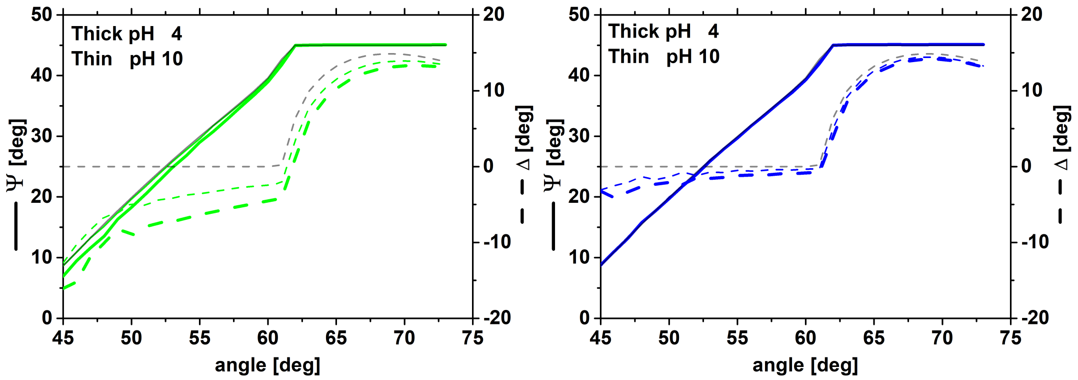

(a) C (b) D

Figure 6.12: Ellipsometric data under internal reflection for the different samples. Comparing the data as recorded under pH 4 and 10. The gray lines are the theoretical prediction without accounting for birefringence. $\lambda = 500nm$

(70% mass loss) right after synthesis or on the sample stored dry. The wet thickness at pH 4 was 98 ± 11 nm and at pH 10 it was 37 ± 8 nm as depicted in Fig. 6.13

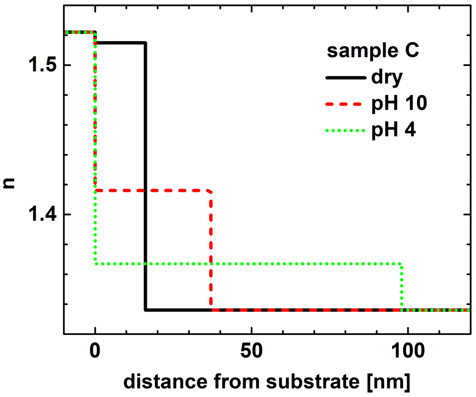

Figure 6.13: Refractive index profiles for sample C at λ=500 nm.

The values obtained for the new wet thickness of sample C are well in agreement with literature values [21, 26, 27, 28].

The quaternized thick sample Q-A displayed strong resonance oscillations (Fig. 6.11b), over the angular and wavelength dispersions. This is an indication of thickness comparable to visible wavelengths used. The brush clearly showed the oscillations which allow to determine a thickness of around 600 nm.

The simple box model is an over simplification in the case of thick soft layers as the brush. The box model being based on clean Fresnel interfaces predicts strong clean resonances, which, although seen on the data, are not, and cannot be as strong as those

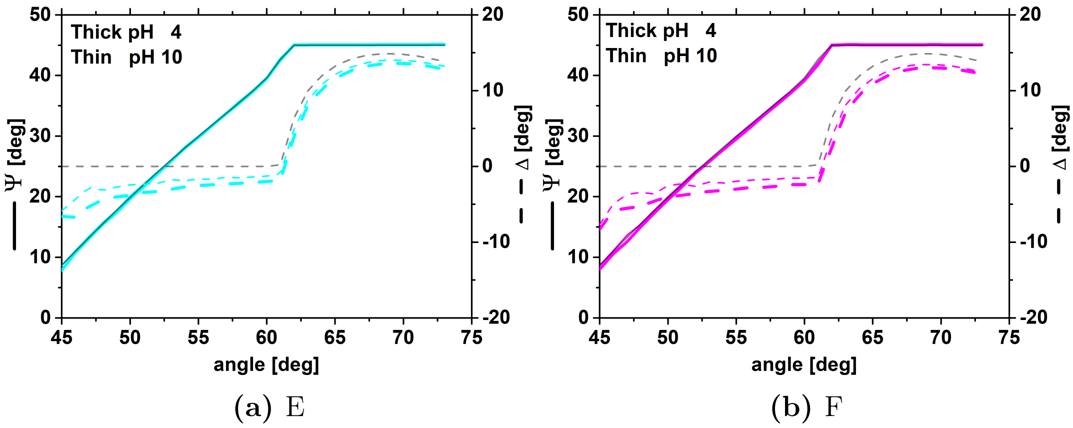

(a) E (b) F

Figure 6.14: Ellipsometric data under internal reflection for the different samples. Comparing the data as recorded under pH 4 and 10. The gray lines are the theoretical prediction without accounting for birefringence. $\lambda = 500nm$

predicted for Fresnel interfaces.

The step-like profile provides strong resonances. However such profile is unlikely as it is expected to be smoother [29]. The clear presence of a "resonant" Δ clearly points to the layer thickness of the order of λ. From the strong oscillation on the phase angle seen in Fig. 6.11a at around 60° we obtained different thicknesses for the brush under the different buffers.

For the pH 4 buffer the obtained wet thickness is 660 nm while at pH 10 the value is of 600 nm. Sample Q-A, being quaternized, is not sensitive to the pH and therefore the change is expected to be due to the change in ionic strength in the buffers (0.1 M for the pH 4 and 0.19 M for the pH 10), though they are only a factor of 2 apart. The molar density of the charged groups within the brush, assuming a homogeneous box model with 630 nm thickness, is 1.5 M, ten times higher than the ionic strength of the buffers.

6.4 Response kinetics

Ellipsometry capture the time dependent response of the polymer layer following a change of pH. The equilibration time appears to be in the order of sec to mn. We did not observe longer times (10 mn) as sometimes reported.

6.4 Response kinetics

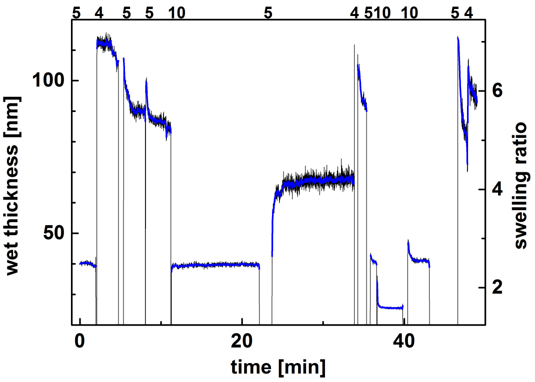

Figure 6.15: Fitted wet thickness and derived swelling ratio for sample C during the kinetic measurement. The blue line is the smoothed version of the fit result (black line). The dry thickness of 16.1 nm was used to fit the data.

The results obtained for brush C are shown in Fig. 6.15. Analysis was done using Complete EASE and the box modeling, assuming constant "mass" and change of thickness/swelling. The fit returned good results so that we obtained values for thickness/swelling.

The values in Fig. 6.18 were extracted from the data in Figs. 6.16-6.17 where the "apparent" thickness evolution is shown. Note that we refer to them as "apparent", they are not the real physical thicknesses of the brushes but the information on the response times is still contained within.

The values are on the order of several 10's of seconds, by comparison, Wanless et al. report transition times of 1 min for swelling and 4 min for collapsing on PDEA [21]. Others report similar values as well [24].

The sample changes drastically through the evacuated state which sometimes is shorter than the half times obtained. The actual times through this unusual evacuated state transition should be shorter than 20 s. One particular that we notice is that in literature the pH is changed over mL volumes in the order of mL/min and the samples are not subjected to shear forces. In our case we used exchanged 0.01 mL volumes with 50 mL/min.

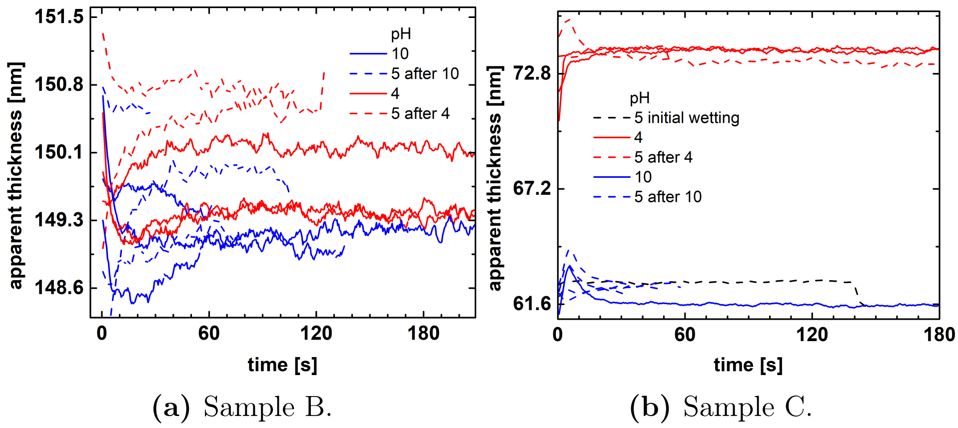

(a) Sample B. **(b)** Sample C.

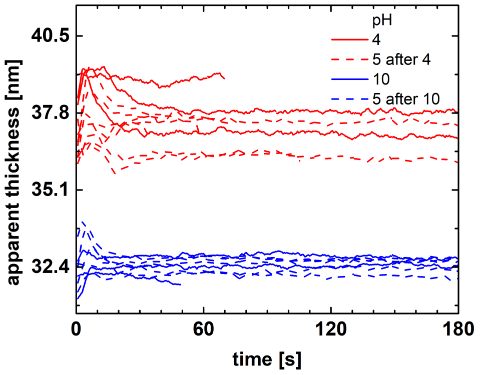

(c) Sample D.

Figure 6.16: Smoothened "apparent" thickness values obtained from fitting with the wrong grafting density. Time 0 was set to when the value went above a certain arbitrary threshold. Dashed lines indicate when milliQ water of pH 5 was introduced either after the pH 4 (red) or pH 10 (blue) buffers.

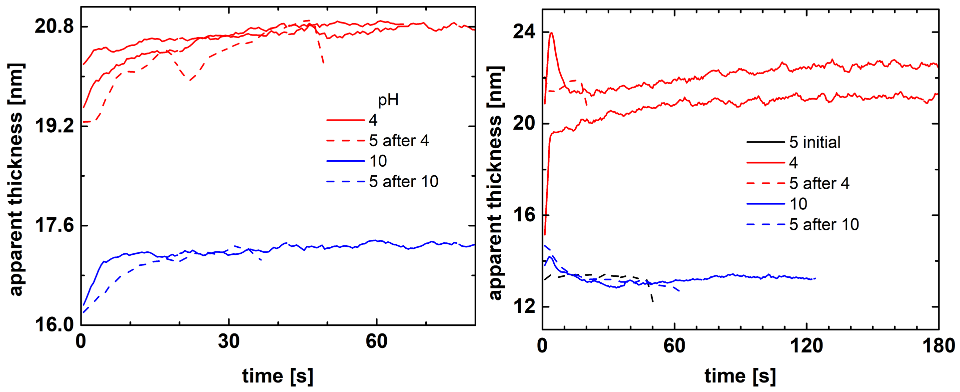

(a) Sample E. **(b)** Sample F.

Figure 6.17: Smoothened "apparent" thickness values obtained from fitting with the wrong grafting density. Time 0 was set to when the value went above a certain arbitrary threshold. Dashed lines indicate when milliQ water of pH 5 was introduced either after the pH 4 (red) or pH 10 (blue) buffers.

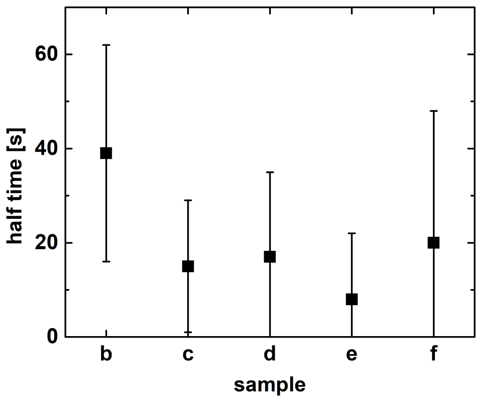

Figure 6.18: Half decay times from kinetic measurements for the weak PEB's.

6.5 Equilibrium dynamics

The VASE study shows rather "extended" brush with high polymer concentration for sample Q-A. We want to explore the concentration dynamics (mostly polymer versus solvent) as has been done in neutral polymer and also initiated in PE brush [18, 19].

Obtaining good evanescent wave dynamic light scattering measurements turned out to be challenging.

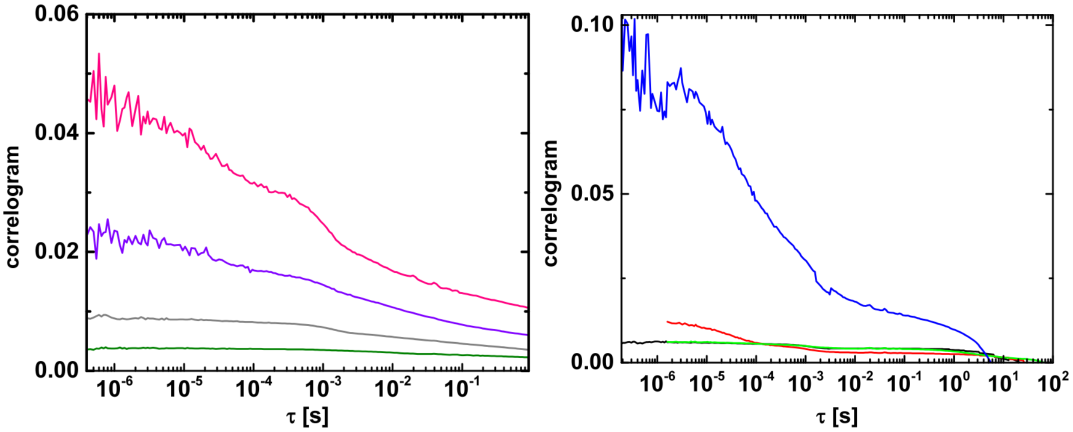

(a) (b)

Figure 6.19: Intensity correlograms. (a) Sample C (b) Sample Q-A

The intensity was dominated by static scattering most probably originating in the glass substrate. Possible brush dynamics were therefore probed through strong heterodyne conditions. Typically raw correlograms have amplitude A of around 10^{-3} as shown on the intensity correlograms in Figs. 6.19a and 6.19b.

Three modes were identified on the measurements. We fitted the data with three stretched exponents ($\exp -(\tau\Gamma)^{\beta}$). A slow stretched mode we take as the slow baseline. A mostly compressed exponential mode at $\sim 1\mu s$ we associate with unavoidable known setup instabilities. Finally, we were left with one single physical sample mode with exponent $\beta \sim 1$ we will examine further. Two of the samples (C and Q-A) displayed the fast mode, and therefore, any information on the internal dynamics.

The measurements were carried out both in both of the buffers used in the previous sections (pH 4 and 10). There was no visible difference on the data on the two buffers so we focus here only on the pH 4 (swollen state) measurements.

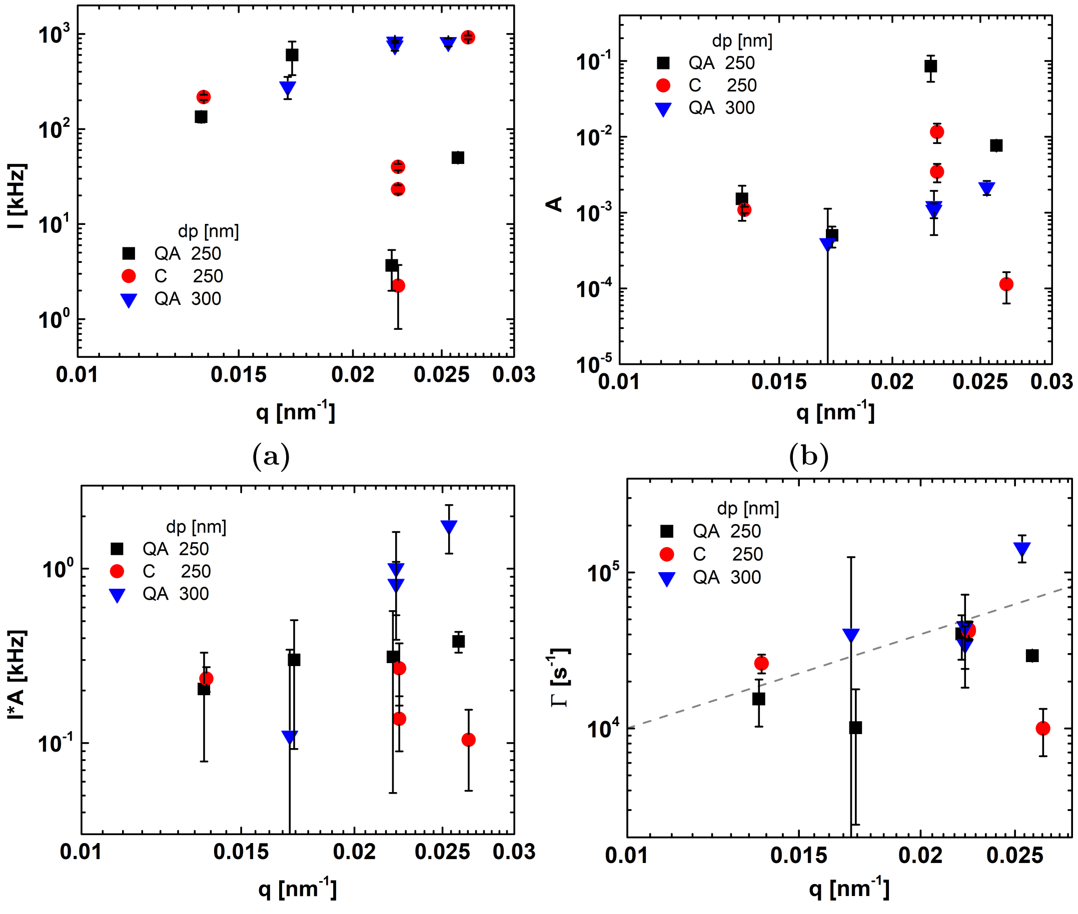

(a) (b)

(c) (d)

Figure 6.20: Samples QA and C. (a) Intensity vs q. (b) Dynamic amplitude of the fast mode vs q. (c) Dynamic intensity of the fast mode vs q. (d) Decay rate of fast mode vs q.

The raw intensities shown in figure 6.20a for similar field penetration depths on the three samples show no particular trend, but a wide spread of the points. This is acceptable as the raw intensity is highly affected by small alignment changes. The amplitudes of the fast mode in figure 6.20b showed an increase as a function of q for the sample Q-A. The same can be said for the total dynamic intensity of the fast mode shown in figure 6.20c. This becomes more evident in figures 6.21b and 6.21c where only values from sample Q-A are shown for several field penetration depths varying over a factor of 2. The penetration depths used were all higher than the dry thickness of the brush (145 nm), but lower than the wet thickness ($\sim$ 600 nm). As a function on penetration depth, there might be a trend of higher dynamic intensities as the pentetration depth is increased, but that is not transparent from the data.

The normalized field correlograms were fitted with a sum of three stretched exponentials (a stretched exponential has the form: $\exp\left(-(t/\tau)^{\beta}\right)$) with fixed β exponents of 1 and 2 for the fast and setup instabilities respectively and a free exponent for the slowest mode. The decay rates Γ obtained are plotted in figure 6.20d for the three samples and in figure 6.21d for sample Q-A at different field penetration depths. In the two figures, the dashed line corresponds to a power law of slope 2. The decay rate values seem to increase with the scattering wave vector, though, power laws ranging from 0 to 3 could describe the points. In any case, the decay rates follow the same trend as the dynamic intensities implying stronger correlation at higher q's.

6.6 Discussion and conclusions

Degrafting Our weak PEB samples suffered from strong degrafting after having been stored in isopropanol for several months. The amount of information we could extract in spite of the degrafting was limited. It is critical for future works to give due importance to the aging of the polymer brushes. Samples with ester, amide or silane groups need to be preserved in anhydrous environment or used not long after synthesis. Other chemistries are desirable from the aspect of brush longevity. The use of hydrolysis liable grafting should definitely be avoided when developing applications

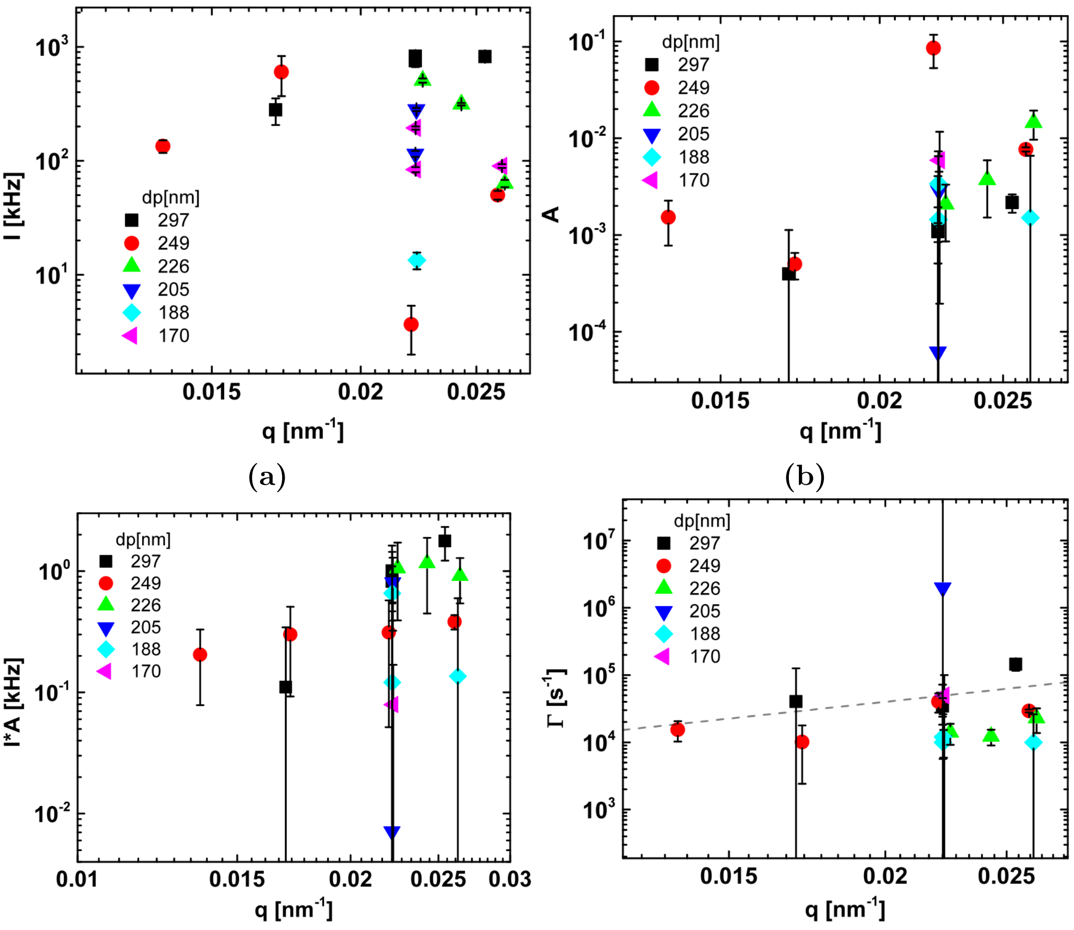

(a) (b)

(c) (d)

Figure 6.21: Samples QA for different *dp*. (a) Intensity vs q. (b) Dynamic amplitude of the fast mode vs q. (c) Dynamic intensity of the fast mode vs q. (d) Decay rate of fast mode vs q.

for wet environments.

VASE VASE in internal reflection geometry and a simple box model with effective medium approximation were used to determine the wet thicknesses of our PEB's. Measuring the absorb amount and wet thickness of polymer brushes is certainly possible as seen from simulations. Still, good knowledge of the birefringence of the setup is necessary in order to extract significant quantities. Prior information such as the absorb amount is typically used to find good solutions. From the VASE data analysis we determined that the samples had undergone strong degrafting after prolonged storage. We worked with effective grafting densities relative to the Mw determined from the

PMMA GPC standard. Absolute values require the knowledge of the absolute Mw. We were not able to recover the thickness of all the samples. For sample C we had sufficient information (mostly using the spectroscopic information) in our data set to obtain an estimate after degrafting. The sample lost 70% of its mass resulting in a grafting density of 0.06 chains/nm^2. The sample swelled by a factor of 6 at pH 4 and 2.5 at pH 10. These values are comparable with those found in literature. The quaternized (fully charged) high density (0.6 chains/nm^2) sample Q-A was found unaffected by the degrafting as also expected form literature. This sample was quite thick in the dry state (150 nm from measurements on a wafer) and showed significant swelling upon wetting. The wet thickness was estimated to be around 600 nm or a swelling ratio of 4. The swollen state presented resonance oscillations in the data which are a clear and undeniable indication of thickness comparable to the wavelength of light. The values we measured for the thicknesses are not coherent. The lower density brush swelled more than the higher density one as should be but the extension of the quaternized brush was 6 times higher than the same Mw lower density. Finally, a 600 nm thickness indicates a molecular weight much higher than the PMMA estimate of 170 nm.

Kinetics of swelling To measure the kinetics of swelling and deswelling as the buffers were changed, we introducing air into the flow cell. The transition times reported refer to the half times between the maximum and the plateau. The average time over the different samples was around 20 seconds. By comparison, Wanless et al. reported times going from 2 to 4 minutes [21].

Dynamics EW-DLS measurements were mined with experimental issues, leaving us with a limited useful time window on the correlograms. The measurements revealed a fast mode in the 10-100 kHz range, that was fitted with an exponential over the $2\pi q^{-1} \sim 300nm$ range. No effect of buffer change could be identified within the sample set. The mode seemed to increase in frequency as q increased, but a scaling law could not established. The same can be said for the dynamic intensity. This was clear only for sample Q-A, showing a possible correlation peak at higher q values. Of the other samples, only sample C showed this fast mode. Albeit the unknown grafting density after degrafting, the other samples were still expected to present dynamics. Yet the other samples measured by EW-DLS (B and F) did not show the fast mode. The fast mode from EW-DLS was 10^6 times faster than the relaxation time measured by ellipsometry and therefore it cannot be of the same nature. Fluctuations in the brush corresponding to those involved in the swelling-deswelling are hidden far in the longer times we were not able to record on this work.

The study of the internal brush dynamics deserves more time, but better experimental conditions are required. Heterodyne measurements require a mechanically stable table, isolated from external vibrations, otherwise the slow channels on the correlogram, the baseline, are plagued by disturbances. The same external vibrations can excite vibrational modes of components placed on the table that again appear in the signal. A stable laser with internal fluctuations not bigger than 0.001%. This includes feedback mechanisms. Our particular case (Torus 532 from Laser Quantum) has a feedback signal at around 1 ms. When this feedback mechanism was turned off, the signal of the fluctuations it tries to correct for appeared in a non predictable fashion over the same time domain. This signal was furthermore of varying shape.

6.7 Acknowledgements

We would like to thank the contribution of the following people to this work. E. Koufakis, and M. Vamvakakis for the synthesis of the polymer brushes and the chemical characterization. E. Koufakis for his help on writing the synthesis part of the chapter, including providing some of the text. We also thank them for the discussion we had. E. Gizeli and D. Xronaki for access to their ellipsometer and support whenever it was needed. We also thank them and the other members of the Biosensors group at UoC for the wonderful time spent there.

6.A Appendix

6.A.1 Scaling laws

Polymer brushes are rich in available architectures and chemistries as seen from the several reviews cited previously. A basic building block of interest for us is the single uncharged polymer chain attached to a solid plane from one end, as discussed by Alexander and de Gennes [2, 3]. Such chains adopt a coil conformation as in the bulk (so called mushroom), when there is no affinity for the surface, and a flat conformation when strong affinity with the wall is present (so called pancake). When the distance D between chains is comparable to the bulk characteristic size R_G, the polymers begin to overlap and push outwards. The thickness d grows as the degree of polymerization N and with the grafting density σ according to [2, 3, 30, 31]:

$$d \sim \begin{cases} N\sigma^{1/3} & \textit{good solvent} \\ N\sigma^{1/2} & \Theta \textit{ solvent} \\ N\sigma & \textit{bad solvent} \end{cases} \tag{6.3}$$

Polyelectrolyte brushes have a complex phase diagram. Zhulina et al. show on [32] develop the phase diagram following a box model based on the force balance of conformational, non-electrostatic volume interactions and electrostatic forces, where no interaction with the wall is admitted. In the limits of small degree of ionization ($\alpha \ll 1$) and of low salt concentration compared to the brush charge concentration $\alpha c_p \gg C_S$ the degree of ionization of weak polyelectrolyte brushes depends on several parameters (polymer concentration (therefore on thickness and grafting density), ionic strength, bulk degree of ionization and pH). Owing to this, weak PEB's have non-monotonic thickness as a function of grafting density and ionic strength, contrary to strong (quenched or permanently charged) PEB's that display monotonic varying thickness. For large salt concetrations or large degree of ionization, the local degree of ionization of the brush is approximately the same as on the bulk.

For polyelectrolytes in solution, in theta solvent conditions, the equilibrium size comes from the balance of electrostatic and elastic free energy giving $R_e \sim N l_B^{1/3} a^{2/3} \alpha^{2/3}$ where N is the degree of polimerization, $l_B = e^2/(\epsilon kT)$ is the Bjerrum length, a is the Kuhn length and α is the fraction of charged sites [33, 4, 34].

Above the overlap concentration and $C_H + C_S \ll \alpha c_p$, the thickness of the brush scales as:

$$d \sim \begin{cases} N\alpha^{1/2} & for\ quenched\ brushes \\ N\sigma^{-1/3}\left(\frac{\alpha_B}{1-\alpha_B}\left(C_H + C_S\right)\right)^{1/3} & for\ weak\ PEB's \end{cases} \tag{6.4}$$

This is the so called osmotic brush regime.

When the salt concentration is higher than the local polymer charges $C_S \gg \alpha c_p$, the weak polyelectrolyte is fully ionized and behaves like a quenched brush. Both thicknesses scale as

$$d \sim N\alpha^{2/3} C_S^{-1/3} \sigma^{1/3} \tag{6.5}$$

This is the so called salted brush regime. Here the added salt starts screening the charged groups and the other non-electrostatic forces start dominating.

The power behaviors described above are experimentally verified. Wu et al. [28] show nicely these scaling behaviors for a weak polyacid.

Through the years much theoretical work has gone into the study of PEB's and the theoretical phase diagrams have become more elaborate and corrections have been suggested for the power laws [34]. Still, the general picture stays the same.

Other than the ionic strength and salt concentration, valency of co-ions and counter-ions are important. Counter-ion valence define the power law during the osmotic brush regime [35]. Experimental work verifies this and shows that entropic considerations like the ones used on the theoretical frameworks cited here are not sufficient to describe the ions effect [27]. Enthalpic, size, charge concentration and hydration radii effects play a major role in the structure of polyelectrolyte brushes.

6.A.2 Density profile

The real density profile is not squared as assumed on the previous scaling laws derivations.

Theoretical density profile for non charged brushes were derived separately by Milner et al. [36, 37, 38], Skvortsov et al. [39] and Zhulina et al. [40] for relatively unstretched chains in good solvent conditions (Gaussian chains). The result is a quadratic density profile. At high grafting density or bad solvent the profile goes from parabolic to box shape [41]. Biesheuvel et al. [42] provided a picture for dense or stretched neutral or charged brushes.

Simulation work by Grest et al. [43] finds good agreement with the Gaussian limit for good solvent condition, and shows the description is not appropriate for higher grafting densities or bad solvent conditions. Later, He et al. [44, 45] obtain agreeable density profiles with the prediction by Biesheuvel et al. [42].

Experimental results on the density profiles on charged and uncharged polymer brushes by fitting neutron scattering data show monotonic decreasing densities with distance from the wall [46, 47, 48]. Strong polyelectrolyte brushes like PMETAC are reported to have more complex profiles with multiple decays.

Sanjuan et al. [48] studied the density profiles for PDMAEMA brushes of 43 kDa for grafting densities around 0.2 chains/nm^2 varying the pH and salt conditions. They report on swellings by a factor of 4 varying slowly over pH: smooth Gaussian profiles for low pH, multiple decays at high pH and parabolic profile in good solvent conditions (methanol).

Bibliography

[1] R. López-Esparza, M. A. Balderas Altamirano, E. Pérez, and A. Gama Goicochea, “Importance of Molecular Interactions in Colloidal Dispersions,” *Advances in Condensed Matter Physics*, vol. 2015, pp. 1–8, sep 2015.

[2] S. Alexander, "Adsorption of chain molecules with a polar head a scaling description," *Journal de Physique*, vol. 38, pp. 983–987, aug 1977.

[3] P. G. de Gennes, "Conformations of Polymers Attached to an Interface," *Macromolecules*, vol. 13, pp. 1069–1075, sep 1980.

[4] O. V. Borisov, E. B. Zhulina, and T. M. Birshtein, "Diagram of the States of a Grafted Polyelectrolyte Layer," *Macromolecules*, vol. 27, pp. 4795–4803, aug 1994.

[5] S. Chen, L. Li, C. Zhao, and J. Zheng, "Surface hydration: Principles and applications toward low-fouling/nonfouling biomaterials," *Polymer*, vol. 51, pp. 5283–5293, oct 2010.

[6] A. Civantos, E. Martinez-Campos, M. E. Nash, A. Gallardo, V. Ramos, and I. Aranaz, "Polymeric and Non-Polymeric Platforms for Cell Sheet Detachment," in *Advanced Materials Interfaces*, pp. 463–495, Hoboken, NJ, USA: John Wiley & Sons, Inc., aug 2016.

[7] A. Steinbach, T. Paust, M. Pluntke, O. Marti, and D. Volkmer, "Selective adsorption of functionalized nanoparticles to patterned polymer brush surfaces and its probing with an optical trap," *ChemPhysChem*, vol. 14, no. 15, pp. 3523–31, 2013.

[8] T. K. Tam, M. Ornatska, M. Pita, S. Minko, and E. Katz, "Polymer brush-modified electrode with switchable and tunable redox activity for bioelectronic applications," *Journal of Physical Chemistry C*, vol. 112, no. 22, pp. 8438–8445, 2008.

[9] D. Li, G. L. Jones, J. R. Dunlap, F. Hua, and B. Zhao, "Thermosensitive hairy hybrid nanoparticles synthesized by surface-initiated atom transfer radical polymerization," *Langmuir*, vol. 22, no. 7, pp. 3344–3351, 2006.

[10] J. Xie, K. Nakai, S. Ohno, H. J. Butt, K. Koynov, and S. I. Yusa, "Fluorescence Correlation Spectroscopy Monitors the Hydrophobic Collapse of pH-Responsive Hairy Nanoparticles at the Individual Particle Level," *Macromolecules*, vol. 48, no. 19, pp. 7237–7244, 2015.

[11] S. Nakayama, S. Hamasaki, K. Ueno, M. Mochizuki, S. Yusa, Y. Nakamura, and S. Fujii, "Foams stabilized with solid particles carrying stimuli-responsive polymer hairs," *Soft Matter*, vol. 12, no. 21, pp. 4794–4804, 2016.

[12] S. J. Jhaveri, M. R. Hynd, N. Dowell-Mesfin, J. N. Turner, W. Shain, and C. K. Ober, "Release of nerve growth factor from HEMA hydrogel-coated substrates and its effect on the differentiation of neural cells," *Biomacromolecules*, vol. 10, pp. 174–183, jan 2009.

[13] B. Yameen, M. Ali, R. Neumann, W. Ensinger, W. Knoll, and O. Azzaroni, "Proton-regulated rectified ionic transport through solid-state conical nanopores modified with phosphate-bearing polymer brushes," *Chemical Communications*, vol. 46, pp. 1908–1910, mar 2010.

[14] M. Krishnamoorthy, S. Hakobyan, M. Ramstedt, and J. E. Gautrot, "Surface-initiated polymer brushes in the biomedical field: Applications in membrane science, biosensing, cell culture, regenerative medicine and antibacterial coatings," *Chemical Reviews*, vol. 114, pp. 10976–11026, nov 2014.

[15] M. A. C. Stuart, W. T. S. Huck, J. Genzer, M. Mueller, C. Ober, M. Stamm, G. B. Sukhorukov, I. Szleifer, V. V. Tsukruk, M. Urban, F. Winnik, S. Zauscher, I. Luzinov, and S. Minko, "Emerging applications of stimuli-responsive polymer materials," *Nature Materials*, vol. 9, pp. 101–113, feb 2010.

[16] O. Azzaroni, "Polymer brushes here, there, and everywhere: Recent advances in their practical applications and emerging opportunities in multiple research fields," *Journal of Polymer Science Part a-Polymer Chemistry*, vol. 50, pp. 3225–3258, aug 2012.

[17] W. L. Chen, R. Cordero, H. Tran, and C. K. Ober, "50th Anniversary Perspective: Polymer Brushes: Novel Surfaces for Future Materials," *Macromolecules*, vol. 50, pp. 4089–4113, jun 2017.

[18] G. Fytas, S. H. Anastasiadis, R. Seghrouchni, D. Vlassopoulos, J. Li, B. J. Factor, W. Theobald, and C. Toprakcioglu, "Probing collective motions of terminally anchored polymers," *Science*, vol. 274, pp. 2041–2044, dec 1996.

[19] V. N. Michailidou, B. Loppinet, D. C. Vo, O. Prucker, J. Rühe, and G. Fytas, "Dynamics of end-grafted polystyrene brushes in theta solvents," *Journal of Polymer Science, Part B: Polymer Physics*, vol. 44, no. 24, pp. 3590–3597, 2006.

[20] M. Biesalski, D. Johannsmann, and J. Rühe, "Synthesis and swelling behavior of a weak polyacid brush," *The Journal of Chemical Physics*, vol. 117, pp. 4988–4994, sep 2002.

[21] J. D. Willott, T. J. Murdoch, B. A. Humphreys, S. Edmondson, G. B. Webber, and E. J. Wanless, "Critical salt effects in the swelling behavior of a weak polybasic brush," *Langmuir*, vol. 30, pp. 1827–1836, feb 2014.

[22] K. Matyjaszewski, "Atom Transfer Radical Polymerization (ATRP): Current status and future perspectives," *Macromolecules*, vol. 45, pp. 4015–4039, may 2012.

[23] X. Huang and M. J. Wirth, "Surface Initiation of Living Radical Polymerization for Growth of Tethered Chains of Low Polydispersity," *Macromolecules*, vol. 32, no. 5, pp. 1694–1696, 1999.

[24] L. A. Fielding, S. Edmondson, and S. P. Armes, "Synthesis of pH-responsive tertiary amine methacrylate polymer brushes and their response to acidic vapour," *Journal of Materials Chemistry*, vol. 21, pp. 11773–11780, aug 2011.

[25] N. C. Ataman and H.-A. Klok, "Degrafting of Poly(poly(ethylene glycol) methacrylate) Brushes from Planar and Spherical Silicon Substrates," *Macromolecules*, vol. 49, pp. 9035–9047, dec 2016.

[26] J. D. Willott, T. J. Murdoch, B. A. Humphreys, S. Edmondson, E. J. Wanless, and G. B. Webber, "Anion-specific effects on the behavior of pH-sensitive polybasic brushes," *Langmuir*, vol. 31, pp. 3707–3717, mar 2015.

[27] J. Yu, J. Mao, G. Yuan, S. Satija, Z. Jiang, W. Chen, and M. Tirrell, "Structure of Polyelectrolyte Brushes in the Presence of Multivalent Counterions," *Macromolecules*, vol. 49, pp. 5609–5617, aug 2016.

[28] T. Wu, P. Gong, I. Szleifer, P. Vlček, V. Šubr, and J. Genzer, "Behavior of surface-anchored poly(acrylic acid) brushes with grafting density gradients on solid substrates: 1. Experiment," *Macromolecules*, vol. 40, no. 24, pp. 8756–8764, 2007.

[29] J. D. Willott, T. J. Murdoch, G. B. Webber, and E. J. Wanless, "Physicochemical behaviour of cationic polyelectrolyte brushes," *Progress in Polymer Science*, vol. 64, pp. 52–75, jan 2017.

[30] T. M. Birshtein and E. B. Zhulina, "Conformations of star-branched macromolecules," *Polymer*, vol. 25, no. 10, pp. 1453–1461, 1984.

[31] O. V. Borisov, T. M. Birshtein, and E. B. Zhulina, "Collapse of grafted polyelectrolyte layer," *Journal de Physique II*, vol. 1, pp. 521–526, may 1991.

[32] E. B. Zhulina, T. M. Birshtein, and O. V. Borisov, "Theory of Ionizable Polymer Brushes," *Macromolecules*, vol. 28, pp. 1491–1499, sep 1995.

[33] P. De Gennes, P. Pincus, R. Velasco, and F. Brochard, "Remarks on polyelectrolyte conformation," *Journal de Physique*, vol. 37, pp. 1461–1473, dec 1976.

[34] E. B. Zhulina and M. Rubinstein, "Ionic strength dependence of polyelectrolyte brush thickness," *Soft Matter*, vol. 8, no. 36, pp. 9376–9383, 2012.

[35] E. B. Zhulina, O. V. Borisov, and T. M. Birshtein, "Polyelectrolyte brush interaction with multivalent ions," *Macromolecules*, vol. 32, no. 24, pp. 8189–8196, 1999.

[36] S. T. Milner, T. A. Witten, and M. E. Cates, "A Parabolic Density Profile for Grafted Polymers," *Europhysics Letters (EPL)*, vol. 5, pp. 413–418, mar 1988.

[37] S. T. Milner, T. A. Witten, and M. E. Cates, "Theory of the grafted polymer brush," *Macromolecules*, vol. 21, pp. 2610–2619, aug 1988.

[38] S. T. Milner, "Polymer brushes," *Science*, vol. 251, pp. 905–914, feb 1991.

[39] A. Skvortsov, I. Pavlushkov, A. Gorbunov, Y. Zhulina, O. Borisov, and V. Pryamitsyn, "Structure of densely grafted polymeric monolayers," *Polymer Science U.S.S.R.*, vol. 30, pp. 1706–1715, jan 1988.

[40] Y. Zhulina, V. Pryamitsyn, and O. Borisov, "Structure and conformational transitions in grafted polymer chain layers. A new theory," *Polymer Science U.S.S.R.*, vol. 31, pp. 205–216, jan 1989.

[41] D. Shim and M. E. Cates, "Finite extensibility and density saturation effects in the polymer brush," *Journal de Physique*, vol. 50, no. 24, pp. 3535–3551, 1989.

[42] P. M. Biesheuvel, W. M. de Vos, and V. M. Amoskov, "Semianalytical Continuum Model for Nondilute Neutral and Charged Brushes Including Finite Stretching," *Macromolecules*, vol. 41, pp. 6254–6259, aug 2008.

[43] G. S. Grest and M. Murat, "Structure of Grafted Polymeric Brushes in Solvents of Varying Quality: A Molecular Dynamics Study," *Macromolecules*, vol. 26, no. 12, pp. 3108–3117, 1993.

[44] G.-L. He, H. Merlitz, J.-U. Sommer, and C.-X. Wu, "Static and dynamic properties of polymer brushes at moderate and high grafting densities: A molecular dynamics study," *Macromolecules*, vol. 40, no. 18, pp. 6721–6730, 2007.

[45] S.-z. He, H. Merlitz, L. Chen, J.-U. Sommer, and C.-X. Wu, "Polyelectrolyte Brushes: MD Simulation and SCF Theory," *Macromolecules*, vol. 43, pp. 7845–7851, sep 2010.

[46] J. B. Field, C. Toprakcioglu, R. C. Ball, H. B. Stanley, L. Dai, W. Barford, J. Penfold, G. Smith, and W. Hamilton, "Determination of end-adsorbed polymer density profiles by neutron reflectometry," *Macromolecules*, vol. 25, pp. 434–439, jan 1992.

[47] N. Spiliopoulos, A. G. Koutsioubas, D. L. Anastassopoulos, A. A. Vradis, C. Toprakcioglu, A. Menelle, G. Mountrichas, and S. Pispas, "Neutron Reflectivity Study of Free-End Distribution in Polymer Brushes," *Macromolecules*, vol. 42, pp. 6209–6214, aug 2009.

[48] S. Sanjuan, P. Perrin, N. Pantoustier, and Y. Tran, "Synthesis and Swelling Behavior of pH-Responsive Polybase Brushes," *Langmuir*, vol. 23, no. 10, pp. 5769–5778, 2007.

Overall conclusions

In this thesis, we reported advances in internal reflection techniques applied to the study of interfaces between a hard solid (glass substrate) and various soft material. Such developments might be valuable to the soft matter community as the techniques to study such interfacial processes are scarce. The following is a short summary of the main achievements reported in the thesis.

Concerning the combination of TIR and DLS, we successfully implemented EW-DLS for near wall (NW) velocimetry on a stress controlled rheometer. The measurable quantities are frequencies which rescaled by $1/\boldsymbol{q}$ give the slowest near wall velocity and a near wall velocity gradient. With this tool we have measured slip of various orders of magnitudes on different samples where no attempt was made to prevent it. Newtonian fluids presented stick boundary conditions. Polymer solutions had weak but measurable slip. Colloidal systems like concentrated emulsions presented full slip and strong slip at low shear rates as expected. Unstable colloidal gels were more difficult to measure and usually present stick-slip behavior. Tracer free measurements are possible and were performed on colloidal systems of weak contrast.

The effect of strong scattering on EW-DLS was studied. We found that it is still possible to perform near wall dynamics measurements using the EW-DLS approach for highly turbid samples. Surprisingly the presence of strong scattering is even beneficial for EW-DLS velocimetry. The near wall (NW) signal is enhanced and averaging time is reduced thanks to the high intensities. The detected light from the multiple scattering is temporally shifted to shorter times making it distinguishable from the NW signal. Moreover the multiply scattered light samples the bulk of the material flow and provides a macroscopic average of the bulk shear rate. This signal is qualitatively described by traditional DWS velocimetry theory. This makes it possible to estimate bulk flow profiles with special interface sensitivity on conditions that are prohibitive with microscopy techniques.

We recorded stick to weak slip boundary conditions and linear bulk average flow profile on dense hard sphere system just before the glass transition. For a hard sphere system beyond glass transition volume fraction, we also measured the same stick boundary conditions and linear flow profile at high shear rate when the glass had yielded. At the lower rates slip lengths of 10 μm were observed. Such values are hardly recognizable from rheological measurements. These values are in between literature values reported for enhanced slip and prevented slip. We were able to follow the evolution of the near wall and bulk flow during recovery and yielding.

On the technical side, validation of EW-DLS velocimetry for single scattering was supported by Brownian-Langevin simulations and the statistics of light paths in turbid EW-DLS were studied with Monte Carlo (MC) photon tracing simulations. From the MC photon tracing simulations we determined that with the point-of-entrance geometry of EW-DLS, recovery of single scattering dynamics in equilibrium dynamics of turbid media is possible. We recovered quasi single scattering dynamics from a system of concentrated PS spheres by using a simple treatment. This is potentially useful for particle sizing without prior knowledge of l^*.

A future matter of interest is the development of fitting routines to estimate the full flow profile from turbid EW-DLS velocimetry.

An interesting observation was that we measured dynamics pass the critical angle of total internal reflection where propagation of light is strictly “forbidden” by Fresnel equations. One possible explanation of the presence of light in this “forbidden” zone, is that it is the result of near field tunneling from particles to the glass substrate. Consequently it is expected to be near wall signal. Its dynamics should be related to a motion perpendicular to the interface. We measured dynamics comparable to the bulk diffusion when using the EW penetration depth as the relevant length scale.

The study of the EW-DLS of turbid samples called for a good understanding of the internal reflection in the presence of strong scattering losses. Empirical effective medium models have been developed to describe clear-turbid reflectivities. They are proposed and used to determine the composition and sizes within turbid media. We evaluated the validity of some of these models when applied to internal reflection variable angle spectroscopic ellipsometry. We show the value of the wavelength dependence for determining the scattering losses. The wavelength dependence of the losses can be fitted to determine dimensions. The measurements are relatively straightforward but the analysis/interpretation of the data are model dependent. The results indicate that the measurements are surface sensitive, as should be the case. The length scale associated with reflectivity losses in an attenuated total internal reflection fashion is still a matter of debate for turbid samples. But given the surface sensitivity it is probably not possible for a single number to correctly describe the data.

The internal reflection DLS and ellipsometry could prove useful for systems consisting of thin layers of adsorbed or grafted polymers, in particular polyelectrolyte brushes that are currently much studied as multi-reponsive layers. We have attempted to study densely grafted weak bases PE, with large Mw. We studied a high density (∼600 times overlap concentrations) high Mw (150 kDa relative to PMMA standards in GPC) quaternized strong polyelectrolyte and a lower density (∼60 times overlap concentrations after degrafting) weak polyelectrolyte same Mw sample. The lower grafting density brush displayed swelling ratios of 2.5 and 6 in pH 10 and 4 respectively. For the quaternized dense sample of dry thickness of 150 nm we observed distinctive resonances in the ellipsometric data that correspond to approximately 600 nm of wet thickness, an extremely extended state. The kinetics of swelling in conditions far from equilibrium were significantly faster (20 seconds) compared to those reported in literature (minutes) for smooth in equilibrium transitions. Further we realize that stroing condition are of prime importance for this type of chemistry. As has been recently shown, polyelectrolytes brushes anchored with amide, ester and silane groups tend to degraft by hydrolysis, specially at high grafting densities. Such brushes should be stored under dry or anhydrous conditions to prevent hydrolysis.